Development of a Marker-Based iFEM Optimisation Approach for Aeroelastic Load Characterisation in Gust

Louis Alen

In partial fulfilment of
the degree of Master of Science
in Aerospace Engineering
at Delft University of Technology.

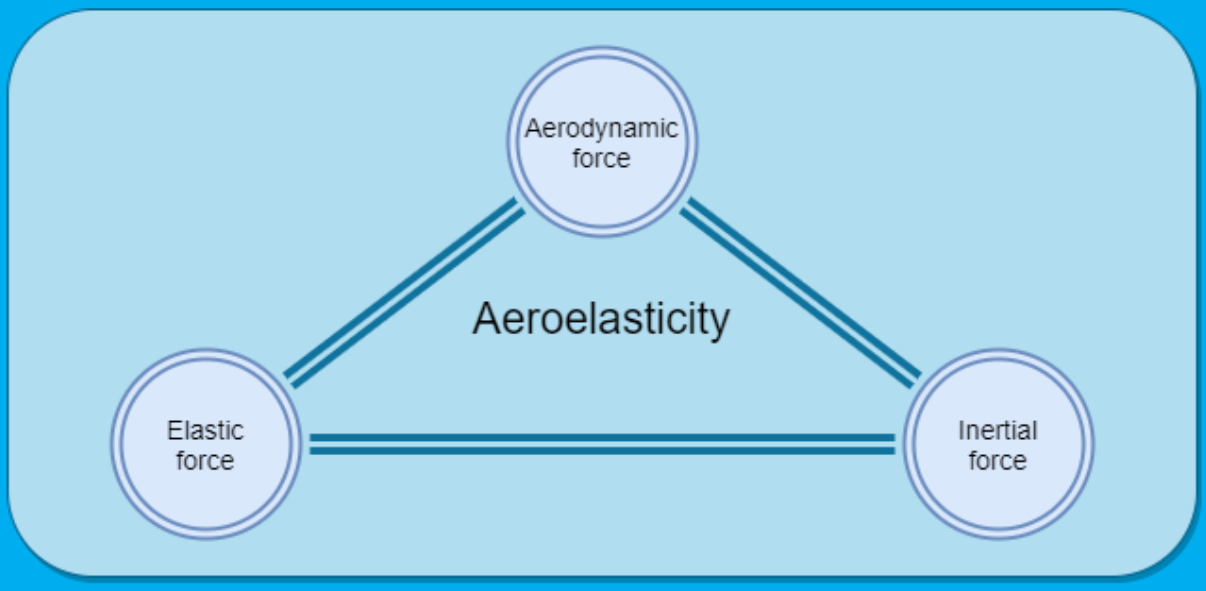

TU Delft

Development of a Marker-Based iFEM Optimisation Approach for Aeroelastic Load Characterisation in Gust

by

Louis Alen

in partial fulfilment of the degree of Master of Science
in Aerospace Engineering at Delft University of Technology.

Student number: 4446542
Project duration: March 2, 2020 – January 25, 2021
Thesis committee:

Dr. A. Sciacchitano,	TU Delft, supervisor
Dr. ir. B. van Oudheusden,	TU Delft, chair
Dr. ir. S. G. P. Castro,	TU Delft
Dr. ir. A. H. van Zuijlen,	TU Delft

TU Delft

Preface

What makes a thesis dissertation interesting, is the constant discovery of new and challenging hurdles to overcome and get through, though this is not captured in this document. For this particular thesis, however, not only had I encountered hurdles, but complete lane-changes. What was supposed to be an intensely experimental project, turned into a numerical-based one. What I had hoped would be written whilst among research-leading experts, was written in the confinement of my personal spaces. I will mention no troubles specifically, but in such tough times I did not just develop a deep understanding of the topic of aeroelasticity – I learned what one should value most in life: the merit of those closest to oneself. This list of people – which will not be exhaustive – consists of parents, siblings, my partner, but also myself. In a period where you spend a lot of time by yourself, it is important to recognise one's assets.

Handing in this document serves as the ideal opportunity to thank those people who kept me under their wing in times of need, to support me in finding challenges and developing the person I stand to be today. First and foremost, my parents. To my father, who has been my guide in the pursuit towards creative thinking, whose parents would have risen above their differences to get together and express their joint pride towards their son and grandson for their accomplishments. To my mother, who has continuously pushed me to walk the extra mile and face challenges head-on beyond where I would have gone without her, and my grandparents that have always been ready to catch me when I fell – void of hesitation. To my brother, who regardless of plentiful poignant moments between the two of us, has assisted me in ways he likely has never realised. It is thanks to them, and the entirety of my dear family, that I have reason to be proud of myself. Besides wanting to thank those people for the person they have brought me up as, I cannot come close to expressing in writing the gratitude I have for the opportunities I was offered. They went out of their way whenever necessary such that I could enjoy the best education available to me and be exposed to the greatest sources of innovation and engineering. I dare to bet that they will never realise how much I am grateful for their support, even for the small things such as picking me up at Schiphol airport despite having previously bought me a ticket for a direct train home which would have taken 15 minutes longer, or buying models of Tintin's red-white Moon Rocket for each one of my successful academic years. Memories of being Loved, encrypted in my mind to carry with forever.

On a more professional basis, it goes without saying that I thank the thesis committee for their assistance, guidance and feedback during this project. The flexibility required to cope with such a change of tides has not gone unnoticed. I appreciate the effort and enthusiasm they shared for the thesis which has allowed for this document to be a worthy contribution to the body of science. After five and a half challenging years, my academic career has come to an end and this team of researchers has made it an enjoyable one.

Louis Alen
Antwerp, December 2020

Executive Summary

In the field of aeroelasticity, research revolves around the study of the interaction of three forces: inertial, aerodynamic and elastic forces. This interaction is often depicted in the aeroelastic triangle of forces, or Collar's triangle. In order to understand the interaction between these forces, it is quintessential to be able to quantify them at each point in time during an aeroelastic encounter.

Studying these loads experimentally has until now required complex experimental set-ups, though efforts were made to use numerical additions to form hybrid approaches. Such approaches combine the benefits of numerical and experimental techniques to eliminate individual disadvantages and supplement the retrievable data with more accuracy or detail. With the recent development of an integrated particle-image velocimetry and marker-tracking technique, capable of capturing large-scale information on both the flow and the structural motion, an interest has grown in the exploitation of this data in a hybrid approach to characterise Collar's triangle in a span-wise sense on a flexible wing.

For this purpose, a hybrid approach was proposed which incorporates assumed prior knowledge regarding the load distribution from lifting-line theory to predict a load distribution given a measurement of span-wise deflection from the markers. The framework first attempts to optimise such a scaled distribution, after which it will individually tune nodal forces to further match the deflection. With a linear separation of the deflection caused by the aerodynamic and inertial loads, where the latter is calculated from the mass distribution and the marker acceleration, it is then possible to extract the three components of Collar's triangle from marker measurements. The framework uses a finite-element method (FEM) model based on the composite lay-up of the wing structure on which it imposes a force as a variable to achieve a measured deflection through the optimisation process in an inverse FEM approach.

This novel framework was first studied in a numerical environment where artificial errors were imposed on numerical data obtained from MSC.Nastran to assess its response to potential empirical flaws. The result of this analysis showed the robustness of the application in a static case, where the dynamic case was disregarded as the inertial forces are calculated directly from the marker measurements and have no influence on the optimisation. Measurement errors and limited accuracy showed to have a random impact on the framework, while an error in the FEM model introduced a linearly increasing systematic error on the results.

Considering the results of this sensitivity analysis, on the one hand a static test case was conducted in the wind tunnel. Under a static aerodynamic load, the lift force was extracted locally near the tip region from circulation measurements with particle image velocimetry for a flexible wing. The framework showed that it managed to extract those local lift values accurately. Results from force balance measurements then showed that the framework had higher net root force predictions, which are likely caused by an error in the FEM model and the acquisition set-up. The resultant span-wise distribution showed promising matches with a vortex-lattice method prediction for the same flow conditions.

On the other hand, results show that the framework also works in a dynamic environment, in this case a harmonic gust. While the entire span-wise load distribution cannot be assessed at this point, there is no indication that the predicted distribution differs from the actual load based on the bending moment measurements. Considering the match of the inertial load between the numerical and the measurement-based computations, one can conclude that the approach with the marker measurements allows for the calculation of the inertial load, provided that the mass distribution is given. As for the aerodynamic loads, taking into consideration a slight discrepancy in the present work which is assumed to be caused by modelling aspects, it is concluded that the framework manages to predict the aerodynamic load distribution which matches the deflection also in unsteady scenarios. Following these conclusions, it has been shown that the framework allows for the separation of the three forces of Collar's triangle in a dynamic aeroelastic environment.

Follow-up research is suggested to focus on taking into account more experimental data such as force balance measurements in the optimisation as constraints, and to obtain more quantitative velocity data in order to assess the dynamic load distributions. On the structural side, shape functions could be used to model the marker measurements to reduce the measurement errors. Lastly, optimising the accuracy of the FEM model with respect to the test model is also recommended for further applications of the framework.

Contents

List of Figures

List of Tables

Nomenclature

List of Abbreviations

BC	Boundary Condition
CFD	Computational Fluid Dynamics
CVV	Coaxial Volumetric Velocimeter
DOF	Degree of Freedom
FEM	Finite-Element Method
HFSB	Helium-Filled Soap Bubbles
iFEM	Inverse Finite-Element Method
LDV	Laser-Doppler Vibrometer
LES	Large-Eddy Simulations
LLT	Lifting-Line Theory
MRD	Mean Relative Difference
OJF	Open Jet Facility
PIV	Particle Image Velocimetry
RANS	Reynolds-Averaged Navier-Stokes
SA	Sensitivity Analysis
SD	Standard Deviation
STB	Shake-The-Box
TC	Test Case
VLM	Vortex-Lattice Method

List of Symbols

α_G	Gust Angle of Attack Component [°]
δ_G	Gust Vane Angle [°]
Γ	Circulation $\left[\frac{m^2}{s}\right]$

$\mathbf{d_{act}}$	Actual Displacement Vector $[m]$
$\mathbf{d_{opt}}$	Optimised Displacement Vector $[m]$
$\mathbf{d}$	Displacement Vector $[m, rad]$
$\mathbf{F_{act}}$	Actual Force Vector $[N]$
$\mathbf{F_{inrt}}$	Inertial Force Vector $[N]$
$\mathbf{F_{opt}}$	Optimised Force Vector $[N]$
$\mathbf{F}$	Force Vector $[N, Nm]$
$\mathbf{K_M}$	Mass Matrix $\left[kg\right]$
$\mathbf{K_S}$	Global Stiffness Matrix $\left[\frac{N}{m}, \frac{Nm}{rad}\right]$
ω	Angular Velocity $\left[\frac{rad}{s}\right]$
ρ	Fluid Density $\left[\frac{kg}{m^3}\right]$
σ	Standard Deviation $[-]$
AOA	Angle of Attack $[^\circ]$
b	Wing Span $[m]$
c	Chord Length $[m]$
C_L	Lift Coefficient $[-]$
f	Frequency $[Hz]$
k	Reduced Frequency $[-]$
L'	Lift per Unit Span $\left[\frac{N}{m}\right]$
MRD	Mean Relative Difference $[-]$
r	Random scalar on the interval $[0, 1]$ $[-]$
S	Surface Area $\left[m^2\right]$
V_∞	Free-Stream Velocity $\left[\frac{m}{s}\right]$
V_G	Gust Velocity $\left[\frac{m}{s}\right]$
x	Deflection $[m]$

1 Introduction

As aviation experiences continuous development to reduce flight emissions in order to achieve more sustainability in the industry, more light-weight and flexible materials such as composites are used which experience more intricate fluid-structure interactions that occur between the air and the wind structure. The aerodynamic loads generated by this interaction are compensated for by the elastic loads which are the result of the subsequent deflection of the wing. Due to the relation of this deflection and the respective aerodynamic load, it is important to be able to quantify such loads for the design of the wing structure. The study which concerns itself with this topic is referred to as aeroelasticity [3].

The term is derived from the combination of the study of aerodynamics and mechanical elasticity, and it deviates from classical mechanical elasticity in that the coupling of the fluid-structure interaction is what gives rises to the aeroelastic phenomena [13]. In static and dynamic structural analysis approaches, the load is often assumed to be a constant or time-dependent variable. In aeroelasticity, however, it is also closely related to the local geometry at any given time since it directly affects the resulting aerodynamic load. In addition to the elastic and aerodynamics loads, the inertial loads must also be considered. The inertial loads come from the fact that structures have a mass, which when accelerated will exert a force on the structure. A sudden change in flow conditions may create an imbalance in the aerodynamic and elastic forces, from which an acceleration is generated, in turn generating inertial forces. Collar depicted the relation between these three forces in the aeroelastic triangle of forces [6]. As he was the first to identify it in this context, it is often referred to as Collar's triangle. The connection of these three forces is shown in Figure 1.1, which also shows the various phenomena which comprise the study of aeroelasticity.

To further introduce the topic of aeroelasticity, this chapter is divided into two sections. Firstly, section 1.1 will discuss the relevance of the characterisation of the gust encounter among the other phenomena in terms of the aeroelastic forces for structural design. Secondly, the analyses which are performed to achieve this goal are introduced in section 1.2.

1.1. Aeroelastic Phenomena

When all three forces are quantified, an aeroelastic phenomenon is considered to be fully characterised. As mentioned before, cases in which the inertial force may be ignored are considered static and cases with significant influences from the inertial forces are dynamic. Moreover, when the variations in either one of the forces increases drastically, the system may respond in non-linear manners. When certain models are used which consider small-deflection assumptions, the analysis of a non-linear case may become invalid. Non-linear cases, however, are often difficult to model due to their inherent instability and volatility [3]. Experimental campaigns contribute to the study of highly non-linear phenomena by the fact that in a direct experimental environment no modelling is used and as such all non-linear effects are inherently included. Having an insight from such experiments allows for the improvement of non-linear modelling techniques and the overall study of the three forces during an aeroelastic phenomenon.

Since recent years, aviation safety regulation instances such as the European Union Aviation Safety Agency compiled a list of requirements for various types of aircraft, including certain requirements on how an aircraft should be able to cope with various aeroelastic encounters such as flutter or gusts, for example the Certification Specifications for Large Aeroplanes, or CS-25 in short [8]. Within aeroelasticity, instabilities are studied

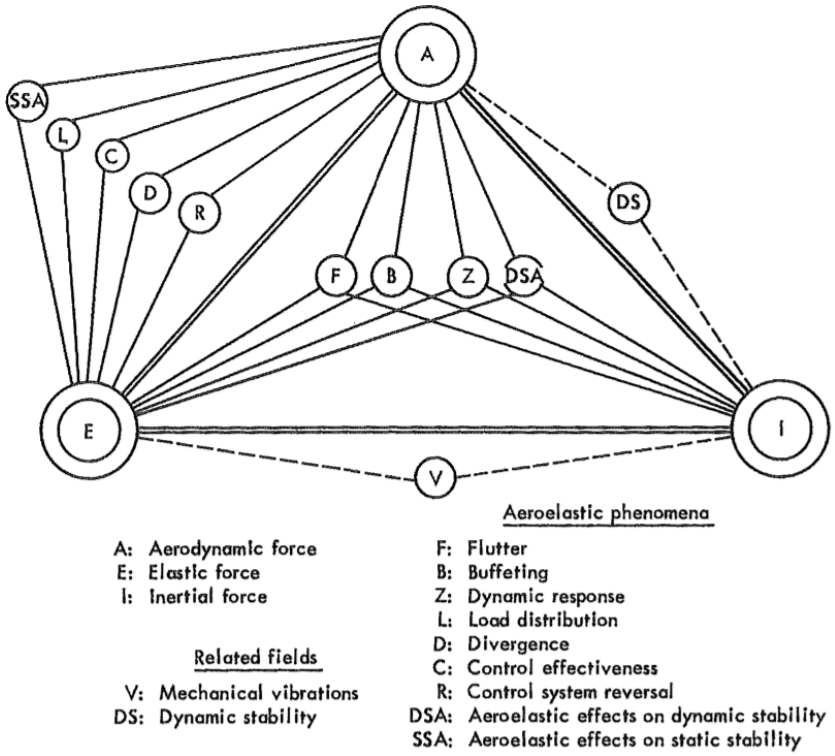

Figure 1.1: The aeroelastic triangle of forces or Collar's triangle, as taken from [3].

which may have catastrophic consequences if not treated during the design of an aircraft. One such instability is static divergence, where the aerodynamic force grows stronger following from the deflection of the respective force. In time, this instability will cause a structural failure due to the strain limits of the material [49]. On the other hand, a dynamic instability which must be avoided in-flight is flutter. This aeroelastic phenomenon follows from an imbalance between the three forces of Collar's triangle which induce vibrations into the structure. As a direct cause, the aircraft may suffer from loss of control or the vibrating surface may eventually fail. The role of inertial forces in such dynamic events cannot be neglected, and as such every phenomena inside the aeroelastic triangle of forces as per Figure 1.1 is dynamic, as they are connected to the three individual forces. It is an aircraft engineer's task to ensure that such aeroelastic phenomena do not occur within the aircraft's flight envelope. There are, however, other phenomena which are unavoidable for the engineer. The structure should be adequately designed such that it can cope with the most load-intense encounters.

One such encounter is that of a gust, as is widely studied in literature [17, 25, 35]. The gust encounter may be the most load-intense encounter in the operational life of an aircraft, making it an essential encounter to be studied in order to meet the CS-25 requirements. For this particular document, the gust encounter is formulated in a 1-cosine shape [8]. It is noted that other shapes such as a sharp-edged or harmonic gust are also considered in literature [3]. In the majority of such studies, the main purpose is to assess the maximal load condition during gust, as this is often considered to be the driving load for the design of the structural reinforcements [49]. The evaluation of this maximal load condition during a gust encounter is therefore essential for the structural validation in CS-25.

1.2. Gust Analysis

The analysis of a gust encounter is performed with both numerical or experimental campaigns in varying stages of aircraft design to achieve the evaluation of the maximal structural load for CS-25 certification. In numerical approaches, often simple analytic models are used which rely on direct relations between the response of the structure and the aerodynamic load. More elaborate numerical modelling will contain increasing levels of complexity. The most complex approach is a direct simulation of the flow and the finite-element modelling of the entire wing. In this case, a coupling mechanism is required which projects the aerodynamic

loads onto the finite-element model at the respective locations. The deflection is then transferred into the aerodynamic model such that the local flow is corrected for the new boundary conditions. Experimentally, the variety of available tools are often distinguished by what type of data they extract: structural or aerodynamic data. From the structural perspective, measurements revolve around obtaining the motion, strain and stresses of a structure [26, 33, 48]. The motion can be used to obtain the deflection and acceleration of a structure, where the latter plays a key role in dynamic events to compute the inertial loads. As for the aerodynamic measurements, the most interesting quantities are surface pressure, flow velocity and overall flow visualisation. The latter may be used to understand the behaviour of unsteady flows. From surface pressure, it is possible to evaluate the various aerodynamic loads such as the lift, drag or pitching moment on the respective surface. Various methods are applied by academia and industry in experimental campaigns to obtain both aerodynamic and structural data, on which more later. These methods often use pre-existing techniques in a new application to extract more information about the encounter. In recent years, researchers have begun using hybrid approaches in which experimental data is used in a numerical environment or vice versa. Such techniques allow for the elimination of disadvantages of one approach over the other.

Ultimately, the goal of experimental aeroelastic investigations is to characterise the fluid-structure interaction in terms of elastic, inertial and aerodynamics loads such that the entire phenomenon may be characterised. Following from the balance of the three forces that make up Collar's triangle, it is hypothesised that by quantifying only two of the three forces, the third one may be determined in an indirect manner. One has two paths to this approach: (1) the aerodynamic loads are measured to obtain the structural loads, or (2) the structural loads are measured in order to arrive at the aerodynamic loads. It is noted that with the former path, only the sum of the elastic and inertial loads may be determined unless another technique is used to make the distinction between those two. As for the second option, most structural measurement techniques allow for the separation between elastic and inertial forces [36]. Hence, it is of interest to measure these two with one technique which implies that the experimental set-up is less costly and complex than when more techniques are applied.

The purpose of this report is to assess this last pathway and whether it is possible to use the structural measurements in combination with an inverse finite-element method tool to extract the aerodynamic loads from making solely structural measurements. The challenge in this approach consists of two aspects. First, the numerical finite-element representation of the experimental model must be sufficiently accurate such that under the same load, the experimental and numerical models will deflect the same. Secondly, the measurement tools used must allow for simultaneous tracking of span-wise points such that the load distribution can be assessed across the wing. The work is an improvement over the initial efforts performed by [38], where Roy et al. managed to do an order-of-magnitude assessment of the forces over a plate during flutter with an inverse finite-element approach. This study applied analytic relations between the aerodynamics and the structural deflection. The improvement over this approach will be based on a novel measurement technique in combination with a more complex finite-element model representation. Thus, the goal of this report is to demonstrate the feasibility of a novel indirect approach which may be used for the complete aeroelastic characterisation during a gust.

The report will first explore the details of aeroelastic characterisation in chapter 2, where the aeroelastic assessment techniques will be elaborated upon. The types of characterisation as discussed before will also be further examined. This chapter will then also define the research statement of the present report. This research builds upon an experimental campaign from a previous study which will be the topic of chapter 3. Following this, chapter 4 will go over how the proposed framework was developed. The overall design considerations and framework flowchart will be discussed. In a numerical campaign, chapter 5 will elaborate on how the framework responds to certain imperfections which may be encountered in an experimental environment. This sensitivity analysis will then be used to finally evaluate the results of the framework when used on experimental data in chapter 6. Lastly, chapter 7 goes over the conclusions which were drawn during the evaluation of the proposed framework and recommendations towards further research on the topic will be touched upon.

2

Aeroelastic Characterisation

This chapter is devoted to provide a basic background of current aeroelastic characterisation methods which creates the context of this document. The characterisation in an aeroelastic environment is relevant for the design of aircraft as well as the research of aeroelastic phenomena. This chapter will further investigate how this characterisation is performed and how it is being applied in research.

The first section, section 2.1, will go over some of the most common techniques to determine the loads and the deflection during an aeroelastic encounter. Then, section 2.2 will discuss the ways in which those techniques are applied to characterise such a problem. One approach in particular is elaborated, namely the inverse finite-element method (iFEM) approach. Lastly, section 2.3 will define the research purpose of this document based on the discussions held in this chapter.

2.1. Evaluation Techniques

For an aeroelastic phenomenon, it is important to be able to understand the response of the structure under all conditions. This allows engineers to ensure that the structure will comply with aircraft safety regulations as discussed previously. To fully understand the response of the structure, it is required to be able to model the interaction between the three aeroelastic forces. In this section, the most common applications in the research of these three loads will be elaborated upon. With quantitative insights, it is possible to make sure that the structure will comply with the regulations.

Generally speaking, it is possible to divide the different tools by two categories. The first category bases itself on what type of technique is used to obtain the insights. With this, one can consider either numerical or experimental techniques. Secondly, the other category can be used to determine what type of load is extracted from the system, namely the structural or aerodynamic load. For structural loads, this may be either as a single component comprising the elastic and inertial loads, whereas some techniques additionally allow for the distinction of these components. For the purpose of this document, the distinction will be made as per the first category. Hence, subsection 2.1.1 will cover the numerical applications and subsection 2.1.2 will go over the experimental techniques.

2.1.1. Numerical Applications

The discussion of numerical applications will be held based on the two aspects of aeroelastic modelling that are used. Both structural and aerodynamic modelling will be considered, starting with the simplest type of modelling, namely analytically, and finishing with the more advanced types of each aspect. There is also the option to directly analytically model the entire aeroelastic encounter, including both structural and aerodynamic forces, which is discussed in the final part here.

Structural Modelling

The simplest approach to structural modelling is with analytic relations such as the Euler-Bernouilli relations [13]. This approach can be used to model load-carrying beams and their resulting deflection. Analytic models are usually simplifications of linear theories such that they can be readily applied for a first estimation. Since they may include assumptions such as small deflections or small angles, they are not used for final design methods.

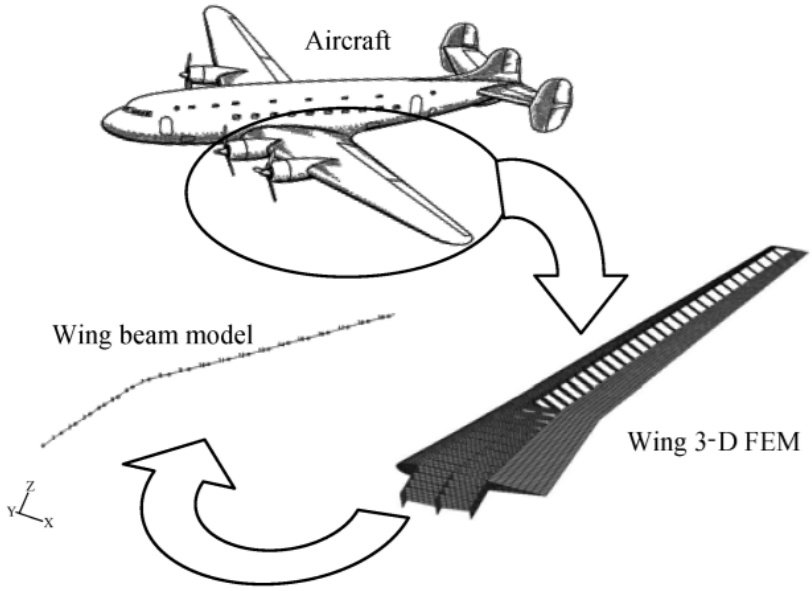

Figure 2.1: Various FEM modelling approaches for an aircraft wing, as taken from [9].

Structural modelling is most commonly performed with finite-element methods (FEMs). Essentially, any structure can be modelled as a number of elements which each have their degree of freedom (DOF) and a certain stiffness. This stiffness matrix can be obtained with a simple model following from the Euler-Bernouilli theorem or more elaborate models such as Timoshenko beams. In essence, the entire system of elements can then be modelled as a series of springs which deflect following a certain load. For example, an entire aircraft wing can be modelled with a 3D FEM shell model or a simpler beam or stick model, as seen in Figure 2.1. FEM can thus be applied with different levels of accuracy to suit the required level of fidelity. Moreover, relations from FEM can be used to derive methods which allow the modelling of the deflection under certain loads, given the necessary boundary conditions, such as the moment-area method for deflection estimation [32]. This method allows for the estimation of the deflection of a simple cantilever beam by using the relation between the local bending moment, the element stiffness and the deflection [31].

A more elaborate FEM application is the addition of a shell element, which allows the creation of 3D elements [27]. Shell elements can be used to represent thin-walled components such as the wing skin, whereas a beam will be used to model spars. With this combination, it is possible to model an entire aircraft. Such box models are more desirable from an aeroelastic point of view as each control surface of a wing can be modelled individually, which assists in the estimation of the flutter speed as it is closely related to the wing geometry. Harmin applied box models to form a baseline reference case in the analysis of other FEM applications, demonstrating its effectiveness in academia [16]. Finally, it is possible to reduce the DOF of a system by, for example, modelling the properties of a shell element onto a beam segment. This can be done for a composite structure as per the work by Ferede and Abdalla in [11]. Essentially, this approach creates a Timoshenko stiffness matrix in six DOF (force and moment in x, y and z) for each node based on the composite material and lay-up. This also allows for the generation of the global stiffness matrix for the entire beam. This matrix can then be used in a direct analytic relation to extract the deflection given the applied forces. It must be noted that due to this exact relation, any mismatch in either the force or matrix may result in erroneous computations of the deflection. In an iFEM approach, where deflections are imposed on the global stiffness matrix to obtain forces, this effect is further emphasised when experimental measurements are used. The experimental measurements include noise and other measurement-related errors which create large deviations in the extracted forces. Due to a small change in the root force, the deflection at the tip can change drastically depending on the structure's stiffness, and vice versa. Hence, any error locally can have effects on the entire result.

When a detailed insight into failure mechanisms or ultimate stresses is required, the entire wing must be modelled which includes material, cross-sectional geometries and so on. This would then become a full FEM analysis. As it is extremely costly, it is often used only in the validation phases of aircraft design or its application is limited to smaller, critical components. In order to use it reliably, a coupling method is necessary

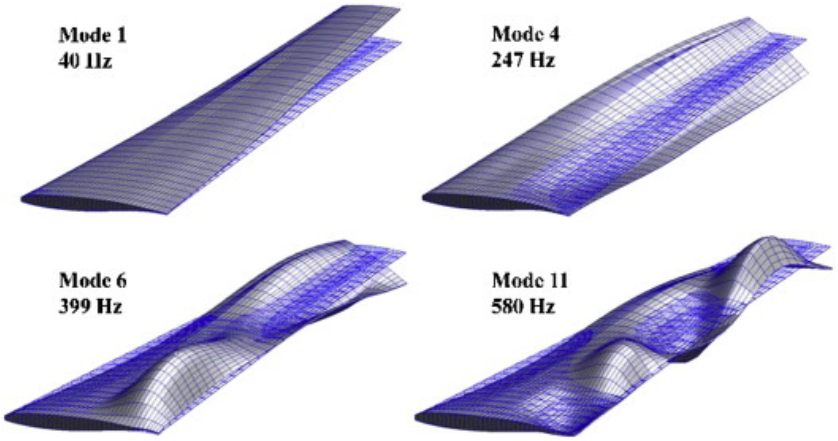

Figure 2.2: The wing was modelled using a FEM shell model, from which the modes as given by the figure were used in the gust response simulations, as taken from [33].

which couples aerodynamic loads onto the structural FEM, especially for dynamic analysis where the loads are dependent on the local geometry. Neumann and Mai used an advanced 3D FEM shell model along with a computational fluid dynamics solver to validate the performance of an experimental gust generator in a wind tunnel [33]. The 3D FEM shell model is seen in Figure 2.2 and was used to assess the vibrational modes in gust.

Aerodynamic Modelling

To model the aerodynamics during a gust encounter, usually only the resulting lift is considered. This load is then imposed on the structural model such that the response can be obtained. While different methods exist for the prediction of aerodynamic loads with increasing complexity, it is often possible to modify an elementary method with additional theorems such that they become applicable in a wider range of problems.

One of the most elementary methods to predict the lift load generated by a wing is Prandtl's lifting-line theory (LLT). This model assumes an incompressible and inviscid flow, where the wing is then modelled as a single bound vortex line at the quarter-chord position of the wing. The vortex extends across the entire span and has two tip vortices which originate from the wing tips and extend aft the wing to form a so-called horse-shoe vortex. This is visualised in Figure 2.3, where one such single vortex is shown. The span-wise lift distribution then follows from the circulation across the span. The circulation along this line depends on the downwash generated by the trailing vortices. With the application of a zero normal flow condition to the vortex sheet, one can determine the circulation as it is affected by the shed trailing vortices. To make this a more accurate model which allows for span-wise variations in geometry, LLT was extended to strip theory in which the wing is modelled in strips along the span by extending the amount of horse-shoe vortices used. Each strip is then comprised of a lifting line and two shed vortices, where the lifting line may vary in strength according to local geometry. Further developments allowed this method to be improved by adding various bound leading edge vortices at several locations chord-wise. This creates panels across the wing surface and such methods are therefore called panel methods. Panel methods allow for the modelling of lifting surfaces individually, which aids in the study of geometry-sensitive phenomena such as flutter.

A study by Kier compared a modified strip theory which accounted for unsteady effects and a panel method, the vortex-lattice method (VLM) in a gust scenario to assess the computational cost and load prediction performance of both in addition to LLT [19]. VLM is an extension of Prandtl's lifting-line theory, it adheres to the same assumptions, implying small angle approximations, thin-walled lifting surfaces and a potential flow. Hence, the effect of thickness and viscosity is neglected. For the purpose required in this article, it serves as an approximation for the forces which can be made by taking into account the geometry of the wing as well as the desired flow conditions in terms of velocity and angle of attack (AOA). In practice, VLM is used in the early design stage of an aircraft for the preliminary design of load-bearing components in lifting surfaces [49]. The method is applied by dividing the wing planform of arbitrary shape in quadrilateral elements as per Figure 2.4, with each a defined collocation point (P in the figure) [1] Horse-shoe vortices of different circulation strengths Γ are placed on each element, where the leading edge of the elements represents a lifting line and the chord-wise sides represent trailing edge vortices. By the superposition of horse-shoe vortices along the

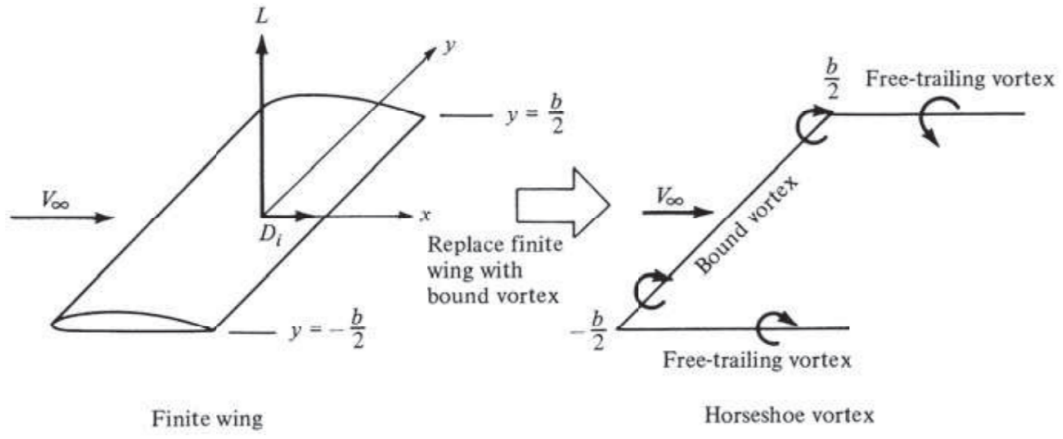

Figure 2.3: Modelling of a finite wing with bound vortices, as taken from [1].

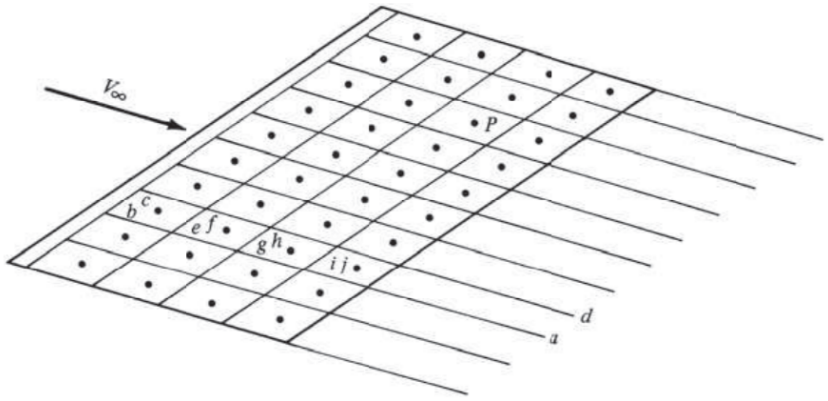

Figure 2.4: Vortex-lattice system on a finite wing, as taken from [1].

chord-wise elements, a finite wing can be represented. At the collocation points, the normal velocity components of all the horse-shoe vortices must add up to zero (flow-tangency condition). This is achievable from the Biot-Savart law and adding each vortex filament component labelled as bc, ef, etc. in Figure 2.4. From the flow-tangency condition, a matrix system can be set up to calculate the unknown strengths Γ for each horse-shoe vortex. From the circulation, one can then extract the normal and tangent forces of the system induced by the circulation. Finally, with the AOA, the lift and induced drag forces may be extracted.

Kier found that LLT was providing more impulsive responses to a gust because as soon as the single bound vortex is in the gust, the entire wing is considered to be in the gust [19]. In VLM, however, each panel will enter the gust before the more aft ones, creating a more realistic response to the gust. They did conclude that for pre-studies in design, the LLT will suffice in ultimate load prediction. At a later stage in this report, VLM will be used for the prediction of aerodynamic loads in the numerical assessment.

The most direct approach in the numerical prediction of aerodynamic forces is by directly solving the Navier-Stokes equations, which is referred to as direct numerical simulation. In practical design studies, this type of simulation is too expensive and therefore simplified models such as Reynolds-Averaged Navier-Stokes (RANS) or Large-Eddy Simulations (LES) are used. Both of these models have their advantages and thus also their specific applications. RANS will model all turbulent effects, whereas LES will model only the smallest turbulent motions – which are expensive to resolve – and compute the larger eddies in the flow. These models' working principles are provided in [12]. CFD is used in gust analyses as it will also show insights into the flow domain, rather than just the forces exerted on the structure [45, 46]. Finally, a CFD module was coupled to a FEM analysis in the study by Neumann et al. to resolve the fluid-structure interaction caused by a gust in a wind tunnel as a validation for the experimental study [33].

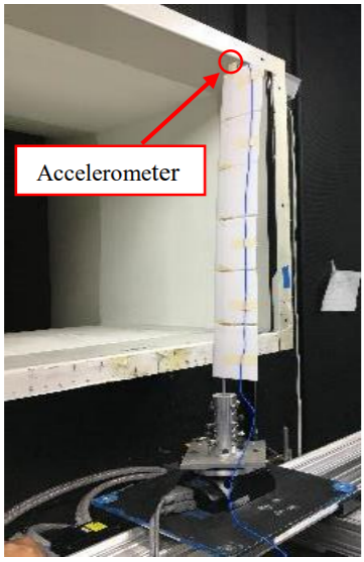

Figure 2.5: The wing with an accelerometer attached to the tip in the experimental campaign by Black et al. [4].

Direct Aeroelastic Analytic Models

Analytic models are the simplest type that can be used to model complete aeroelastic phenomena, including approximations for both the aerodynamic and structural loads. As a consequence of their simplicity, they are rarely used beyond the conceptual phase of aircraft design as they provide limited insights into the gust encounter [20]. Such models rely on the principles of unsteady aerodynamics to take into account the delay in lift caused by the motion of the wing. The analytic models are concerned solely with the overall dynamic loads which the aircraft may experience. They provide no information of the local forces. As a deep understanding of analytic models is considered beyond the scope of this research, the more interested reader is referred to a broad coverage of analytic models provided in the work by Fung [13].

2.1.2. Experimental Techniques

Measurement techniques often used in experimental aeroelastic investigations will be discussed here. The discussion will cover the two main categories of structural and aerodynamic data retrieval methods. Some studies which are relevant for this report are elaborated upon.

Structural Data

Following from the elasticity of a structure, the elastic force will always seek to balance out an external force. In the aeroelastic context, this will be the aerodynamic force. For dynamic cases, an imbalance between these two is introduced by the inertial forces caused by the motion of the wing. This generates an interest in three main structural quantities of interest: acceleration, deformation and load. Here, the most common tools which may be used for the extraction of those quantities will be shown.

The most straightforward technique to measure acceleration is with the application of an accelerometer. In short, a mass is attached to a suspension on which a piezo-resistor is placed. The latter will measure the strain created in the suspension by the motion of the mass following an inertial load. The downside of an accelerometer is that it is an intrusive method as the sensor itself modifies the mass distribution and thus the inertial loads. Black et al. applied an accelerometer to the tip of a wing in an aeroelastic investigation, as seen in Figure 2.5. In this experiment, it was compared to the values of a laser-Doppler vibrometer, or LDV.

An LDV points a laser to a surface of a test model and when the test model moves (e.g. due to a vibration), the amplitude and frequency of the laser's reflection will change. It is possible to measure these changes by the shift in an analogue voltage as recorded in a photo detector. Knowing the properties of the laser, the calculations can be performed to derive the movement of the test surface. In the aeroelastic campaign of Black et al., the LDV showed to have a more accurate measurement on the natural frequency of the model as the accelerometer affected this frequency due to its added mass. Moreover, the authors concluded that LDV allows for a better insight as multiple measurements can be made at various locations [4].

As mentioned before, an accelerometer uses a piezo-resistor to measure strain in the suspension. This resistor is called a strain gauge and essentially measures strain on a given surface. These must be manually

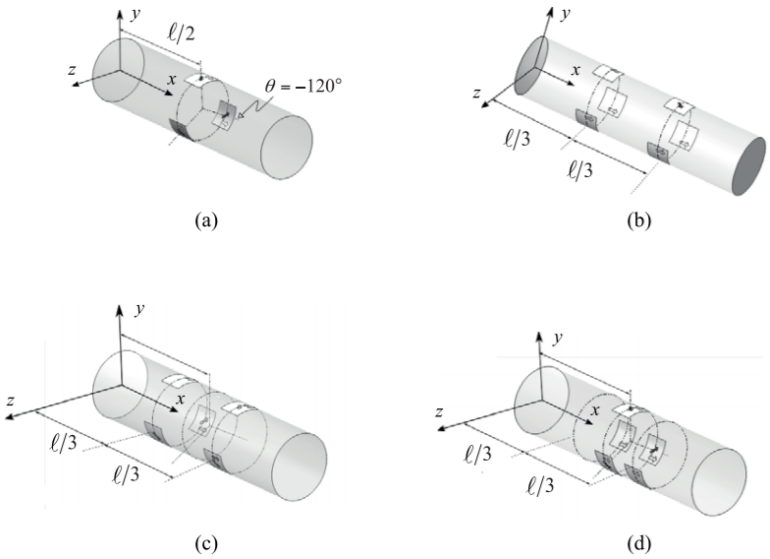

Figure 2.6: The strain gauge configurations as used by Gherlone et al. to perform an iFEM technique to obtain the deflection [14].

attached to flat surfaces and are sensitive to misalignment or other production flaws such as bad adhesion. In an interesting study by Gherlone et al., strain gauges were used to predict the deflection of a simple thin-walled cylinder in both static and dynamic cases [14]. With the application of a numerical iFEM approach and considering experimental measurements, it is a hybrid numerical-experimental approach. Gherlone et al. attempted four different configurations in which the strain gauges were attached, following from the assumption that it may affect the results. These configurations are shown in Figure 2.6. Also, in Figure 2.7, all the static cases performed in the campaign are shown. In an aeroelastic environment, case (iv) is most relevant as it includes a moment which could represent an aerodynamic moment. For each gauge configuration, the results of case (iv) are shown in Figure 2.8. The results are displayed by the respective difference in deflection of the iFEM approach and measurements taken by a linear variable differential transformer. Moreover, Figure 2.9 shows that with increasing FEM elements across the length of the cylinder, the results converge to an error which is – according to Gherlone et al. – defined by the placement of the strain gauges, the FEM geometry and other noise-related errors. For a dynamic case, a vibration with a frequency of 40 Hz and amplitude of $F = 80$ N was imposed on the tip of the cylinder. The time-resolved response of the cylinder from the iFEM approach and the measurements are shown in Figure 2.10. Clearly, the iFEM approach manages to predict the deflection fairly well, though an accurate way of measuring the strain and an accurate FEM representation is required.

The final topic which will be discussed for the acquisition of structural data is called photogrammetry. It is a governing term for techniques in which digital image processing is applied to determine the deflection, motion and acceleration of a structure. A broader discussion of photogrammetry in an aerospace context is provided in [24], whereas this document will focus on one such technique in particular: marker-tracking. By tracking targets or markers placed on the surface of a structure, it is possible to derive its deflection in time and as such also its motion and acceleration. This technique was demonstrated by Graves et al. where it was demonstrated on a business jet model with targets on its surface [15]. In this article, the goal was to supply motion data to aeroelastic solvers such that limit cycle oscillation testing becomes cheaper to perform with more accurate data. It was concluded that this photogrammetric technique was: "a very useful complement to accelerometer data," as stated by Graves et al., where the accelerometer may serve as a local validation measurement. As it is a non-intrusive method which allows measurements to be taken at a wide variety of points simultaneously, the benefits with respect to accelerometers and LDV are clear.

Aerodynamic Data

Similarly to the structural quantities that were defined before, aerodynamic data is often expressed in three individual quantities: velocity, pressure and lift loads. Moreover, these quantities are closely related to each other, as lift is generated by pressure differences. Also, from velocity data, more data such as vorticity can be calculated in post-processing. Common techniques to measure the three aforementioned quantities will be discussed here briefly from an aeroelastic point of view.

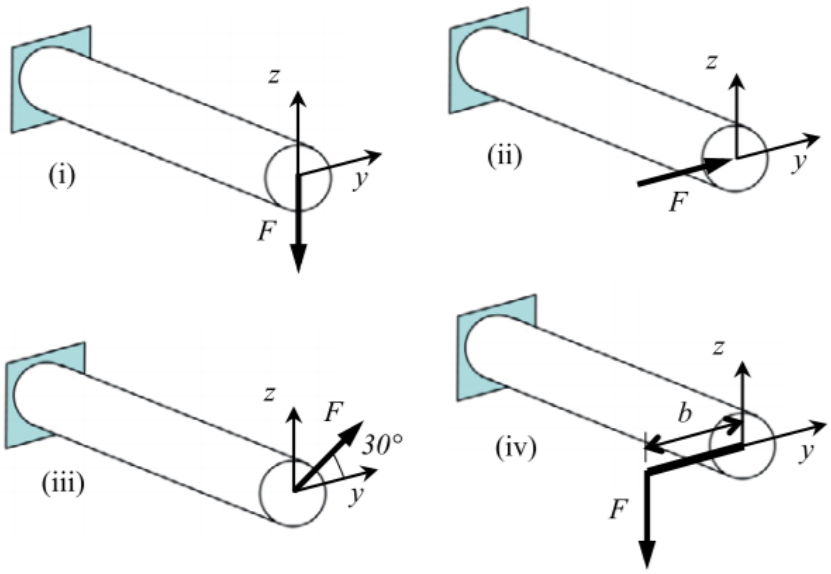

Figure 2.7: Static test cases run by Gherlone et al. in [14]. In all cases, F is the weight of a 26.38 kg mass attached to the rod.

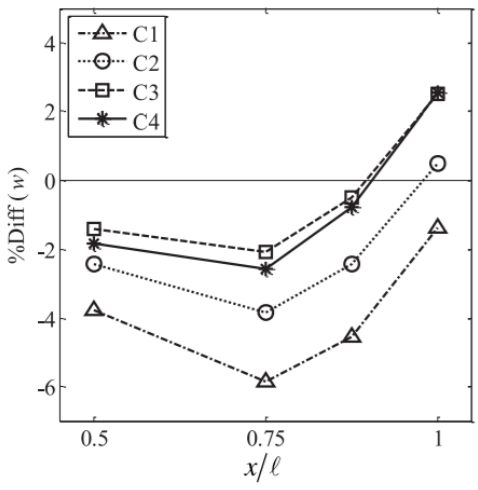

Figure 2.8: The difference of iFEM predictions of the deflection along the longitudinal axis with respect to linear variable differential transformers displacement measurements for load case (iv), with one iFEM element for the different strain gauge arrangements [14].

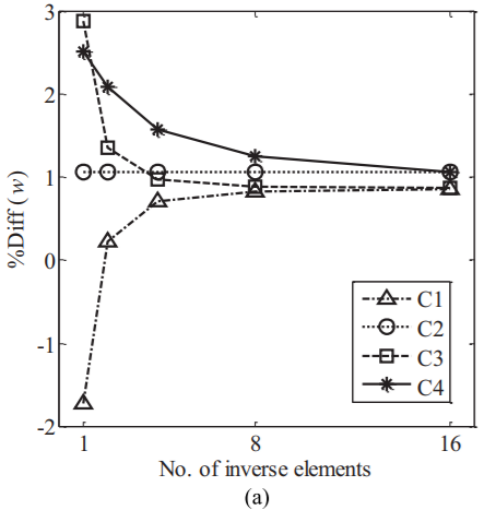

Figure 2.9: The change in difference of iFEM predictions of the deflection along the longitudinal axis with respect to linear variable differential transformers deflection measurements for load case (iv) with increasing number of iFEM elements [14] for the different strain gauge arrangements.

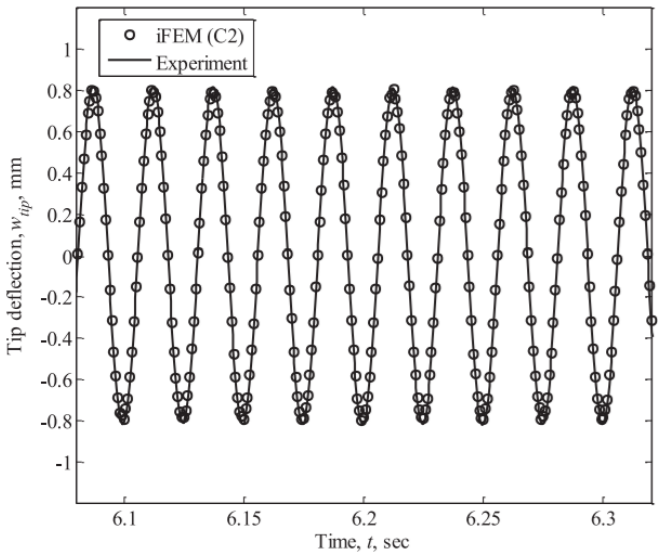

Figure 2.10: Tip deflection of the rod in a dynamic case with $f = 40\ Hz$ and an amplitude $F = 80\ N$ in the experiment by Gherlone et al. [14]. Results are compared with the experimental measurements using a linear variable differential transformers to measure deflection.

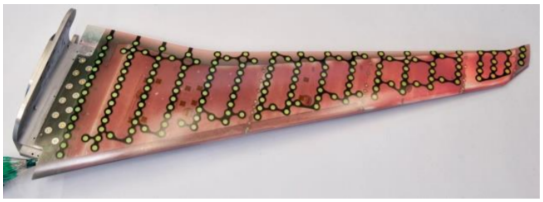

(a) The manufactured version. One can note the tubes coming out of the root section for the pressure taps as well as the markers for stereo-pattern recognition.

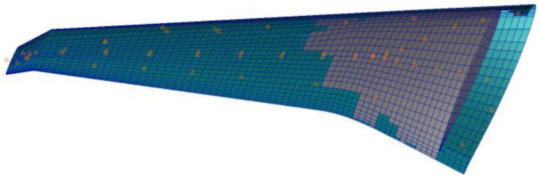

(b) The FEM model. The concentrated masses may be spotted (triangles) which represent the measurement devices (e.g. accelerometers) on the wing.

Figure 2.11: The wing models used by Timmermans et al. in [44] for the tests without a pylon-nacelle mounted.

Pressure taps are used widely in aerodynamic experiments to measure local surface static pressure. By combining pressure measurements in a total and static sense, it is also possible to retrieve the free-stream velocity, given the density of the flow. This is how a Pitot tube is able to measure the flow velocity ahead of an aircraft. Moreover, by having pressure taps spread around the airfoil shape, it is possible to retrieve local pressure data from which the pressure distribution may be calculated. This distribution in turn allows for the computation of the airfoil lift. A pressure tap is essentially a pressure transducer at the bottom of a small hole drilled into the test model. Hence, it is an intrusive method which will affect the flow locally. Furthermore, the measurement itself may be affected by the flow which impedes on the transducer. A deeper understanding of pressure taps as well as a series of applications may be found in [2]. A related study by Timmermans et al. applied pressure taps to extract the lift locally [44]. The lift was calculated by integrating the pressure measurements around the airfoil. With this lift, the deflection was then calculated by imposing the integrated pressures on the FEM model. In the same study, VLM was used to generate a numerical reference in the aeroelastic solver MSC.Nastran from which the deflection of the wing was also determined to validate the deflections obtained from the pressure measurements. Also, the study compared the numerical deflection of the wing with a photogrammetric technique which makes use of markers. The test model with markers and the respective FEM model used is shown in Figure 2.11. The pressure taps are clearly visible in Figure 2.11a, whereas Figure 2.11b shows a box model of the wing with lumped masses which represent measurement devices mounted in the wing. The results of the VLM-based deflection compared to the marker-tracking technique is shown in Figure 2.12, where it can be seen that the two methods match closely. The approach shows promising matches, though it is not always possible to make extensive use of pressure taps due to limitations in the model structure. Finally, the FEM-based deflections are found to match the stereo-pattern recognition measurements which implies that the FEM approach allows for the reconstruction of deflection data.

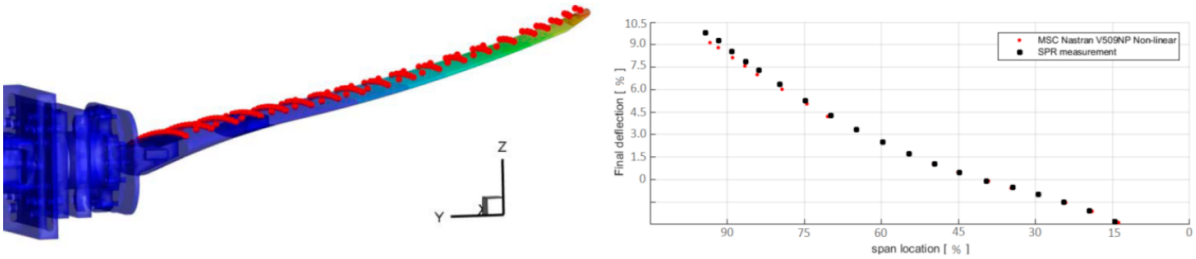

Figure 2.12: A comparison of the FEM results and stereo-pattern recognition measurements for the span-wise wing deflection from the campaign run by Timmermans et al. [44]. Close correlation can be seen between the two methods.

The last measurement technique to be discussed in an aerodynamic-centred context will be particle image velocimetry (PIV). In essence, a laser illuminates a field of the flow in which tracer-particles are moving along with the flow. A digital camera records images with known time intervals and by using tracking algorithms, the velocity can be derived from the images. For a more technical explanation, the reader may refer to [2]. With the application of one camera, velocity can be resolved in a plane with two components. Developments allow for the computations of the third component when a second camera is used, which is called stereoscopic PIV. The PIV technique where a robot guides four cameras around the test model for large-scale measurements is called robotic tomographic PIV. Four cameras are able to resolve three velocity components in a 3D volume. Traditional tomographic PIV, as described by Elsinga et al. in [10], works by the reconstruction of projections from four cameras at two time instances t and $t + \Delta t$ into one volume for each time instance. By then applying cross-correlation of the two volumes it is possible to extract a vector field of the velocity. This process is visualised in Figure 2.13. Jux et al. applied another PIV technique which makes use of the coaxial volumetric velocimeter (CVV) probe as described by Schneiders et al. [41] to visualise the flow around a full-scale cyclist at 14 m/s as shown in Figure 2.14. Here, it is demonstrated that the technique works for large-scale test models while providing valuable insights into local flow behaviour. Jux et al. also calculated vorticity based on the flow data extracted from the PIV measurements. The study emphasised the practicality of the robotic tomographic PIV measurements, allowing for large flow volumes to be visualised at an unprecedented scale.

Finally, the measurement practicality of robotic tomographic PIV was put to the test when it was used in a study by Mitrotta et al. to attempt the simultaneous recovery of PIV and marker-tracking measurements on a flat plate in a gust [29]. This would allow for the flow velocity and structural deflection to be measured with a single, non-intrusive technique on a large scale. In this study, the flow-tracing particles' reflection and the marker reflection was separated by a low-pass filter under the assumption that the markers on the surface of the test model will move much slower than the flow particles. This separation can be seen in Figure 2.15. The result of this study showed that CVV is capable of providing both reliable PIV measurements as well as tracking the motion of the markers in order to obtain structural quantities such as deflection, motion and acceleration. The deflection of the structure is validated with LDV and is compared to the PIV measurements with and without flow tracking particles (in this case helium-filled soap bubbles or HFSB), as seen in Figure 2.16.

2.2. Types of Characterisation Approaches

Following a brief discussion on some of the most common applied aeroelastic investigation techniques, it will now be defined how these are used to characterise the forces of an aeroelastic phenomenon.

2.2.1. Direct Approach

First and foremost, the most straightforward way to characterise each force in Collar's triangle is by directly measuring them individually. Hence, this is defined as the direct approach. This can be performed by the application of one or more measuring techniques as previously discussed to quantify the forces separately. While feasible, this includes complex set-ups and post-processing techniques which may have an undesirable effect on the measurements. The reader may resort to a variety of literature which applies this technique in aeroelasticity, such as the discussed study by Timmermans et al. [26, 33, 37]. The direct approach, as visualised by Figure 2.17a, is not discussed further in this report due to its inherent directness.

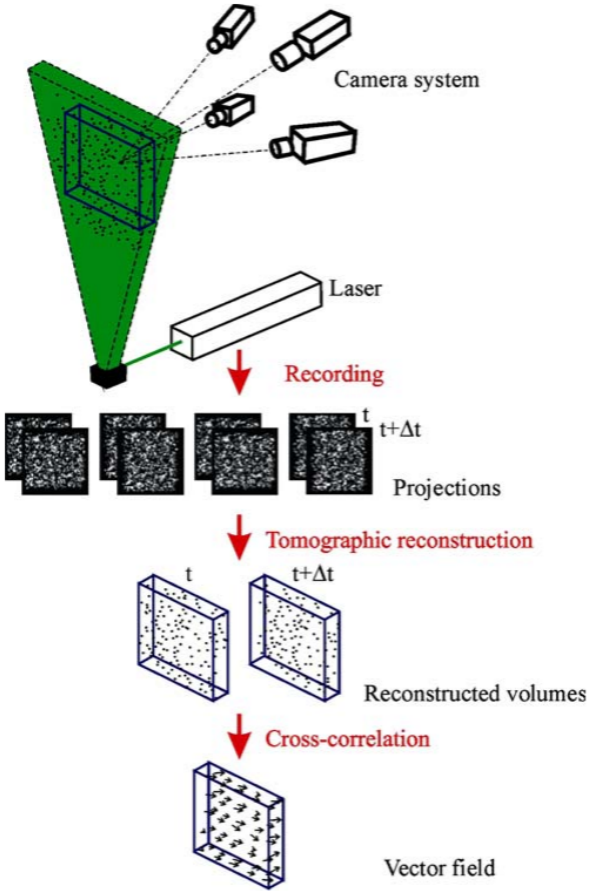

Figure 2.13: Tomographic PIV working principle, as taken from [10]. As can be seen, a vector field for the velocity is created from the projections at two time-steps with the application of cross-correlation.

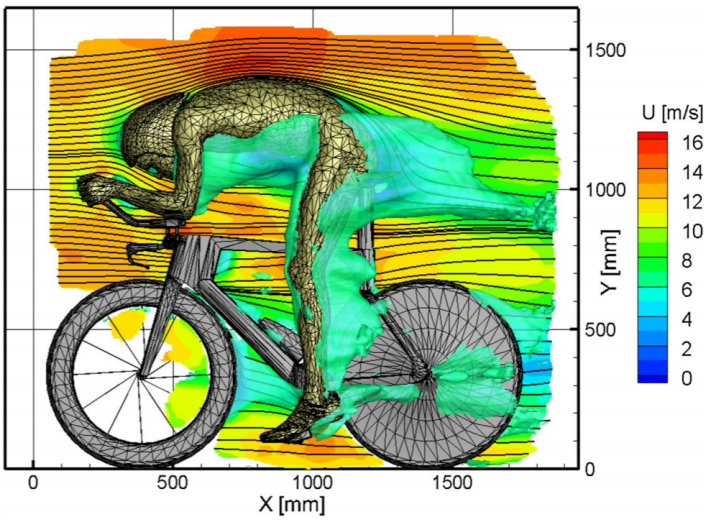

Figure 2.14: Mean velocity field at a free-stream velocity of 14 m/s displaying the stream-wise component in the centre plane along with the surface streamlines, as taken from [18]. The green iso-surfaces are shown for the free-stream velocity $U = V_\infty = 7\ m/s$.

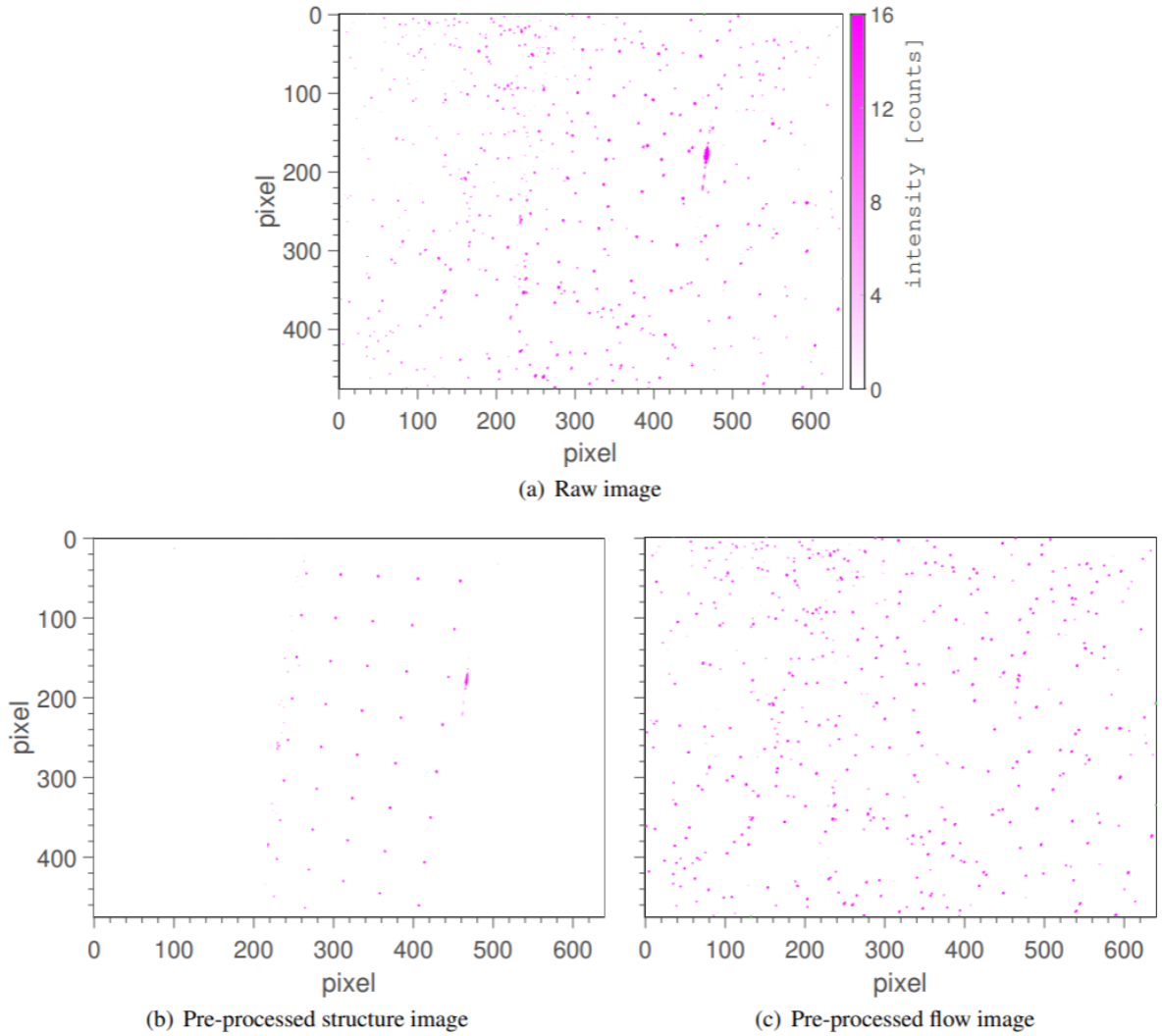

Figure 2.15: The raw image (a) showing both the tracking particles as well as the marker reflections, (b) the marker reflections after the filter and (c) the filtered flow-tracing particles image, as adapted from [29].

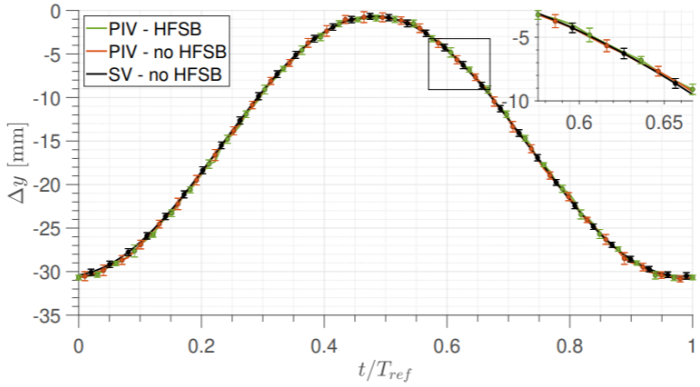

Figure 2.16: Phase-averaged structural deflection during a gust with and without HFSB, as taken from [29].

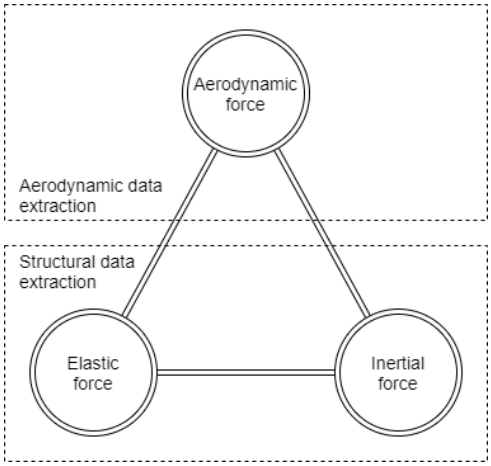

(a) The direct approach, where all forces are measured directly in the experiment.

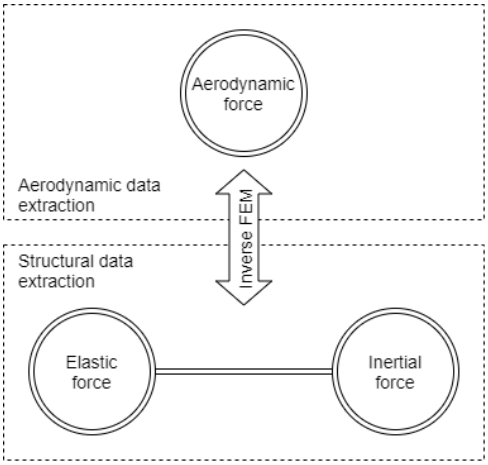

(b) The indirect approach, where either structural or aerodynamic forces are measured and the other is resolved using iFEM.

Figure 2.17: Types of approaches to the characterisation of the three aeroelastic forces in Collar's triangle.

2.2.2. Indirect Approach

The indirect approach relies on the relation of Collar's triangle where knowing either the structural or aerodynamic forces implies that also the other one may be known, since the structural forces must balance out the aerodynamic forces. Within this approach, there is another distinction. On the one hand, when knowing the aerodynamic force, it is possible to determine the structural forces. In order to distinguish between inertial and elastic forces, however, additional tools are required. This would again increase the required effort for the experimental method. On the other hand, if the structural forces are known, it is possible to determine the aerodynamic load, while being able to make the distinction between elastic and inertial loads. This indirect approach would require a coupling mechanism standing between the aerodynamic and structural forces, which would be an iFEM approach as seen in Figure 2.17b.

Roy et al. generated an iFEM method based on analytic relations which allowed them to recover the distributed force of a flat plate in flutter based on its mass distribution, the eigenfunctions and the normalised force. This force is a temporal function which was extracted from the measurements of the forced vibration [38]. The mass distribution and the eigenfunctions were found through the marker measurements from the plate. In the analytic model, the effect of aerodynamic damping was excluded when calculating the natural frequencies and damping modes. The study by Roy et al. was the first to investigate the distributed force over a plate in flutter and the analysis was performed on 12-, 18- and 24-inch plates of which the latter is shown in Figure 2.18. The marker pattern is the same on each plate. The results for each plate are shown in Figure 2.19 in terms of maximum displacement and the aerodynamic load on the plate for their respective flutter speeds. To visualise the load over an entire oscillation cycle, a time-history of deflection and respective aerodynamic load is provided in Figure 2.20 with time-steps of 0.005 s. The limits of this approach concern its analytic nature which relies on the assumption of a thin plate structure. Moreover, the authors emphasised the influence of an accurate FEM representation in such methods. Since the experiment by Roy et al. includes assumptions to set up the analytic relations, a more direct approach is desired which uses fewer modelling assumptions. The downside of these assumptions is that many aspects of the actual scenario may be lost in the process.

Similarly to the approach by Gherlone et al. where strain gauges were used in an iFEM approach to extract the shape of a cylinder based on local strains [14], the aerodynamic forces may be imposed on a FEM model to retrieve structural forces, or the structural forces are imposed on an iFEM model to retrieve aerodynamic forces. This latter direction is not as straightforward as simply imposing the structural forces, as these are not straightforward to measure locally across the span of the wing.

The issue lies in the relation between elastic forces and displacement, which is defined by the structural stiffness. While in an ideal environment where it is possible to have an exact FEM representation of a test wing and a test wing of which the deflection is measured exactly, this is not the case for an experiment. In an experiment, in first instance the FEM model may have its flaws with respect to the experimental model. In that case, even with exact experimental measurements, the iFEM approach which imposes the deflections on a model to retrieve the forces would result in erroneous force extraction. Secondly, supposing the FEM model

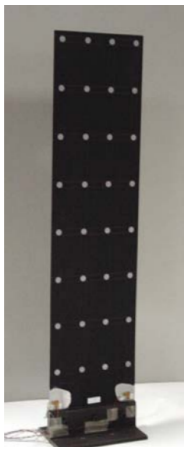

Figure 2.18: The 24-inch flutter test plate as used by Roy et al. [38].

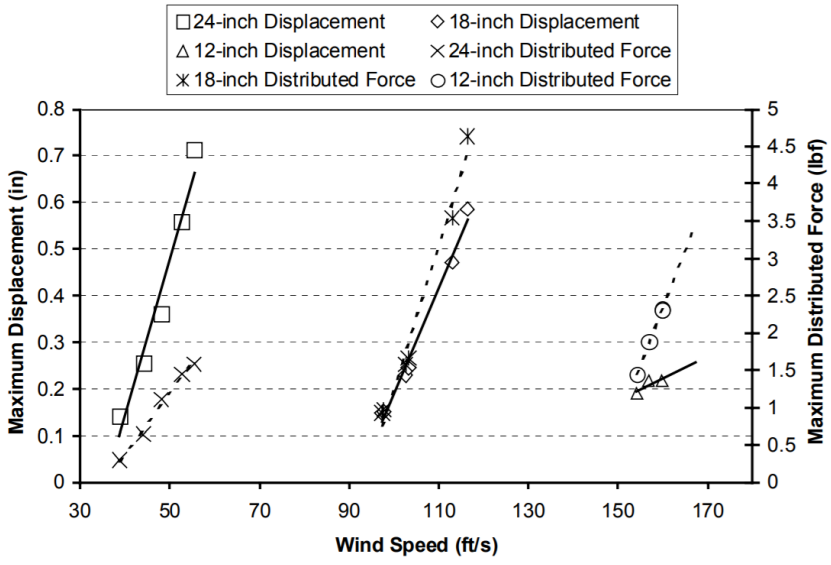

Figure 2.19: The resulting maximal displacement values (in inch) and maximal distributed force (in lbf) given for the three plates at their respective flutter speeds, from the experiment by Roy et al. [38].

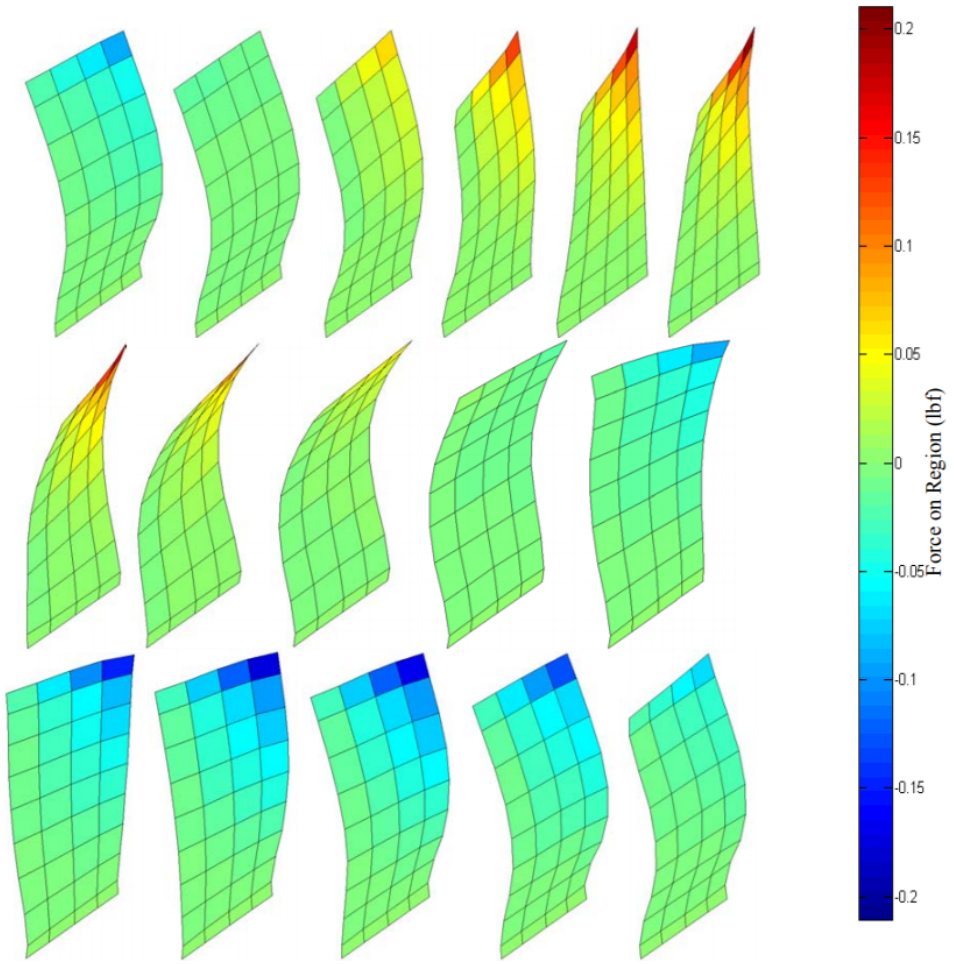

Figure 2.20: Flutter animation of the 24-inch plate with the respective distributed force as per the colour bar. One flutter oscillation is given by Roy et al. to demonstrate the extraction of aerodynamic loading from marker measurements [38]. Each frame is recorded 0.005 s after the last.

is a perfect match with the test model, due to measurement flaws and errors it is not possible to retrieve the forces by using the erroneous measurements in an iFEM approach as this would give forces that ensure an exact fit of deflection to the measured deflection – where the latter is not the exact deflection of the wing. Thus, simply deploying the indirect approach by using iFEM on a set of measured deflections to obtain the aerodynamic force is not readily possible and further research is required.

Using the novel measurement approach by Mitrotta et al. with the dual application of a PIV CVV probe to extract simultaneous flow and structural data, de Rojas integrated a simple constant-load beam model in a first attempt to extract the aerodynamic load in gust from marker-tracking data [7, 29]. The assumption in this method was that since the inertial load is larger at the tip and that the aerodynamic load is smaller at the tip, a constant load may be assumed. With the application of a tip mass in that experiment, the inertial tip load was further amplified. This approach therefore lacks the argument for applications in broader research where this assumption may not hold. Hence, a more elaborate iFEM approach is necessary to be able to accurately characterise each aeroelastic force using marker-tracking data as it is assumed that measurement errors from the markers will affect the reliability of a direct iFEM approach.

The purpose of such a new iFEM application is to be able to characterise the three aeroelastic loads from marker-based measurements in the indirect approach. Until now, either pressure taps or extensive PIV measurements were required to extract the aerodynamic force after which the inertial force could be quantified through structural deflection monitoring. As it is not always possible to perform such extensive measurements with PIV or because some test structures do not allow for intricate pressure tap set-ups, an iFEM modelling aspect must be introduced to extract the elastic loads from the deflection in order to be able to characterise Collar's triangle. To achieve this in an experimental environment where the deflection can only be measured with finite accuracy, a predictive optimisation may be considered to find a load distribution which achieves the measured deflection within a margin. This application may eventually be used in the research of aeroelastic encounters with specific interests in the evaluation of Collar's triangle throughout the occurrence, as well as in the structural design to achieve CS-25 certification.

2.3. Research Statement

The research in this thesis is proposed to find a solution to the issues on the topic of the indirect iFEM approach. In order to guide this research, a research objective is formulated in subsection 2.3.1. Research questions are then defined such that the objective can be fulfilled in a guided, step-wise manner. These questions will be shown in subsection 2.3.2.

2.3.1. Research Objective

Following the suggested approach towards the full fluid-structure interaction characterisation in gust, a research objective or research purpose is defined. The research objective for this thesis is stated as follows:

> "To develop a method to apply a hybrid numerical-experimental approach to extract the three components of Collar's triangle on a flexible wing in gust by means of an iFEM framework which returns the span-wise aerodynamic force distribution given marker-tracking measurements."

The research purpose was pursued in three main pillars, each of which has its own milestone topics:

1. Framework development phase:
    - A basic understanding of various FEM approaches is to be obtained such that an appropriate decision can be made for the FEM module of the framework.
    - Literature on the lift distribution shape curve will be studied to incorporate a mechanism which generates such a shape based on the wing's geometry.
    - The optimiser is to be set-up such that it manages to meet the deflection, while providing realistic lift distributions.
2. Numerical behavioural analysis:
    - Experimentally relevant test cases should be defined which allow for a realistic test case of the performance of the framework. For these cases, the experimental model is to be modelled in a FEM module and the lift force should be found from a reference aerodynamic model for validation.
    - A method must be laid out such that each parameter such as measurement errors can be compared to its reference case consistently.

- The various parameters which may affect the output, for example the accuracy of the FEM model with respect to the wing, of the framework must be assessed individually in order to understand the behaviour of the framework given certain circumstances.
- Using the various parameters which are expected to influence the performance of the framework in terms of experimental or numerical flaws, a test case can be generated based on numerical data such that the experimental environment can be simulated to see how the framework works in such non-ideal situations.

3. Experimental efforts:
   - An experimental data set for a static and dynamic case must be prepared such that it can be used in the framework for validation.
   - The inertial forces must be extracted from a dynamic case based on the marker-tracking data and included in the framework's optimisation process.
   - The results are to be discussed in order to evaluate the framework's performance and to make recommendations towards future experiments which may be designed in favour of the framework in terms of the results of the numerical behavioural analysis.

2.3.2. Research Questions

The research purpose comes with a series of questions which must be answered such that the purpose can be achieved. These questions, along with a brief reasoning for them, are provided here.

1. What is the best approach towards an iFEM framework which optimises a load distribution to match a measured deflection?
   (a) What prior knowledge about the aerodynamic load distribution can be used to feed into a framework as an initial estimate of the load without performing additional measurements?
   (b) Which structural numerical modelling tool is the most suitable for the FEM framework?
      i. What are the requirements for the FEM module in the framework?
      ii. To which extent does the error in the accuracy of the FEM model with respect to the experimental model itself need to be taken into account for this decision?

   The goal of this research question is to assist in the required understanding such that the framework may be developed. The framework needs to perform well when taking into account certain physical aspects concerning the lift load distribution. Furthermore, a decision must be made as to which FEM solver will be used to extract the deflection following from the estimated lift loads, based on the level of representation with respect to the experimental model.

2. What parameters in the experimental or numerical approach (e.g. measurement accuracy) may affect the outcome of the iFEM application which must be considered during an assessment of an iFEM solver to extract aerodynamic loads from marker-tracking measurements?
   (a) What (set of) parameter(s) can be used to assess the similarity between a test model and a reference FEM?
   (b) In which ways can mismatches with respect to a reference FEM be quantified in terms of those parameters?
   (c) What effects do the individual parameters have on the extracted loads?
      i. To which extent can these effects be mitigated or reduced?
      ii. What margin in the modelling mismatch can be considered to be acceptable during the application of the suggested framework?
      iii. For each of the effects, what is the physical cause of the induced error?

   Here the goal is to evaluate the feasibility of this method as a tool to analyse the aeroelastic loads from a marker-tracking-based experiment using the suggested approach with respect to mismatches in the initial reference FEM model or flaws in the measurements. It essentially serves as both a validation effort and initial uncertainty quantification for the hybrid method. Furthermore, it will guide an analysis of the consequences of the errors that could be present and specifically how they should be treated in the discussion of the results once the loads are extracted in an experimental environment.

3. How well do the forces in Collar's triangle match with the application of the suggested framework?
   (a) How well can the inertial forces be retrieved from marker-tracking measurements in addition to the aerodynamic forces?
   (b) Taking into account the errors in the FEM, what is the error in the relation of the forces in the context of Collar's triangle?
   (c) What is the influence of non-linear and unsteady effects on the feasibility of the framework?

   With this question an attempt is made at looking at how the iFEM framework works for both static and dynamic phenomena. Both unsteady aerodynamics and inertial forces need to be taken into account for a gust and this question will be the basis of a discussion on how the framework copes with the dynamic events.

3

Experimental Approach

Prior to the development of the proposed framework, it is important to elaborate on how the marker data was retrieved from a previously executed experimental campaign. This will aid in understanding the results and especially unexpected discrepancies which show up in them. Being a hybrid numerical-experimental approach, the experimental part plays a key role. As is the case with any experimental method, the measurements are imperfect and should therefore be properly discussed prior to assessment. The experimental campaign which will be considered for this document was performed by de Rojas as per [7]. This chapter will provide an overview of the key aspects to the extraction of the marker data.

To start off, the wind tunnel facility in which the measurements were made will be briefly discussed in section 3.1. Then, the wing test model used in the wind tunnel for the measurements is shown in section 3.2. The measurement techniques will be the topic of section 3.3, providing an insight into how the measurements were obtained. The measurements also required post-processing as it was found that there were errors in the retrieved data, as will be elaborated upon in section 3.4.

3.1. Wind Tunnel Facility

The wind tunnel facility used for this experimental campaign will be explained here. The specific set-up which allowed for the generation of a gust flow will also be covered.

Open Jet Facility

The experiments run for this research were performed in the Open Jet Facility (OJF) at Delft University of Technology. This wind tunnel is characterised by its large and open test-section with a closed-loop circulation system. The flow is driven by a 500 kW turbine which may generate velocities up to 35 m/s at the octagonal outlet of dimension 2.85×2.85 m^2. A schematic representation of this wind tunnel is shown in Figure 3.1. Its 13 m wide and 8 m high open test-section allows for large-scale testing, while maintaining sufficient vacant room to place the equipment.

Moreover, the nominal turbulence intensity in the OJF was found to be in the order of 0.5% [23]. This result, however, was achieved without the presence of the PIV seeding system as will be discussed later, nor the gust generator mounted in the nozzle. In the study by Sciacchitano and Giaquinta, it was found that with the presence of these two attributes the turbulence intensity is in the order of 0.8% [42].

Gust Generator

The gust generator used for the dynamic experiments in this campaign was specifically designed for the OJF as elaborated upon in the work by Lancelot et al. [21, 22]. A schematic overview of the design and implementation of this gust generator is provided in Figure 3.2.

It is mounted in front of the inlet on an aluminium frame which provides stability. This frame was specifically designed not to resonate with the frequencies which the gust generator may exert. Two active gust vanes are placed vertically within this frame, both are 2.88 m in length and are constructed with a combination of aluminium spars and foam. The gust vanes have a $NACA$ 0014 airfoil with a chord length of 0.3 m and have a

[1] As taken from: `https://www.tudelft.nl/lr/organisatie/afdelingen/aerodynamics-wind-energy-flight-performance-and-propulsion/facilities/low-speed-wind-tunnels/open-jet-facility/`; accessed on 05/11/2020.

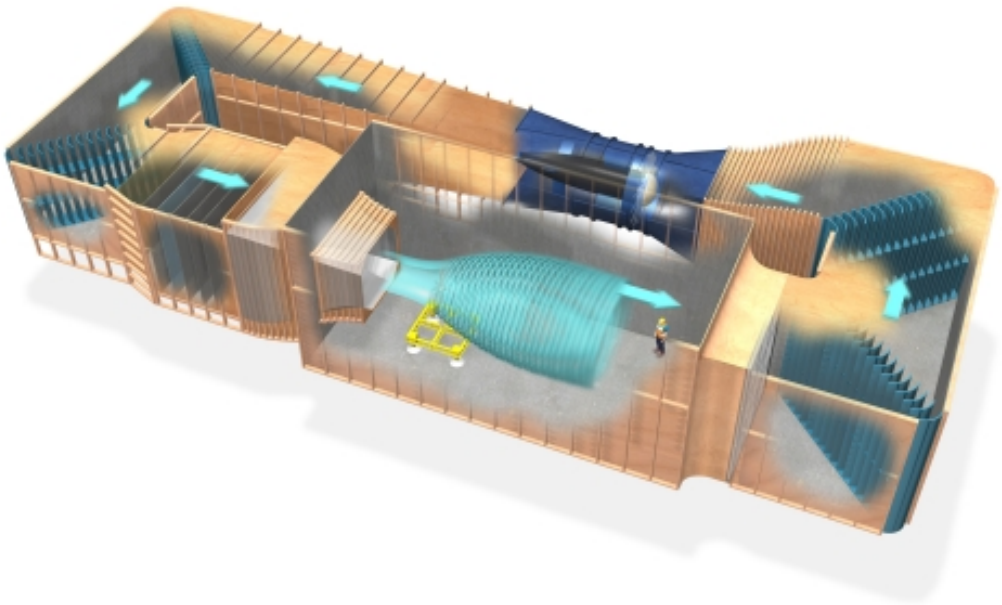

Figure 3.1: Overview of the Open Jet Facility at Delft University of Technology[1].

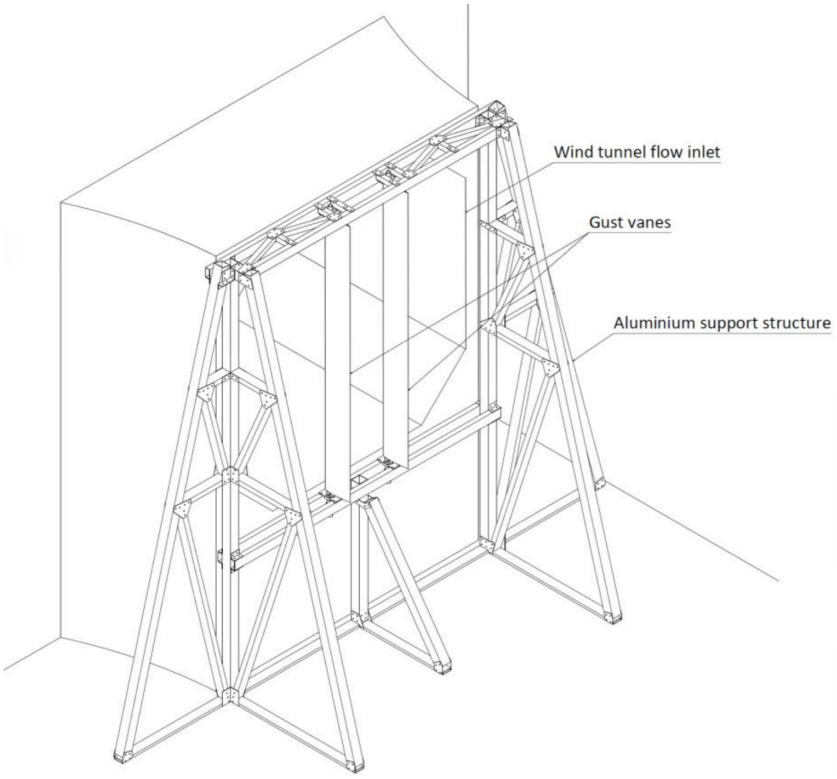

Figure 3.2: Sketch of the overview of the design and implementation of the gust generator used in the OJF, as taken from [21].

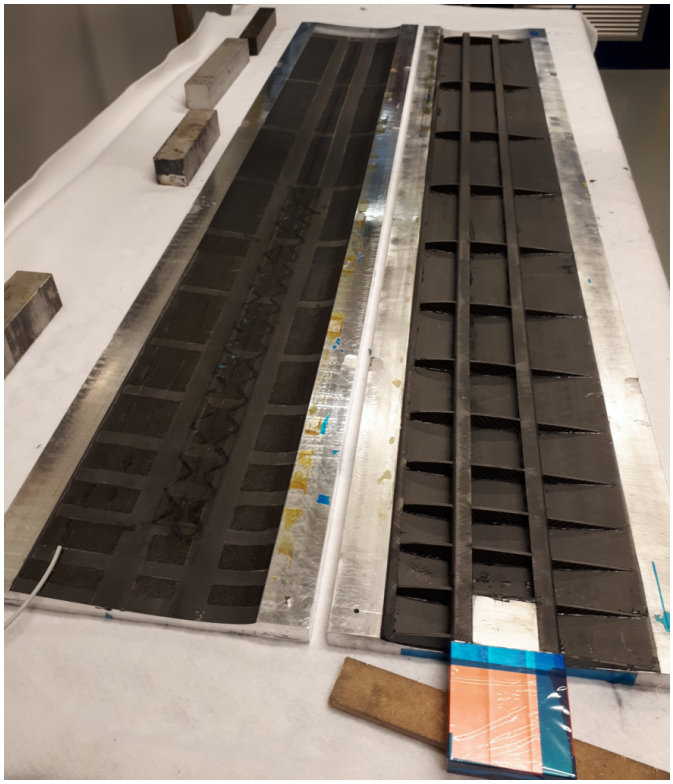

(a) Inner structure of the wing prior to bonding the two halves.

(b) Fully assembled wing as used in the experiments.

Figure 3.3: Wing structural manufacturing imagery, as taken from [29].

spacing of 0.7 m between them. The rotation of the gust vanes is controlled by a control system and actuators which allow for the generation of deterministic gust profiles through the OJF's LabView user interface. This rotation induces a transverse velocity component with respect to the free-stream direction, creating a gust. Both harmonic and 1-cosine gust profiles can be generated with frequencies varying between $0.5-10$ Hz and gust vane angle of attacks of $\pm 10°$, which defines the amplitude of the gust.

3.2. Test Model

The experimental test model which was used to obtain the measurements will be discussed here. An explanation of the flexible wing will be provided along with the wing's marker grid, 0ive FEM model and mass matrix. Any modifications to the structure will also be discussed.

Wing

The flexible wing for this campaign is 1.75 m long with a constant chord of 0.25 m and a $NACA$ 0010 airfoil. Its thin airfoil supports any thin-walled aerodynamic modelling theories such as VLM. It was designed and built by the Aerospace Structures & Materials group at the Faculty of Aerospace Engineering of Delft University of Technology. The design was made according to an optimisation process to design a wing with maximal tip displacement with minimal mass, while adhering to certain safety standards [29]. The wing's inner and outer structure can be seen in Figure 3.3. A total of 13 ribs are used across the span, with more ribs concentrated towards the root where more support is required. Two constant cross-section spars are also placed across the entire length of the wing. The composite wing is made out of a carbon-fiber reinforced epoxy, Hexcel 8552 IM7. It is a unidirectional tailored laminate and it is used for the skin, but also for the spars and the ribs. The wing is divided into three sections of equal length with individually constant stiffness properties, with the most reinforced section at the root and the weakest at the tip.

A tip mass of 0.4 kg was added to the wing tip to reduce the natural frequency of the wing such that it is within the achievable range of frequencies of the OJF's gust generator. Moreover, in order to clamp the wing an aluminium block was added to the bottom which increased the wing's total length to 1.8 m, though it is considered to be perfectly rigid and thus taken out of the measurements to correspond to its equivalent FEM

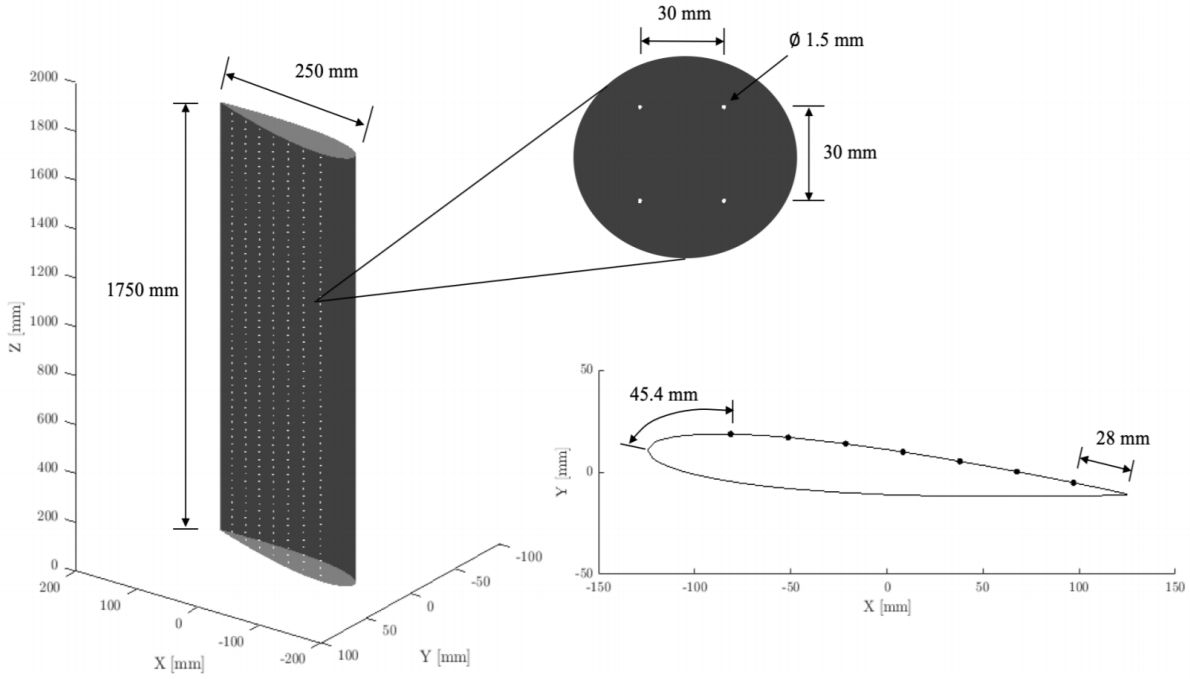

Figure 3.4: Wing and marker grid dimensions visualised, as taken from [7].

model of 1.75 m, on which more later. Finally, a zig-zag trip strip is glued to both the pressure and suction side at 5% and 65% chord, respectively, and with a thickness of 0.2 mm and 0.5 mm which ensures the transition to a turbulent boundary layer. These strips are excluded from the analysis, which may induce discrepancies with respect to numerical models such as VLM to calculate the aerodynamic forces as they do not consider the transition.

Marker Grid

The measurements performed for the deflection data is based on marker-tracking in time and space, on which more later in section 3.3. Here, the marker grid which is painted on the wing will be discussed. The marker grid was spray-painted on both sides of the wing using a laser-cut 0.4 mm thick cardboard template. The template of the marker grid was flexible such that it can follow the curve along with the airfoil profile of the wing.

The diameter of the markers may not be too large as this may reduce the capability of the PIV system to visualise flow-tracer particles. On the other hand, the diameter cannot be too small as this will reduce the visibility. It was found in the work by Mitrotta et al. that a marker diameter of 1.5 mm works well for this type of application [29]. One may note that the coordinate system for the wing as defined in the figure is used in the report. Moreover, the marker spacing is 30 mm in a rectangular pattern as shown in Figure 3.4 along with the wing's overall dimensions. A spacing too large would not provide sufficient resolution of the wing's deflection, whereas too small would clutter the PIV view with markers. Finally, the marker grid commences at a contour-based distance of 45.4 mm aft the leading edge.

Wing Numerical FEM Model

The wing model used for the numerical campaign and the framework simulates the one used for the experiments such that its structural properties are represented accordingly. To calculate the equivalent beam stiffness properties, a cross-sectional modelling tool is used for thin-walled composite beams. It was developed by Ferede and Abdalla as per [11] and it provides the Timoshenko stiffness properties for each section. It takes into account the materials used, the geometry and the lay-up of the composites. Furthermore, it also generates the global stiffness matrix for the wing, which is here modelled as a beam in 6 DOF per node (force and moment in x, y and z). The wing is modelled with a total of 44 nodes in addition to the root: the first two sections each have 15 nodes (with a separation of 38.9 mm) and for the third section 14 nodes are used (with a separation of 41.7 mm). The deflection may be calculated for a given load, as will be further explained in chapter 4.

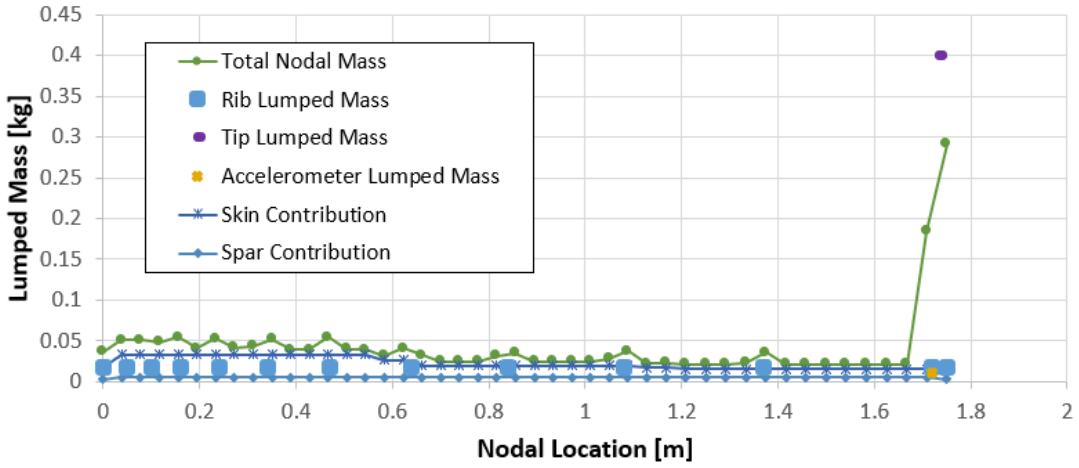

Figure 3.5: Total nodal masses which represent the mass distribution along the wing, taking into account the various contributions which make up the total wing's weight.

Mass Matrix

The mass matrix $\mathbf{K_M}$ as used to calculate the inertial forces is generated by considering the construction materials of the wing. It is not a mass matrix in its conventional sense. Here, $\mathbf{K_M}$ represents the distribution of the mass across the span, or in other words each node is represented as a lumped mass to which the nearby structural mass is projected. The volume of the used materials is based on the layer thickness of the wing and how many layers are used per region. With the density of the composite known, it is possible to arrive at the mass of the structure. For the ribs, it is known that the weight of one rib was 17.2 g and for the two accelerometers at the tip, they have an individual weight of 5 g. The ribs, accelerometers and the tip masses are taken into account as lumped masses. These were then projected with a linear weight to the closest node couple. A visual representation of the wing mass distribution is shown in Figure 3.5. Each mass is projected onto a lumped mass, but the continuous contributions such as the skin and spars are plotted as a line with lumped masses to visualise this. The total mass excluding the 400 g wing tip mass which was obtained through this approximation is 1.47 kg whereas the measured wing weight is 1.44 kg, also excluding the tip mass. Hence, it is assumed that the numerical approximation of the wing mass distribution closely represents the actual distribution.

3.3. Measurement Tools

For the experimental measurements required for the framework as input and validation, two measurement systems are required: PIV for the input and the force balance which can provide an initial validation for the applied forces. Due to the scope of this thesis, the measurement techniques used to validate the combined approach of PIV and marker-tracking will only be briefly discussed based on dedicated research on that topic.

PIV System

The entire PIV system consists of three main components: the seeding system, the imagery and illumination device, and finally the robot arm. Each component will be discussed in a concise manner. The entire PIV set-up as explained below is shown in Figure 3.6.

PIV relies on the presence of flow-tracing particles to resolve the velocity field. To provide seeding on larger parts of the airflow, a seeding rake specifically designed by the Aerodynamics department of the Faculty of Aerospace Engineering at Delft University of Technology was deployed for this campaign. Ideally it may cover an area of up to 1×0.5 m^2, but research has shown that due to deterioration of the nozzles this cannot be achieved [34]. For this campaign, a quarter of this area was considered usable. The seeding rake is positioned in the settling chamber of the OJF as seen in Figure 3.7, where it introduces minimal turbulence intensity into the flow. It is mounted on an aluminium frame such that it can be moved vertically to cover various sections of the wing aft of the outlet. The seeding rake itself produces helium-filled soap bubbles (HFSB) and their buoyancy and production density may be adjusted from the control room of the OJF by controlling the supply of soap and helium to the seeding rake. This type of bubbles is used for their mechanical properties which have a low response time and have favourable light-scattering properties in PIV campaigns.

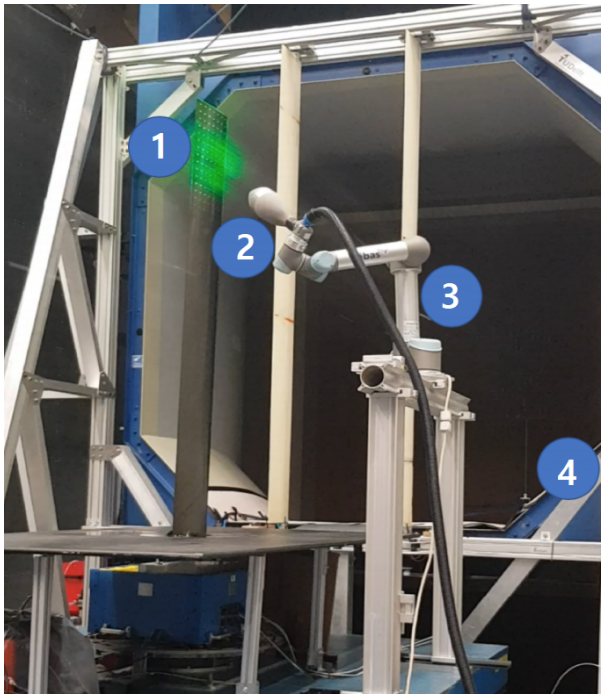

Figure 3.6: The PIV system as used in the experimental campaign with (1) the HFSB seeding rake, (2) the UR-5 robot arm, (3) the CVV probe and (4) the truncated pyramid measurement volume, as adapted from [7].

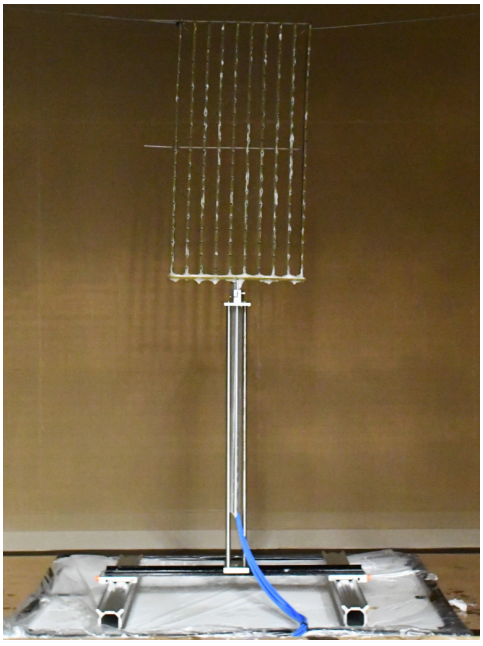

Figure 3.7: The seeding rake as used in the experimental campaign in the OJF's settling chamber, as taken from [28].

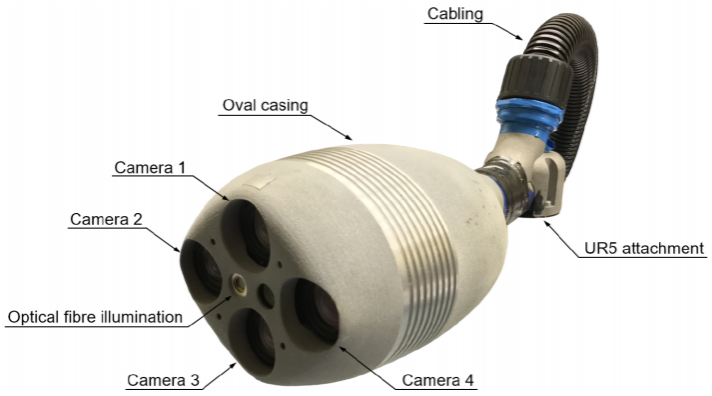

Figure 3.8: The coaxial volumetric velocimetry or CVV probe as used in the experimental campaign, as taken from [34].

The optical capturing and illumination of the particles is done by using a CVV probe as previously discussed in subsection 2.1.2. The CVV probe as shown in Figure 3.8 is a Minishaker Aero by LaVision and it features four complementary metal-oxide semiconductor cameras and the illumination source in an oval housing to minimise flow interference. The cameras are mounted under a low tomographic angle around a common axis. This common axis is also the axis of the source illumination, which comes from a Quantronix Darwin Duo Nd:YLF laser with a wavelength of 527 nm, a frequency range of $0.2 - 10$ kHz and a maximal power of 25 mJ. The laser beam itself comes from the laser head at the bottom of the robot arm, where it is safe from the measurement area. The beam travels through the optic fibre to the CVV probe where it is shattered into a conical shape through a set of spherical lenses. This arrangement produces a truncated pyramid measurement volume as seen in Figure 3.6. The laser and the cameras are connected to the acquisition computer which allows for the triggering of the laser and the cameras at the right times to capture illuminated particle imagery.

Finally, the CVV probe is attached to a UR-5 robot arm which guides the probe around the desired measurement locations. This robot by Universal Robots has 6 DOFs with a maximal reach of 850 mm from its base. The convenience of a robot-guided probe is that with appropriate software, large-scale measurements may be conducted without the need of repeated calibrations at each location. The software used in this campaign is RaboDK 3.2 which allows the test section to be modelled in a 3D environment. The robot can then intuitively navigate this environment through the acquisition computer. Since the robot arm has its own reference frame based on the location and rotation of its joints, the software comes with a function to automatically transform the coordinates to a global reference frame given the position of the robot arm with respect to the measurement objects.

Force Balance

The test model is mounted on a force balance which allows for the measurement of the total applied load in six components (force and moment in x, y and z) at the root of the wing. A splitter plate is also present to separate the test model from the clamping system and the force balance. The wing is clamped on the aforementioned aluminium block which also serves as the support of the entire model. The force balance itself can be rotated as it is mounted on a rotation table in order to adjust the angle of attack of the wing. Lastly, this entire system is put on a hydraulic table which may lift the model such that the system is aligned with the jet from the wind tunnel outlet. It must be noted that the wing's root chord is at a distance of 333.5 mm above the reference axis of the force balance. In the measurements of the root moment, this distance needs to be corrected for such that a comparison can be made.

Measurement Validation Equipment

In the thesis of de Rojas [7], the same set-up was used to assess the performance of the marker-tracking technique in combination with PIV for a dynamic gust case. In that study, the goal was to evaluate the feasibility of using the integrated aerodynamic and structural measurement technique as a stand-alone approach for the acquisition of said data. Hence, it needed to be validated with techniques which were known to provide accurate results during measurement. A brief discussion is held to support the conclusion of de Rojas in [7], claiming that the combined technique may be used as a stand-alone technique for an unsteady dynamic case.

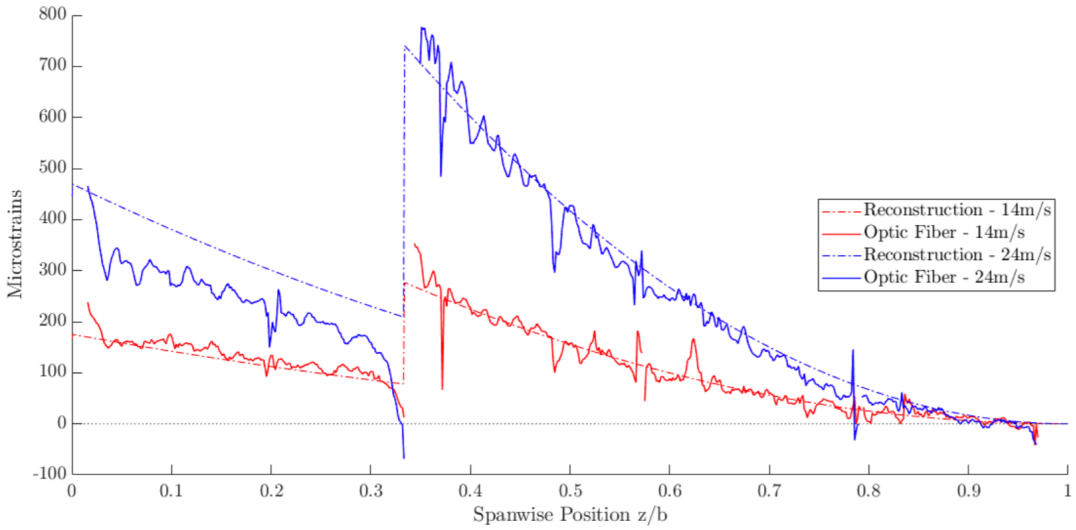

Figure 3.9: Comparison of the strains from the marker-based wing reconstruction and the optic fibre in the wing at two free-stream velocities and $AOA = 5^{\circ}$, as taken from [7].

In first instance, the deflection from the marker measurements was compared to the strains obtained from an optic strain fibre which was mounted on the wing. It can be spotted in Figure 3.3a, where at the bottom-left a white cord extends from the wing. The wing was reconstructed based on the deflection measured from markers and an optimisation process which made use of a shape function with an initial constant load assumption. The strain results from this reconstructed deflection were then compared to the strains obtained from the optic fibre as shown in Figure 3.9. The results show that marker-tracking can be used as a stand-alone approach for the deflection in combination with PIV [7]. Secondly, accelerometer data was used from the accelerometer at the leading edge of the wing tip. The comparison between this data and the data from the second derivative of the marker positional measurements is shown in Figure 3.10. Note, for this figure the position in time was fitted with a polynomial of which the second derivative in time is used for the acceleration.

3.4. Post-Processing

Given the focal point of this thesis being the proposed framework and its evaluation in practice, the post-processing techniques used for this data will be covered only in a concise manner. The data used for this evaluation comes from the experimental campaign as performed in [7]. The reader with a particular interest in the post-processing techniques is referred to the cited document for an in-depth discussion.

Particle & Marker Separation and Tracking

The nature of the used measurement technique is to combine particle and marking tracing techniques into one integrated system. This gives rise to the need to separate the two for the processing of the tracks of each, such that both aerodynamic and structural data may be acquired in a similar manner as discussed previously in the report by Mitrotta et al. [29].

It is assumed that the time scale of the markers is much larger than that of the particles, as the velocity with which the structure moves will be smaller than the flow velocity. With this in mind, it was possible to extract the HFSB particles from the PIV images with a Butterworth high-pass filter [43]. This filter's primary use is to remove the unwanted reflections in the background of the PIV images by considering the pixel intensity in the frequency domain. Davis 10 has a built-in function to apply this filter with settings such that the application was optimal for the extraction of the HFSB particles.

Then, a symmetrical minimum time filter was used to also differentiate the marker tracers from the HFSB tracers. In order to improve the positional information quality of the marker images, operations such as smoothing and the reduction of reflection were performed. It was required to improve the image quality in order to perform the PIV algorithm Shake-The-Box (STB). This allowed for the complete distinction between the structural and aerodynamic markers for which a result is shown in Figure 3.11.

STB allows for the generation of the actual tracks of the traced particles and markers from PIV imagery.

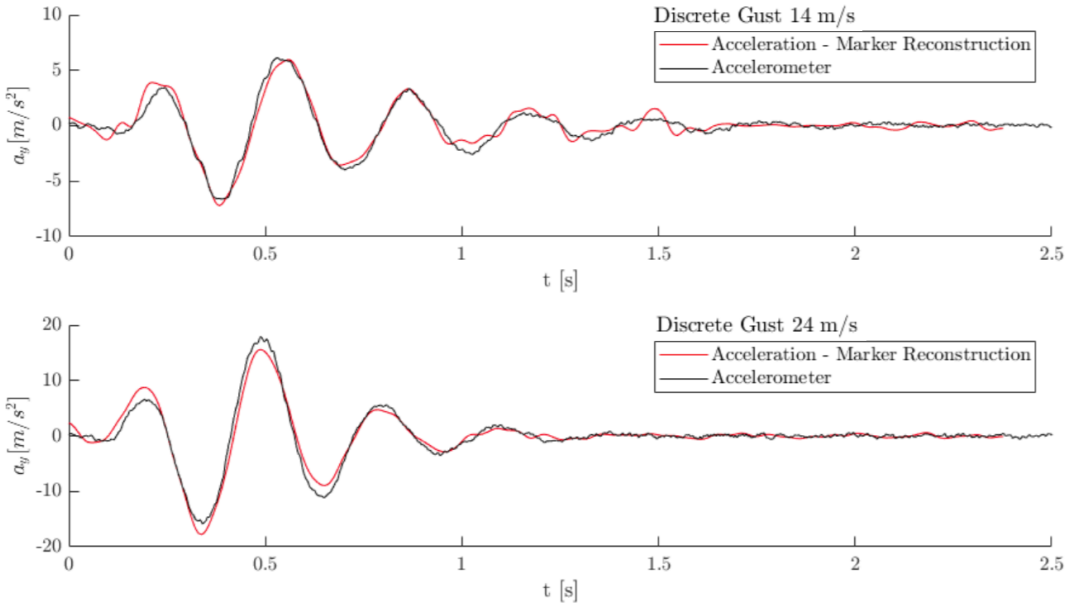

Figure 3.10: Comparison of the acceleration in y from the marker-based wing reconstruction and the accelerometer at two free-stream velocities and $AOA = 5°$, as adapted from [7].

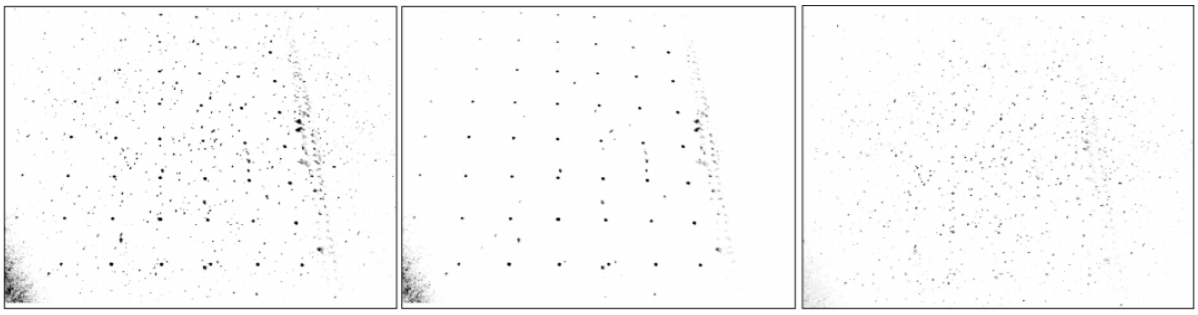

Figure 3.11: The separation of the particles and the marker-tracking with an inverted grey-scale, as taken from [7]. The image on the left shows the raw imagery from PIV, the middle image shows the marker grid on the wing and the right image shows the HFSB tracers.

A more elaborate discussion on this topic may be found in the work by Schanz et al. [40]. In short, this approach relies on the prediction of the position of particles which have been tracked and further refining this position by image-matching schemes. One shakes all particles inside a box-volume until a fit is obtained. This approach has limitations in terms of measurement velocities. As a specific box dimension must be defined, if a particle travels through a box prior to being captured within the box multiple times, the particle will go unnoticed by the algorithm. This limit depends on the acquisition frequency of the optical set-up. For the set-up of this experiment, previous work by Jux et al. and Saredi et al. has shown a feasible velocity of $V_\infty \leq 15\ m/s$ [18, 39]. With this campaign being performed with wind-speeds of up to 14 m/s, local velocities may exceed this limit around the airfoil. Hence, this increases the expected faulty or lacking tracks in the analysis. Since larger deflections from larger lift forces provide more prominent aeroelastic insights, the wind-speed was chosen not to be reduced [7]. Finally, STB provides the information of the motion of a particle in a Lagrangian reference frame. In order to ease visualisation and handling of the obtained data from STB, it is transformed into an Eulerian reference frame with the application of ensemble averaging.

PIV Processing

In terms of the post-processing of the HFSB tracers for this document, it is noted that with the application of the Kutta-Joukowski theorem it was possible to obtain the circulation. Since the PIV measurements were made on both sides of the wing for a small section along the span, a contour could be drawn around the respective chord section in order to derive the circulation. Based on the calculation of the circulation with Equation 3.1, it was possible to then obtain the sectional lift in terms of lift per unit span by applying Equation 3.2 which follows from the Kutta-Joukowski theorem. In these equations, C is an arbitrary contour around the section of interest, $\vec{u}$ is the velocity along a line segment $\vec{l}$ which is positive in the clockwise sense, Γ is the circulation and L' is the lift per unit span.

$$\Gamma = \oint_C \vec{u} \cdot d\vec{l} \tag{3.1}$$

$$L' = -\rho_\infty V_\infty \Gamma \tag{3.2}$$

Marker Processing

The resulting tracks from the STB algorithm for the markers had three flaws which needed adjustment. First, there were outliers in the tracks which were caused by reflections and other imperfections in the imagery. By looking at the length of such tracks, it was found that they were shorter than the length of actual marker tracks. This knowledge was used to filter them out. Secondly, certain tracks had gaps in them due to an instantaneous lack of measurement or loss of sight. A stitching algorithm was used to resolve this issue by looking for a nearby track in a 3D volume around the last measured marker and ensuring this track is in the future of the respective broken track. Finally, as seen in Figure 3.12, when plotting the marker grid for the wind-off case in which one would expect a straight wing, it was noticed that the markers were bent from the theoretical position. Later, it was found out that a faulty joint in the robot arm likely caused this error. Since it was a systematic error in each measurement, the relative displacements during wind-on measurements with respect to this error could still be measured following a reconstruction of the wing to fit the erroneous wind-off measurements. These relative displacements are then considered to be the actual displacement of the markers. This process is shown in Figure 3.13.

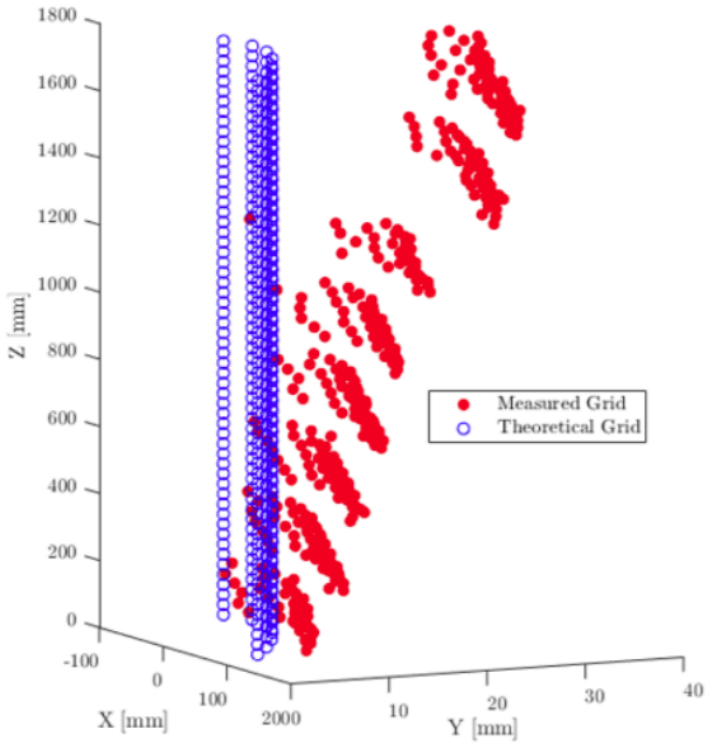

Figure 3.12: The theoretical wind-off marker grid vs. the measured marker grid, as taken from [7].

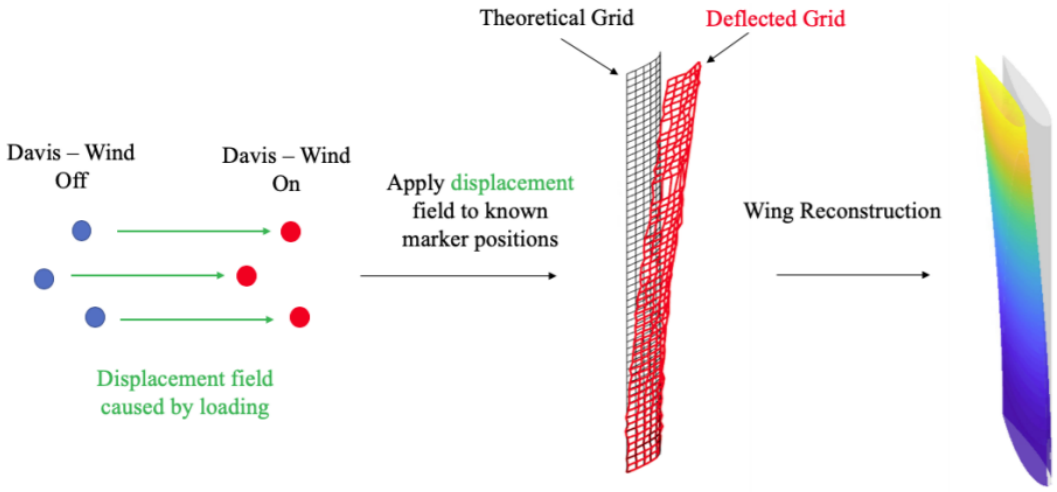

Figure 3.13: Wing reconstruction approach to measure the relative wind-on displacement of the marker grid with respect to a reference wind-off measurement, as taken from [7].

4

Framework Development

With the research purpose defined in chapter 2 as:

> "To develop a method to apply a hybrid numerical-experimental approach to extract the three components of Collar's triangle on a flexible wing in gust by means of an iFEM framework which returns the span-wise aerodynamic force distribution given marker-tracking measurements."

This chapter will focus on the development of a framework to fulfil this purpose. In short, this framework is to produce the aerodynamic lift distribution given a set of deflection measurements in addition to the computation of the inertial forces from the marker-tracking measurements. Its generic approach will initially be explained in section 4.1. The design considerations which were made prior to the actual development will be discussed then in section 4.2. Next to this, the flowchart of the developed framework which will be tested in its capability of fulfilling the research purpose will be presented in section 4.3. The overall reasoning of the working principle will be the topic of this section and each global step will be explained. The goal of this chapter is to provide the reader with the necessary insights such that the remainder of the report will be understood in terms of the operation of this framework.

4.1. Framework Approach

To fulfil the research purpose as depicted above, the framework must meet certain requirements in its approach. The purpose is divided into three pillars: Collar's triangle characterisation, marker-tracking and iFEM modelling optimisation. A brief discussion is held on each pillar to introduce the overall approach of the framework development to these requirements.

- **Collar's triangle characterisation**: This pillar implies that the ultimate goal of the framework is to be able to make the distinction between the elastic, aerodynamic and inertial forces with the application of the framework. Hence, it is necessary to have an individual approach for two of these three forces such that the third can be quantified following the relation of Collar's triangle. The output of the framework is thus the quantification of two of these three forces such that through Collar's triangle the third may be found.
- **Marker-tracking**: To achieve the characterisation of two forces, the framework must rely on marker-tracking according to the research purpose. This input data is generated in a wind-tunnel experiment with a flexible wing model which has its surface covered in markers, these are tracked by an optical system as explained in chapter 3. Using this marker-data, it is possible to extract the local displacement, velocity and acceleration of the wing at discrete markers. From the acceleration of these markers, one may also calculate the inertial force when a mass distribution is known. This is how the inertial force will be calculated using the framework. Secondly, using an iFEM approach, it is possible to also extract the aerodynamic forces.

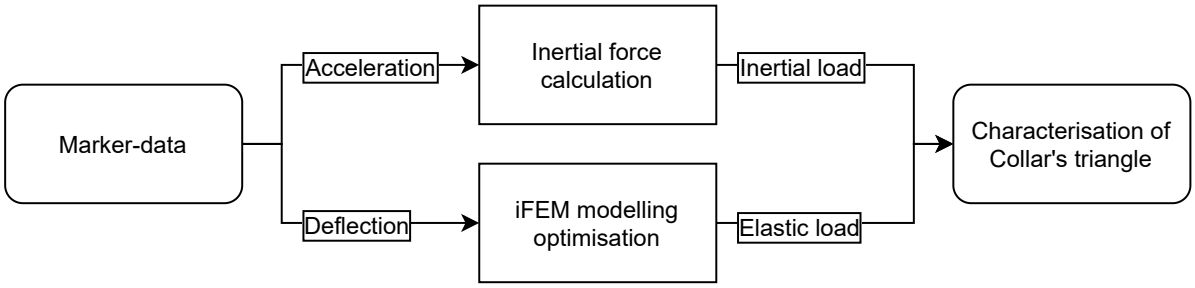

Figure 4.1: Schematic overview of the proposed framework.

- **iFEM modelling optimisation**: This framework uses iFEM modelling to extract the applied load – the aerodynamic load – given the deflection of the wing. Using the relation between the deflection, the stiffness matrix and the applied load, this may be achieved. By implementing an optimisation which has as variable the applied load and as objective function the difference between the resultant deflection and the marker-deflection, the applied load is altered until the desired deflection is achieved. When a close match is found between the resultant and measured deflection, the applied force is assumed to be equal to the experienced load by the measured deflection.

Based on these three pillars, a general-purpose schematic overview of the proposed framework can be made such that its requirements are met. This scheme is provided in Figure 4.1. Essentially, it is required that marker-tracking data is processed in such a way that acceleration and deflection can be extracted. Then, the acceleration may be used to calculate the inertial force. The deflection in turn is used to extract the elastic loads in the structure. Following from these two forces and Collar's triangle, the aerodynamic load may then be extracted.

4.2. Preliminary Design Considerations

Prior to the development of the framework, a few design considerations were made which were later incorporated into the framework. In order to provide a better understanding of how the framework was set up, the main points will be briefly touched upon here.

FEM Beam Modelling

In order to obtain the deflections from the optimised forces, a FEM module is required. In the work by Roy et al. where the distributed force was calculated with an inverse method in flutter, a shell model was used based on analytic relations [38]. Prior to using the proposed framework on a similar thin-plate shell model or on a full-scale shell wing model, the framework is proven for a Timoshenko FEM beam model. One of the leading arguments is that for this study, the lift distribution in a span-wise sense is of interest. While a full shell model may improve the FEM accuracy, an accurate beam representation is assumed to provide a similarly accurate representation of the span-wise lift distribution. Furthermore, with the availability of the model's global stiffness matrix, the forces can be imposed in a direct sense and no further modelling is required. As such, the application of an auxiliary model such as the moment-area method or a FEM program such as MSC.Nastran is superfluous. The beam model for the experimental wing for this study was generated using the PROTEUS framework as described by [11], which includes a cross-sectional modelling tool. It provides the Timoshenko stiffness matrix in 6 DOF on which the forces are imposed for deflection analysis. The DOF are defined by the force and moment in x, y and z.

For the wing model used in this report, as shown in section 3.2, it was found that the twist induced by aerodynamic moments is negligible. As such, in the framework, the aerodynamic moment induced by the airfoil is ignored. The airfoil is a $NACA$ 0010 airfoil, which naturally has a low moment coefficient. The torsional stiffness of the wing itself further reduces the influence of the small coefficient. Moreover, since the wing has no taper ratio nor sweep angle, the aerodynamic moment exists solely of the contribution by the moment coefficient. Next to this, the wing has an-isotropic composite lay-up, though the bend-twist coupling of the wing itself was also found to be sufficiently small to be considered negligible. All this is shown in Figure 4.2, where the wing tip displacement varies from 111.1968 mm without bend-twist coupling to 111.1973 mm with such coupling under a VLM-predicted load. This difference in the order of 0.001 mm is not relevant as the framework is not expected to take such small deflections into account. In terms of

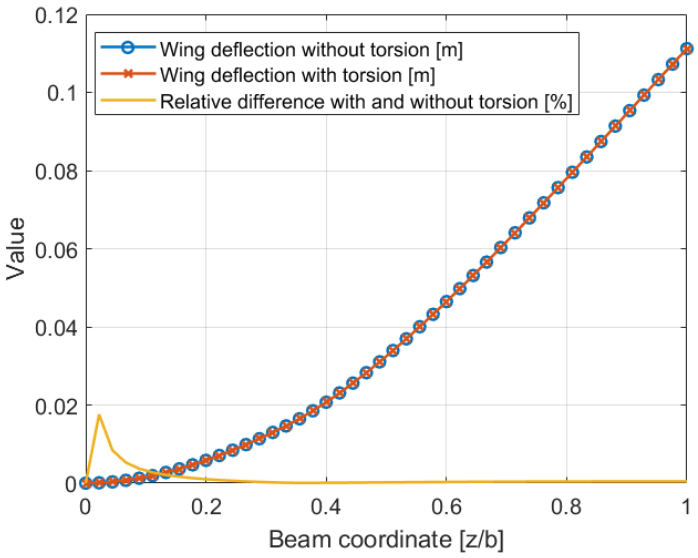

Figure 4.2: Plots of the wing deflection for a case with VLM-predicted lift for 24 m/s and $AOA = 7°$, with and without twist from torsion which would induce bend-twist deflection. A third plot shows the relative difference between the two in percentages.

relative difference between the two, a maximum of 0.02% is reached near the root, where it further flattens out towards the tip. This proves that the effect of torsion and the bend-twist coupling may be ignored. Hence, for other wing models, it should be noted that torsion may affect the measured deflections by twisting the wing in a more significant manner especially in the presence of high-lift devices or sweep angles. To sum up this discussion, the effect of twist will be ignored in this study.

Load Distribution Prediction

As will be covered later, the optimisation process makes use of a prior estimate on the lift distribution to make a first guess in order to avoid large deviations from it. In the process of development of this framework, a total of three options were considered: no prior estimate, a constant load and finally a shape function. These will be briefly elaborated upon.

In a straightforward manner, a case without a prior estimate is likely to have a load distribution with an arbitrary shape with no physical interpretation which is closely dependent on how the optimiser varies its input. With smaller tolerance levels, this will become increasingly arbitrary as it makes an attempt at converging towards the provided deflection solution which with erroneous measurements is incorrect and will thus generate forces that do not represent the actual load distribution. Hence, it is required to include a prior estimate to guide the optimisation in the right process

For the case of a constant load as starting point for the optimisation process, the theoretical root lift force was taken to be the ideal approximation for the entire wing. The reasoning being that in an ideal case, the wing would indeed have a constant lift across the wing as there would be no 3D wing loss effects. Also, it was hypothesised that with the constant load being the wing's real local maximum force, the optimisation would only have to adjust the forces towards the tip as these have more losses. Additionally, it was considered to take the average of the sum of the lift force measured by the force balance, but for the sake of relying solely on the marker measurements from an empirical standpoint, this was not opted for. This approach also has a flaw in that the force will only be correct locally near the tip, where the force drastically drops. Hence, the optimiser would have a larger region where it needs to reduce the force at a large scale, whereas the constant root force assumption implies a fairly constant error until the tip region is approached.

The final option consists of using a shape function which represents the lift distribution in a theoretical environment. Using a polynomial fit was also considered, but a theoretical framework which incorporates certain aerodynamic principles was assumed to have better results across more cases. A fit function would be a good option if the same wing was used in the same scenario, for which empirical data on the lift distribution is already available. It would then be possible to fit to this data and use the fit in the optimisation process. Considering the fact that without other measurements, only the geometry of the wing is available, it was required to use a theory which takes into account the geometry of the wing. The most accessible option

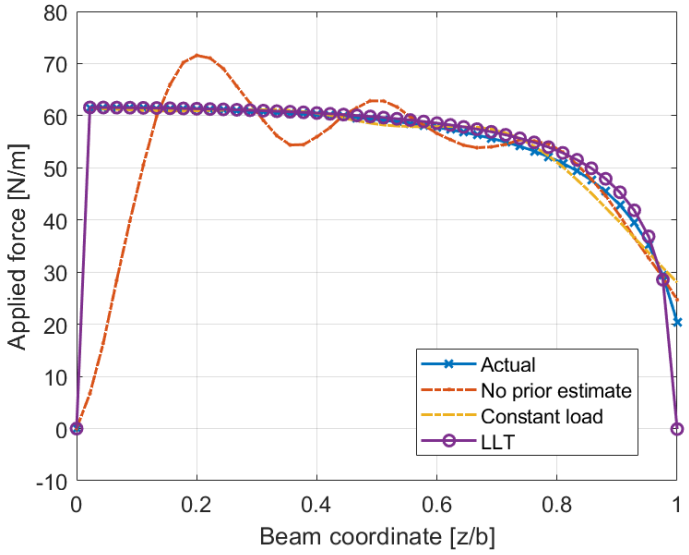

Figure 4.3: Plots depicting the resultant applied force as extracted from the framework with varying prior estimate considerations. The actual applied force was taken from VLM for the FEM wing with $AOA = 7°$ and $V_\infty = 24\ m/s$.

with low computational requirements which provides a shape function based on the wing's geometry is the lifting-line theory. As explained before in subsection 2.1.1, a series of coefficients is used which describe the lift distribution along the span of the wing. The exact approach of this implementation in the optimisation will be shown later in subsection 4.3.1.

A plot with the framework's output for each approach is shown in Figure 4.3, where the actual applied force from VLM with $AOA = 7°$ and $V_\infty = 24\ m/s$ is shown with the FEM wing model as discussed in section 3.2. This reference case will be further explained later. The resulting output of the framework's optimisation process as will be explained in the following sections is plotted for each aforementioned case. Clearly, the case with no prior estimate shows a general trend which matches the shape of the actual distribution, but has large local deviations and is thus not a good solution. The case where the starting force distribution was a constant load has a good match near the root and its accuracy deteriorates towards the tip region. It is noted that the framework was run with the initial estimate being a constant load, which was then optimised to more closely match the deflection. Overall, the LLT-based prior estimate shows great correspondence across the entire wing. It is noted at this point that the tip load from VLM does not equal zero as the force across the final wing element is projected onto the last node. The LLT curve does not take this into account, which is why it shows zero lift at the tip. Considering that this is the case for experiments, the LLT approach shows a good result considering that only the deflection and geometry of the wing was used. Another key take-away is that it clearly shows that with increasing levels of fidelity for the prior estimate of the load distribution, the solution approaches the actual values better.

Two Separate Optimisation Loops

The relation between the deflection of a structure and the resulting elastic loads imply that an optimiser without a prior estimate would attempt to fit exactly towards the measured deflections which may have random errors. These random errors would then create large local force variations to meet the deflections, as opposed to a smooth loading distribution as one would expect in an aerodynamic situation. Two approaches to counter this issue were considered.

Initially, it was assumed that by dividing the optimisation into two loops one could avoid such extreme behaviour. In the first loop, a prior estimate about the lift distribution from LLT is used to approximate the overall deflection based on an ideal load distribution which corresponds to the wing's geometry. This lift distribution would be scaled by the first optimisation loop such that the deflections are optimised towards the measured ones. In the second loop, the input would then be a scaled version of this ideal curve and this loop will then individually tune each force in an attempt to match local deviations in deflection further.

The second consideration towards a solution for the issue regarding the relation of deflection and force is to not use a small tolerance level for either optimiser. Several cut-off mechanisms exist which will cause

the optimiser to stop, but the driving ones are the tolerance of the objective function and the tolerance on the smallest adjustment in the input value. It is suggested that finding a balance between these two values will allow for a robust framework. A relation between the maximum deflection of the beam and the tolerance on the objective function is hypothesised to exist which will allow for each case to run smoothly. Lastly, the tolerance on the smallest variation in input is assumed to be related to the deflection and the stiffness of the matrix. In later studies, however, these relations between the tolerances and the stiffness of the model to achieve robustness may be defined when more cases are considered.

Including the Inertial Load

The nature of the marker measurements allows for the calculation of the marker's acceleration as a function of time, as it tracks the marker's location in time, too. Hence, with the mass distribution $\mathbf{K_M}$ and the acceleration of the markers, the inertial force $\mathbf{F_{inrt}}$ may be computed with the relation of Equation 4.1 based on Newton's second law of motion $F = m\ddot{x}$. Here, $d^2\mathbf{d}(\mathbf{z},\mathbf{t})/dt^2$ is the acceleration of the markers with $\mathbf{d}(\mathbf{z},\mathbf{t})$ the span-wise deflection in time. The acceleration will always be in the opposite sense of the deflection, implying that the inertial force attempts to reduce the deflection. Assuming that the mass matrix represents the actual wing model, the only error in this calculation for the inertial forces is the measurement uncertainty of the markers. Here, statistical averaging such as phase-averaging or taking multiple measurements may reduce this random error.

$$\mathbf{F_{inrt}} = \mathbf{K_M} \cdot \frac{d^2\mathbf{d}(z,t)}{dt^2} \tag{4.1}$$

The framework takes the inertial force into account directly from the calculation as per Equation 4.1 and is not adjusted in the optimisation for two reasons. Firstly, by optimising the combination of the aerodynamic and inertial forces, it would no longer be possible to fulfil the research purpose as the distinction between the aerodynamic and inertial force would be unclear. The characterisation of the three aeroelastic forces would then be impossible. Secondly, by tuning the inertial forces to the deflection measurements, the error of the measurements is used twice. Initially in the calculation of the inertial forces and a second time by optimising the deflection – thus the force – to a measured deflection. In a nutshell, a strong argument holds to apply the most straightforward approach to include the inertial forces by calculating them directly from the computed marker accelerations and the mass matrix. Hence, the optimisation process has no effect on the inertial force.

The manner in which the inertial loads are taken out of the assessment for the aerodynamic load is as follows. By using the relation between the applied force $\mathbf{F}$, the stiffness matrix $\mathbf{K_S}$ and the resultant deflection $\mathbf{d}$ given by Equation 4.2 in addition to the separation of this force $\mathbf{F}$ in inertial and aerodynamic forces given as $\mathbf{F_{inrt}}$ and $\mathbf{F_{AD}}$, a linear analysis can be performed to deduct a suitable method for the separation of the inertial and aerodynamic loads [5].

$$\mathbf{K_S} \cdot \mathbf{d} = \mathbf{F} \tag{4.2}$$

First, from the principle of $m\ddot{x} + kx = F_{ext}$, with $m\ddot{x}$ the inertial force, Equation 4.2 is rewritten as:

$$\mathbf{K_S} \cdot \mathbf{d} = \mathbf{F_{AD}} - \mathbf{F_{inrt}} \tag{4.3}$$

Taking then the inverse of the global stiffness matrix:

$$\mathbf{d} = \mathbf{K_S}^{-1} \cdot \mathbf{F_{AD}} - \mathbf{K_S}^{-1} \cdot \mathbf{F_{inrt}} \tag{4.4}$$

Where the two terms on the right-hand side of the equation may be written as the deflection caused by the aerodynamic and inertial loads, respectively $\mathbf{d_{AD}}$ and $\mathbf{d_{inrt}}$. Then, after rearranging:

$$\mathbf{d_{AD}} = \mathbf{d} + \mathbf{d_{inrt}} \tag{4.5}$$

This final equation may be interpreted as the following: the deflection caused by the aerodynamic load equals the measured deflection plus the deflection following from the inertial load. The way this is used in the framework is by first calculating the inertial force from the acceleration, then calculating the resultant deflection under this load and finally adding this load to the measured deflections.

With this approach, the framework will look for the load which causes the aerodynamic deflection and thus the aerodynamic load. This allows for a continuous separation between the aerodynamic and inertial forces, where the latter are computed directly from empirical results. Hence, the three forces of Collar's triangle can still be distinguished and the error in the marker measurements is used once for the inertial loads.

4.3. Framework Algorithm

The flowchart which visualises the workflow of the framework is shown in Figure 4.4. The in- and output blocks are rounded to make clear that these are not operations. For each block in bold text, a specific section will be devoted to its elaboration. First, the block **[Optimisation Loop 1: Scaling]** will be covered in subsection 4.3.1. Second, **[Optimisation Loop 2: Tuning]** will be covered in subsection 4.3.2. It is noted that the section above on the inclusion of the inertial load separation describes the part prior to the start of the first optimisation loop. This loop takes as input the aerodynamic deflection for which the load is then found after the second loop. This approach allows for a transparent separation of aerodynamic and inertial loads for the fluid-structure interaction characterisation in terms of the aeroelastic triangle of forces.

4.3.1. Optimisation Loop 1: Scaling

The goal of the first optimisation loop is to scale an aerodynamic lift distribution such that the objective function given by Equation 4.6 is minimal. In this objective function, $\mathbf{d_{AD}}$ is the deflection of the wing as taken from the sum of the marker measurements and the inertial deflection component as shown in the flowchart. Furthermore, the variable $\mathbf{d_{opt,\,1}}$ is a function of the LLT coefficients $\mathbf{A_n}$, an LLT curve scaling factor β, the node locations along the span $\mathbf{n_z}$, the global stiffness matrix $\mathbf{K_S}$, the span of the wing b and the free-stream velocity V_∞. Each term will be further explained in this subsection in the context of the computational processes which are part of this block. The initial value for β in the optimiser is zero.

$$\min\left(\sum\left|\mathbf{d_{opt,\,1}} - \mathbf{d_{AD}}\right|\right) \tag{4.6}$$

$$\mathbf{d_{opt,\,1}} = f(\mathbf{A_n}, \beta, \mathbf{n_z}, \mathbf{K_S}, b, V_\infty), \text{ with } \beta \text{ the optimisation variable.} \tag{4.7}$$

Find forces from LLT curve

In this process, an initial approximation of the aerodynamic lift distribution is generated based on LLT, which was previously discussed in subsection 2.1.1. The reason why the LLT curve was opted for is because LLT allows for the generation of the circulation distribution along the span by taking into account the geometry of the wing. Since lift is generated by circulation, the two will follow the same distribution. The method as proposed in Anderson is used to compute the coefficients for the wing which will be used in the remainder of this report [1]. A total of fifteen coefficients is used in order to generate the shape function for the lift distribution. By modelling the wing as a symmetric wing with span $2b$, the even coefficients can be set to zero in the optimisation. The LLT coefficients are generated outside of the optimiser and are thus considered an input in Equation 4.7. The forces themselves are calculated by using the prescribed lift distribution at the locations of each span-wise FEM node given by $\mathbf{n_z}$.

Adjust amplitude of LLT force curve

In Equation 4.7, the scaling factor β is included as the optimisation variable. The optimiser multiplies the entire LLT curve as derived from the geometry with this scaling factor in order to find the most suitable amplitude which minimises the objective function for loop 1. For this calculation, the span, the wing's aspect ratio and the free-stream velocity are used. In reality, there may exist an error in the free-stream velocity or angle of attack which will adjust the actual amplitude of the lift distribution. Hence, this step of the framework will attempt to correct the prescribed lift distribution to more closely match the actual lift distribution while maintaining its overall shape.

An example scaled LLT curve is shown in Figure 4.5a, for which VLM was used to generate a reference load following the same flow conditions as Figure 4.2 which showed the bend-twist coupling; $V_\infty = 24\ m/s$ and $AOA = 7°$. A more detailed explanation of how the reference case is generated will be provided in section 5.1.

Find deflection

This final step takes the scaled aerodynamic lift distribution to compute the LLT-based aerodynamic deflection based on the FEM beam representation of the model. The actual aerodynamic deflection $\mathbf{d_{AD}}$ is then used in the objective function Equation 4.6 to obtain an objective value. When this value is found to be below the tolerance level and the smallest variation tolerance of the optimiser is met, too, the optimiser will quit. At this point, the optimiser will have varied the LLT curve scaling factor β until its optimal value is reached. This is the output of the first optimisation loop.

The deflection is calculated with the application of the global stiffness matrix $\mathbf{K_S}$. By using the global stiffness matrix as provided by the cross-sectional modeller which is elaborated upon in [11], it is possible

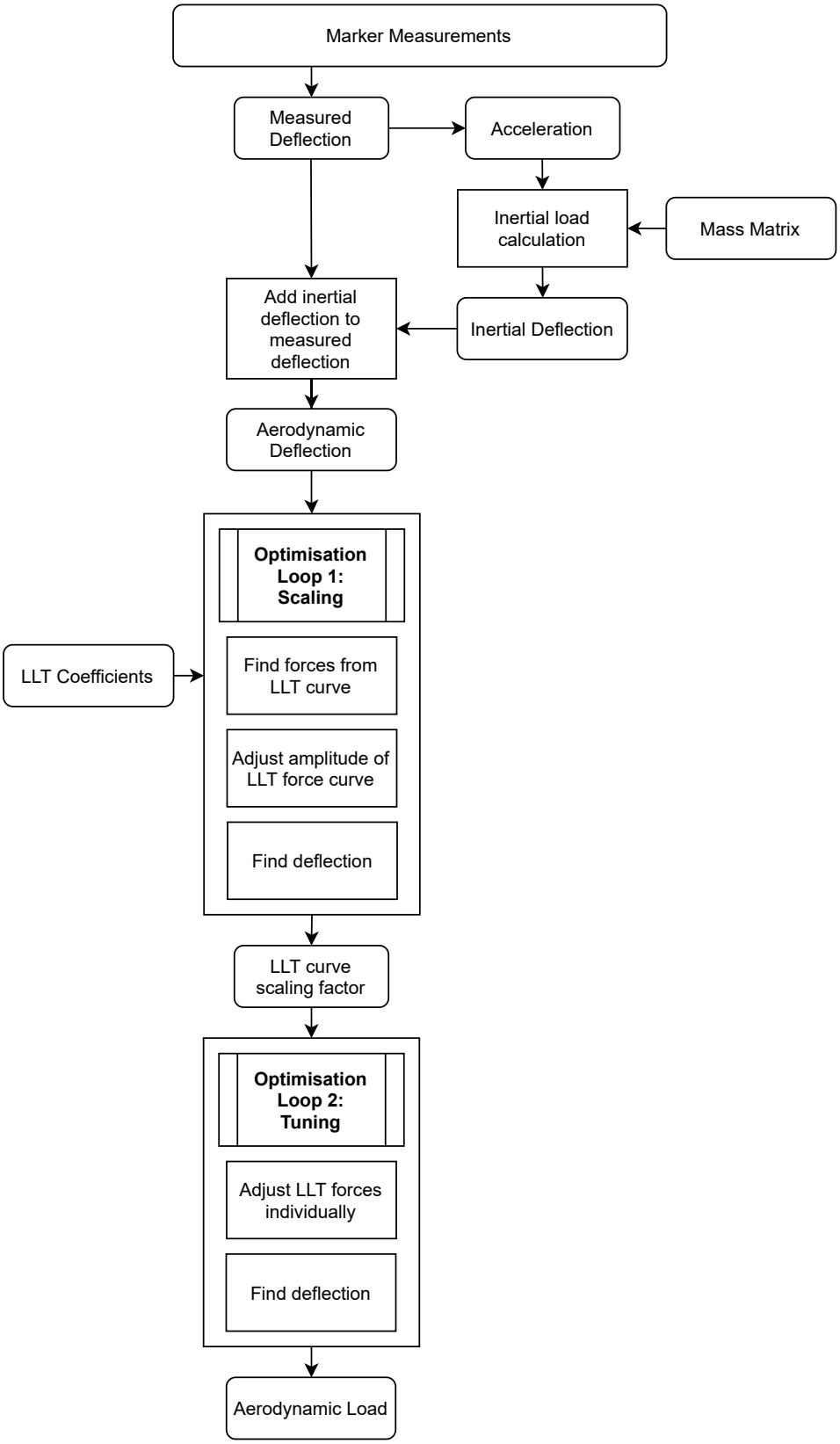

Figure 4.4: The flowchart of the framework used to extract the aerodynamic load given a set of marker measurements. The rounded boxes are in- or outputs of the square boxes, depicting an operation. Bold titles indicate a specific computational section.

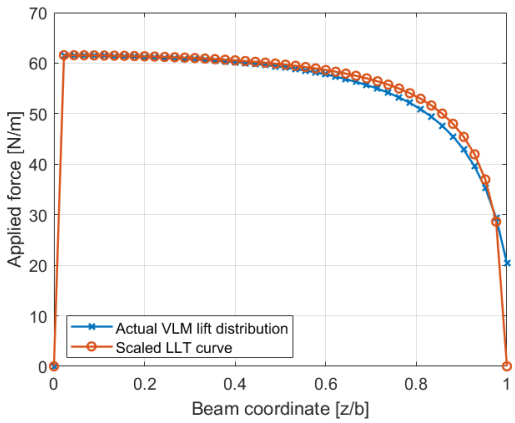

(a) Scaled LLT load distribution with respect to the reference VLM curve which was used to generate the deflections.

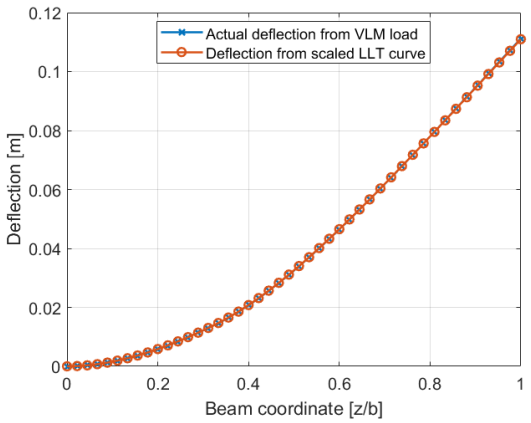

(b) Deflection from the scaled LLT curve compared to the deflection caused by the VLM reference load.

Figure 4.5: The optimised LLT curve load and resulting deflections as per the reference VLM case with $V_\infty = 24\ m/s$ and $AOA = 7°$, after the first optimisation loop which scaled the LLT curve.

to obtain the force **F** given a deflection **d** as per Equation 4.2. Its inverse relation can also be used to obtain the deflection, given a force. In this equation, it should be noted that the boundary conditions (BCs) must be taken into account. For this research, the wing is assumed to be a cantilever beam with the root as a fixed location with null rotation in either axis. Therefore the BCs are considered zero for each entry, implying that they can be taken out of the equation. Each plot including the forces in this report will show a null root force, for which this is the cause. Following this approach, the deflections for each loop can be extracted given the aerodynamic forces from a scaled LLT curve and the inverse relation of Equation 4.2. This is shown in Figure 4.5b for a static case.

4.3.2. Optimisation Loop 2: Tuning

In the second optimisation loop, the adjusted lift distribution is used as the initial optimisation vector to be considered as the variable for the second loop. Again, the objective function is given by Equation 4.8. It is essentially the same objective function, except that the results are weighted with the respective distance of the local nodes from the tip. This was achieved in MATLAB with the $flip$ command, as shown in the objective function. This weighting was found to improve the results, as the root nodes require the largest force to be imposed upon in order to obtain a certain deflection. The tip nodes are relatively easier to move as any force on the tip will greatly increase the moment at the root, which corresponds to large deflections at the tip. The optimisation deflection for the second loop $\mathbf{d_{opt,\,2}}$ is now a function of the force distribution and the global stiffness matrix. The initial estimate for this force, $\mathbf{x_0}$, is shown in Equation 4.10 and is a function of the LLT values with the optimised scaling factor β from the first optimisation loop.

$$\min\left(\sum\left[\left|\mathbf{d_{opt,\,2}} - \mathbf{d_{AD}}\right| \cdot flip(\mathbf{n_z})\right]\right) \tag{4.8}$$

$$\mathbf{d_{opt,\,2}} = f(\mathbf{F_{opt}}, \mathbf{K_S}), \text{ with } \mathbf{F_{opt}} \text{ the optimisation variable.} \tag{4.9}$$

$$\mathbf{x_0} = f(\mathbf{A_n}, \beta, \mathbf{n_z}, \mathbf{K_S}, b, V_\infty) \tag{4.10}$$

Moreover, the optimisation in this loop will optimise each force at each node individually. Hence, $\mathbf{F_{opt}}$ is the variable of this optimisation process. The initial value for $\mathbf{F_{opt}}$, or $\mathbf{x_0}$, is calculated with the same module which calculated the LLT forces from the adjusted curve in the first optimisation loop. To calculate this initial force distribution, the LLT curve scaling factor from the first loop is used. Following this initial estimate, the optimiser will attempt to improve the match in deflection by adjusting each force individually.

The output of the second loop is thus a force distribution which represents the load required to get to the aerodynamic deflection $\mathbf{d_{AD}}$. In other words, these loads may be considered as the applied loads and thus the aerodynamic load.

In conclusion, the framework can be considered in three overall components. Firstly the inertial forces are calculated separately from the optimisation processes, such that they can be identified as a separate known

force. Secondly, an LLT lift distribution shape is scaled to match the measured deflections plus the inertial deflection. This combination then represents the deflection caused by the aerodynamic load. The third and final component will then try to improve the results of the second curve by individually tuning the applied nodal forces. This approach allows the optimiser to start off with an appropriate guess of the applied load distribution through LLT such that it may adjust for local experimental imperfections and in dynamic cases also unsteady aerodynamic effects. With this knowledge, the framework will remain robust rather than instantly trying to over-fit towards the measured deflections as was shown to occur in an example without a prior estimate. In the following chapter, a sensitivity analysis shows the first results from the framework in two numerical test cases to assess the behaviour of its response.

5

Numerical Assessment

In order to assess the performance of the developed framework as discussed in chapter 4, a numerical assessment is executed. The goal of this effort is to provide insights into the characteristics of the framework, such as its robustness and accuracy. This will support the application of this framework on an experimental test model at a later stage with empirical data in terms of understanding the behaviour of the framework's response to experimental imperfections such as measurement errors.

To start off the assessment, two static reference cases are set up using the same test model as the one used in the experiments which was discussed in chapter 3. These static cases will be discussed in section 5.1. Then, a behavioural analysis is performed in terms of a series of parameters on the test model, framework and measurement method. This will be the topic of section 5.2 and it will lay out the fundamental understanding of the framework's output, considering artificial variations in input. These artificial variations can then be compared to the flaws in an experimental context to discuss the reasonableness of the empirical results. Finally, a brief discussion is held on the key take-away points of this chapter in section 5.3.

5.1. Test Cases

The reference test cases are set up to represent a realistic scenario with respect to the experimental model that will be used in chapter 6 for final validation. With the framework relying on the deflection to optimise the forces, the forces which in first instance generate the deflection for the reference cases must be realistic in terms of the aerodynamic load distribution of the wing. Moreover, the reference cases must represent a broad range of situations which may occur for the wing with varying loads and resulting deflections. With these reference cases, it will be possible to assess the influence of adjustments made to either the framework or the input parameters as will be the topic of section 5.2, where the behavioural sensitivity analysis is performed.

For the purpose of this assessment, two test cases are set up with varying conditions to identify whether the considerations made during the sensitivity analysis are random or consistent in their influences on the output. Furthermore, more insights are obtained when considering a wider range of applications as the developed framework is novel. The test cases (TCs) vary both in angle of attack of the wing and the free-stream velocity. For these cases, the aerodynamic lift is calculated with VLM and is referred to as the actual force ($\mathbf{F_{act}}$). The actual deflection $\mathbf{d_{act}}$ for each case is extracted from this with the method as described in subsection 4.3.1. Then, the framework is applied to extract the forces from the calculated deflections. These extracted forces are referred to as the optimised forces or $\mathbf{F_{opt}}$. Next, the optimised forces are imposed on the numerical wing model to obtain the optimised deflections $\mathbf{d_{opt}}$ which serve solely as an indication of how well the optimisation managed to meet the actual deflection. As a measure of how well the displacement matches, the mean relative difference (MRD) of the optimised and actual deflections will be used according to Equation 5.1. Finally, the quality of the individual test cases is measured by the mean relative difference of the optimised and actual forces, given by Equation 5.2. Both of these values are always expressed in percentages whenever used throughout this report.

$$MRD_d = mean\left(\left|1 - \frac{\mathbf{d_{opt}}}{\mathbf{d_{act}}}\right| \cdot 100\%\right) \tag{5.1}$$

Table 5.1: Summary of the generic test cases that will be used in the sensitivity analysis.

Test Case	AOA [°]	V_∞ $[m/s]$
TC1	5	14
TC2	7	24

Table 5.2: Mean Relative Differences of the deflection and applied forces for the two reference cases.

Test Case	Loop	MRD_d	MRD_F
1	1	0.2353	1.7114
	2	0.1855	1.6350
2	1	0.2375	1.7153
	2	0.1839	1.6308

$$MRD_F = mean\left(\left|1 - \frac{\mathbf{F_{opt}}}{\mathbf{F_{act}}}\right| \cdot 100\%\right) \tag{5.2}$$

The two reference cases will each be analysed with the framework and the output will be provided in a total of four figures: the deflection, the applied forces, and the ratio of both between the optimised and actual values; including the results after the first optimisation where the LLT curve is scaled and after the second optimisation which tunes the forces individually. The first test case is labelled as Test Case #1 and has an angle of attack $AOA = 5°$ with a free-stream velocity of 14 m/s. The second case, respectively Test Case #2 has 7° and 24 m/s. In both cases, the flow is steady so no inertial forces need to be considered in this analysis as they may be assumed to be negligible. It is noted that the inertial forces do not need to be considered here since they have no influence on the optimisation loops. A brief summary of the two test cases is shown in Table 5.1.

Test Case #1: $AOA = 5°$ & $V_\infty = 14$ m/s
The lift load for this case follows from VLM with the input data as per Table 5.1. These forces are then combined with the global stiffness matrix in Equation 4.2 to extract the deflection of the wing under the lift load. The lift and wing deflection for Test Case #1 is shown in Figure 5.1. Running the framework on this deflection data set then gives the four figures which are shown in Figure 5.2. These graphs will serve as the first reference for the sensitivity analysis. The results in terms of the MRD can be found in Table 5.2, assisting in the quantitative comparison of results. Opt 1 implies the result of the first optimisation loop and opt 2 the second in the figures.

Both of the MRD values are improved slightly by tuning the forces in the second loop. While barely visible in the deflection in Figure 5.2a, the deflection ratios show that the deflection near the root is closer to the actual values, whereas the tip deflection tends to be smaller. This can be seen in Figure 5.2c, where it is also noticeable how the root deflection is corrected more than the tip deflection deviates further. While the differences are in the order of .5% at most, the forces at the tip which are noticed to deviate more towards the tip as per Figure 5.11b have a larger effect on the overall deflection. Thus, the mean relative deflection has an overall improvement in absolute terms from 0.2353% to 0.1855%. As for the forces, the deviation is smaller and less visible in both the applied force and the relative applied force, as shown in Figure 5.2b and 5.2d. Also, Figure 5.2b shows a deviation in the forces near the tip. This is likely to be caused by the fact that the VLM code used accounts for a tip force generated in the last half element, as the continuous force is mapped to the nearby discrete points. The structural solver, on the other hand, uses discrete forces following the LLT curve locally which has a zero lift force at the tip. Additionally, one may notice that in Figure 5.2d the final node (located at $z/b = 1$ or $z = 1.75$ m) is not shown. The reason for this is that following from how the optimiser applies LLT, the tip force will always be zero and thus the local ratio will always be zero, too. This would generate an undesirable effect on the plot itself, because the plot would have to display a wider range of values, reducing the legibility of the curves further. It is therefore noted that the ratio will always be zero for every applied force ratio at the tip node in the remainder of this document and not plotted in the respective plots to improve legibility of the figures.

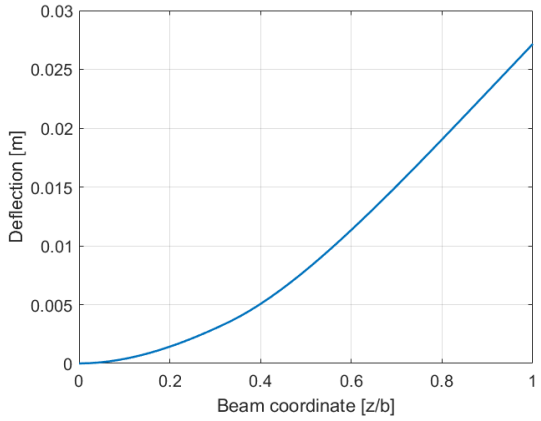

(a) Deflection plot of the wing under the VLM-predicted force.

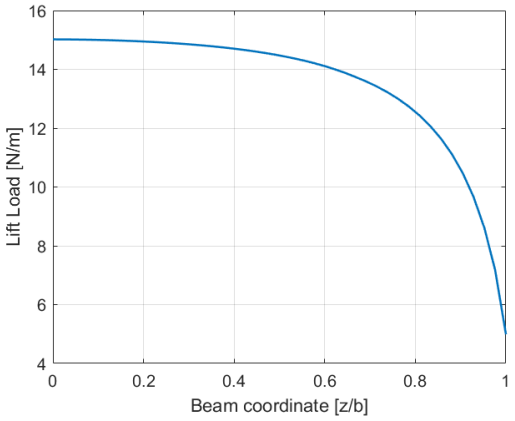

(b) Aerodynamic load plot with VLM prediction.

Figure 5.1: Wing deflection $[m]$ and VLM lift force $[N]$ for the first reference case with an angle of attack of 5° and a constant wind speed of 14 m/s on the FEM wing model. The tip displacement is 27.16 mm.

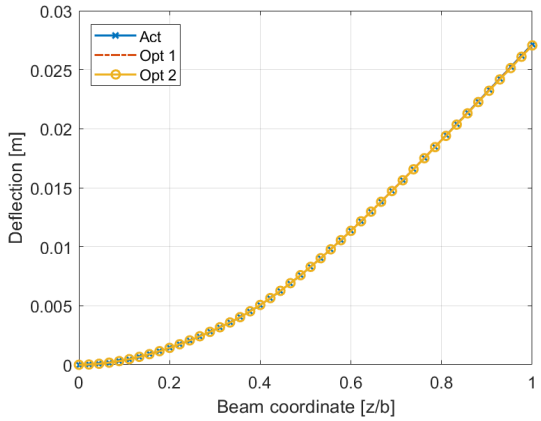

(a) Deflections after the first and second optimisation loops.

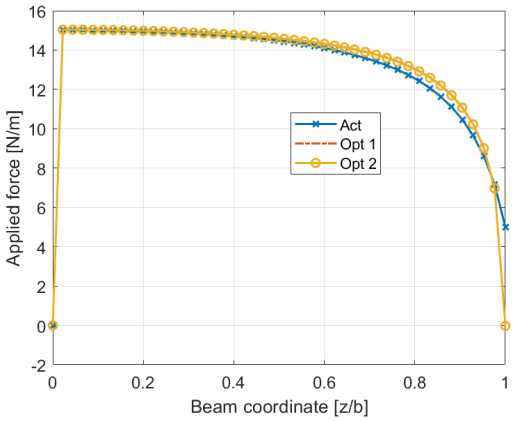

(b) Applied forces after the first and second optimisation loops.

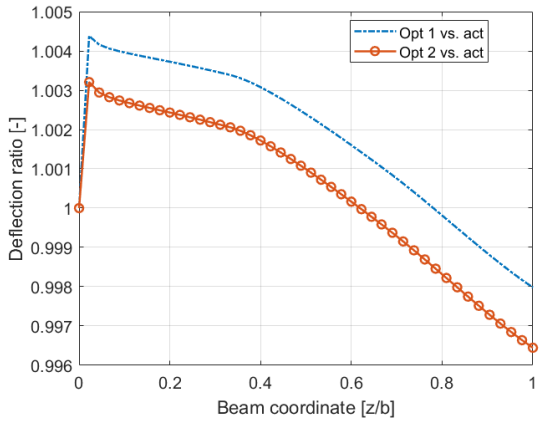

(c) Ratio of deflections of the optimised and actual values after the first and second optimisation loops.

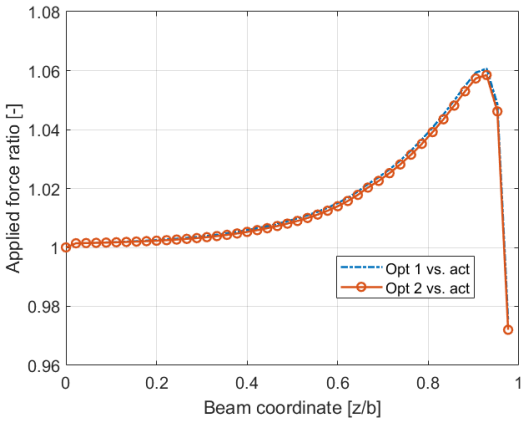

(d) Ratio of applied forces of the optimised and actual values after the first and second optimisation loops.

Figure 5.2: The reference graphs of the wing in Test Case #1.

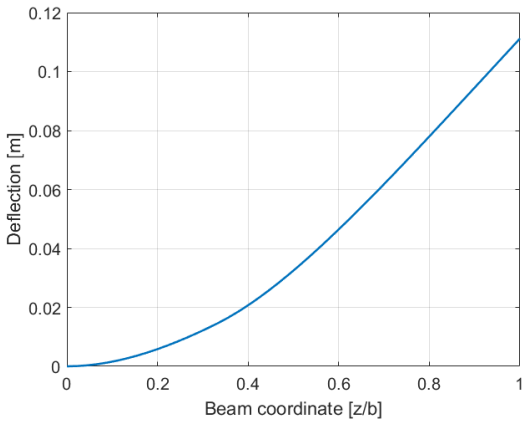

(a) Deflection plot of the wing under the VLM-predicted force.

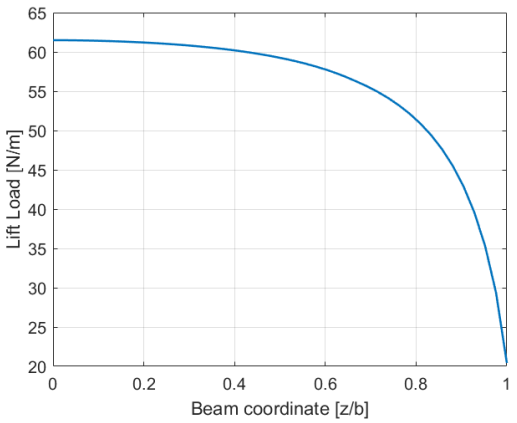

(b) Aerodynamic load plot with VLM prediction.

Figure 5.3: Wing deflection $[m]$ and VLM lift force $[N]$ for the second reference case with an angle of attack of 7° and a constant wind speed of 24 m/s on the FEM wing model. The tip displacement is 111.20 mm.

Test Case #2: $AOA = 7^\circ$ & $V_\infty = 24\ m/s$

In a similar sense as TC1, the second test case is set up. Using VLM, the lift load is combined with the global stiffness matrix to extract the actual deflection for TC2. The framework is then used to optimise a load vector in order to meet the actual deflection. Figure 5.4 contains the four figures on the deflection, applied forces and the respective ratios of the optimised and actual values. The MRD of the second case can be found in Table 5.2.

TC2 shows a similar behaviour as TC1, which can be noticed in the ratio of deflection plot in Figure 5.12a. Since more nodes shift downwards towards the unity line than move under it, MRD_d still improves from 0.2375% to 0.1839% after the second loop. On the other hand, the applied force now has a reduction from 1.7153% down to 1.6308%. Again, the forces near the root match closer than those at the tip, mainly caused by the fact that VLM does not go to a zero tip force because it is projecting the final half-element's force to the tip node while the prescribed LLT curve is zero at the tip. Finally, as can be seen in the absolute deflection and applied force graphs for TC1 and TC2, not much can be derived as the differences between the plots are minimal and the graphs do not have sufficient detail to emphasise the difference. Hence, for the sensitivity analysis, solely the ratio plots and the MRD values will be considered such that relative differences can be considered. Again, the plot for the local ratios of the applied force excludes the final $z/b = 1$ node from the graph.

5.2. Sensitivity Analysis

The two test cases from the previous section show how the framework manages to recover aerodynamic loads from the deflection of a wing in a static case within acceptable margins. Thus far, exact values were used as provided by Equation 4.2, where the output is more accurate than can be realistically extracted from an experiment. To simulate realistic data, adjustments must be made to introduce artificial errors into the data set. Such errors could exist due to flaws in the numerical model with respect to an experimental equivalent or errors in the measurements due to for example noise. Hence, the next step is to assess how the framework reacts to experimental situations, where for example the bending stiffness may be known with an accuracy of up to a certain percentage or where the deflection is measured with a certain accuracy, too. In order to look deeper into these experimental flaws, the sensitivity analysis will look at the various parameters which may affect the measured deflections or the numerical model. The goal of the sensitivity analysis in this document is to assess the behaviour of the response under such imperfections. With this knowledge, one may make recommendations towards the method of application of the proposed framework in experiments.

Following a logical order, the sensitivity analysis will be performed in subsection 5.2.1. At first, each parameter will be assessed individually and in the end the parameters will be adjusted altogether to represent an experimental set-up in. This set-up will be the topic of subsection 5.2.2, providing an insight in how the framework behaves in a simulated experimental environment. This will then be the proof-of-concept for the proposed framework. Later in chapter 6, actual experimental data will be used to validate the framework.

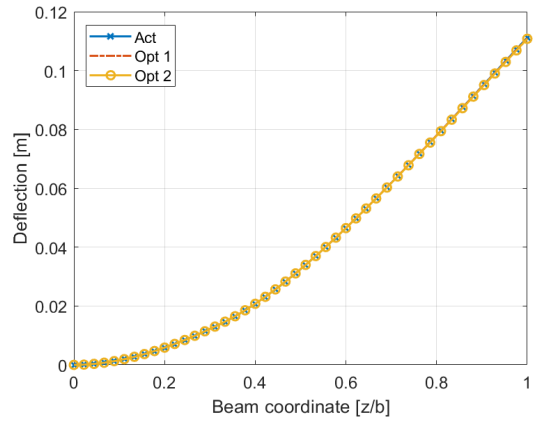

(a) Deflections after the first and second optimisation loops.

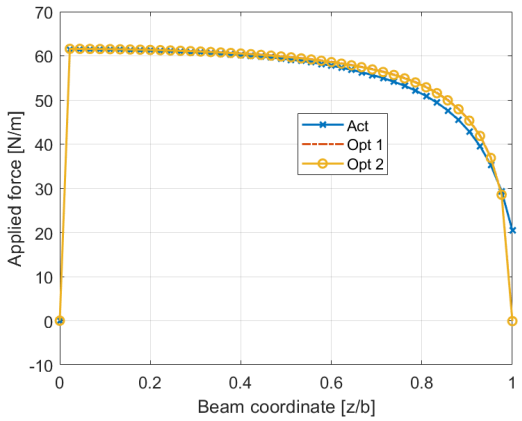

(b) Applied forces after the first and second optimisation loops.

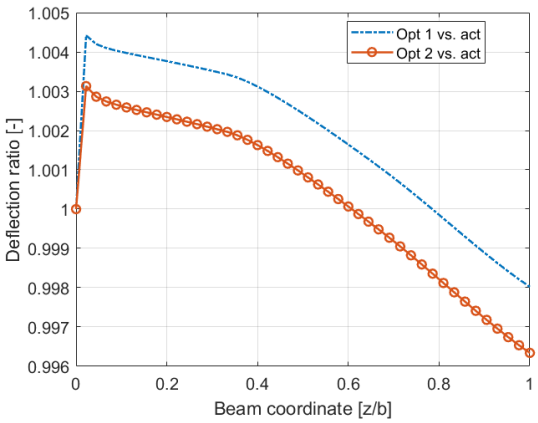

(c) Ratio of deflections of the optimised and actual values after the first and second optimisation loops.

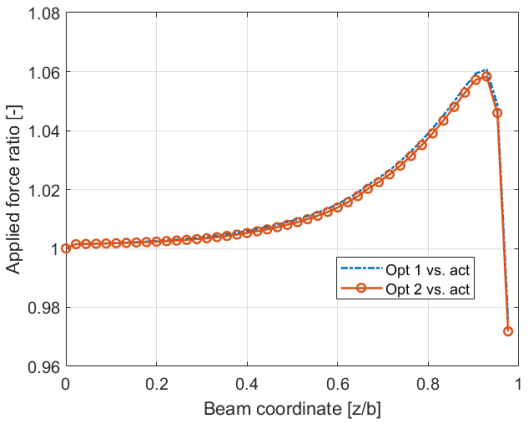

(d) Ratio of applied forces of the optimised and actual values after the first and second optimisation loops.

Figure 5.4: The reference graphs of the wing in Test Case #2.

5.2.1. Parameter Discussion

The parameters which will be analysed for their effect on the response are listed below along with the reason of interest in the respective parameter. Furthermore, an initial margin in which these parameters will be analysed is provided. Following the list, each parameter will be evaluated. It should be pointed out that some of these analyses are performed with randomised input. To obtain consistent results, the rng-counter in MATLAB is reset to 1 for each case such that the same random sequences can be obtained time after time. This implies that the results obtained here may vary when using other counter inputs or random generators. This is another reason for having two TCs as this should show the potential differences in randomness. Moreover, each case which includes randomised input is looped 50 times to introduce unique random noise in each individual case and the results are discussed in terms of the mean of the output as well as the standard deviation (SD) denoted as σ in the graphs. For both TCs, the MATLAB rng function is set to a particular value such that the same random variation is imposed on both TCs in each analysis.

In order to discuss the results, they are expressed in terms of the comparison between the sensitivity analysis (SA) case, which has the individual parameters adjusted, and the reference test case as per section 5.1. To best visualise the effects, the mean relative differences will be discussed in addition to the ratio plots as discussed before. The following parameters will be implemented in the framework such that the input data can be altered in order to simulate the respective experimental imperfection:

- **Rounding**: As mentioned before, Equation 4.2 provides exact values for the deflection following from the lift and global stiffness matrix. In reality, measurement methods have limited significant digits, implying that in order to use the values from numerical computations they first ought to be rounded in order to represent empirical data. For the measurement method used in the validation experiment, marker-tracking, values in the order of 0.001 m can be reliably measured. Thus, all deflections will in first instance be rounded to the third digit behind the decimal point.

- **Random errors**: If only rounding would be introduced, it would be assumed that the measurements made by the markers are perfect and reflect the actual deflections rounded to 0.001 m. Due to the set-up of the experiment, however, it can be shown that the marker measurements have an accuracy in the order of 0.001 m. This random error will be introduced as a parameter in the sensitivity analysis to see how the framework copes with errors in the deflection. The error introduced by (a lack of) measurement accuracy varies from rounding as the measurement accuracy itself implies only a fixed amount of significant digits may be used, beyond which rounding must be applied. The error introduced by rounding prior to a random error from the actual measurement may thus vary.

- **Number of node measurements**: Following from the previous logic regarding the flaws of measurement methods, it is not uncommon for a measurement to either be unreliable or absent. For example, with marker-tracking, it occurs that the track of one particular marker is absent for a set of measurements. Additionally, outliers may be found when the marker data is processed. Such outliers need to be removed from the analysis which also counts as a lacking node. To model this behaviour, an independent set of nodes will be removed from the deflections in the sensitivity analysis. Typically, up to 10% of the nodes may be lacking measurements and as such this value will be considered in this analysis.

- **Error in the stiffness matrix**: Next to the experimental flaws in the acquisition or the set-up, numerical errors can also exist. In this iFEM method, the global stiffness matrix thus far was assumed to be perfect. For most experimental models, there is a difference of up to 1% in the stiffness properties with respect to their respective numerical models. Due to the relation between the deflection and the force caused by the stiffness matrix, this error will be assessed in the sensitivity analysis. To further emphasise the effect of this error, in the SA a value of 5% will be used.

Rounding

It is expected that by rounding the deflection, the optimiser has more room to converge prior to reaching the actual deflection. The tolerance of the optimiser plays a key role in this consideration and was discussed previously to have a direct influence on the quality of the result due to the relation between force and deflection as given by Equation 4.2. Both TC1 and TC2 had an initial rounding introduced which reflected the experimental situation: rounded up to 0.001 m. The comparison of the results of the reference case and the SA case with rounding for TC1 is shown in Figure 5.5 and for TC2 in Figure 5.6. A compilation of the MRD variation for this case is shown in Table 5.3 and 5.4, respectively. The MRD tables show the reference values of the test cases next to the values of the respective SA cases. Finally, the difference between the MRD values for each

Table 5.3: Summary of MRD values for TC1 and the sensitivity analysis case with rounding to the third digit.

TC1	Reference		SA: Rounding 3		Difference [%]	
	MRD_d	MRD_F	MRD_d	MRD_F	MRD_d	MRD_F
Loop 1	0.2353	1.7114	0.5299	1.3723	125.20	-19.81
Loop 2	0.1855	1.6350	0.2628	1.4850	41.67	-9.17

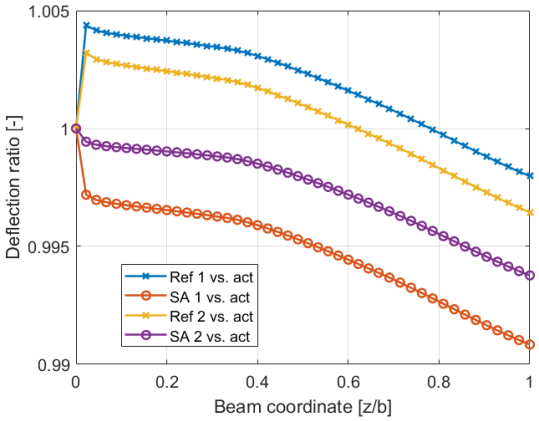

(a) Ratio of deflections of the optimised and actual values after the first and second optimisation loops.

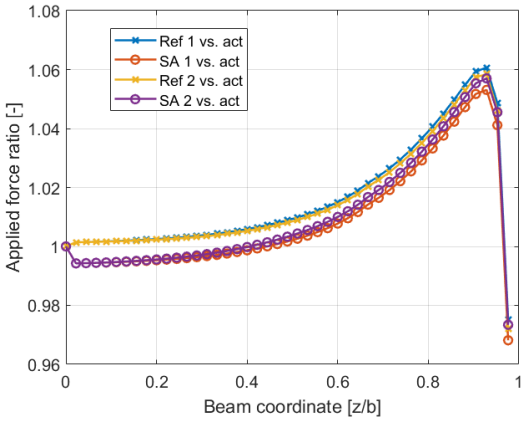

(b) Ratio of applied forces of the optimised and actual values after the first and second optimisation loops.

Figure 5.5: Results of TC1 with rounding to the third digit behind the decimal point for the sensitivity analysis case compared to the reference case with no rounding.

loop is provided both in deflection and force MRDs to give a clear view of how the SA parameter affects the result for both values. This difference is calculated with Equation 5.3 and is shown in percentages.

$$MRD_{diff} = \left(\frac{MRD_{SA}}{MRD_{ref}} - 1 \right) \tag{5.3}$$

It can be seen in Table 5.3 and 5.4 that rounding the deflection to the third digit seems to improve the results for all MRD values in TC2, whereas only MRD_F improves for TC1. From this varying result, one can conclude that rounding may have an arbitrary effect as it can either assist the optimiser in finding the right value, or make the optimiser find a wrong value. MRD_d varies more for both cases than MRD_F, as the non-exact values are fed into the optimiser. Hence, the framework attempts to solve for a beam which is non-exact in its deflection. Due to the relation between force and deflection (see Equation 4.2), this plays a key role in the outcome.

The value of MRD_F for TC1 and TC2 after the second loop, however, varies with a factor of roughly 2. This can be explained by the fact that due to a larger overall deflection in TC2 caused by higher forces, the rounded values are relatively lower than when the deflection is smaller. Hence, with higher values of deflection, rounding is expected to have fewer influence on the outcome.

Subsequently, considering Figure 5.5b and 5.6b which display the ratio of applied forces for TC1 and TC2, the latter shows that the ratio improves near the tip region. A ratio closer to unity implies that the optimised value is closer to the reference value. Following the same logic, suppose a more flexible wing would be used under the same load, then the error caused by rounding will also reduce. It can thus be concluded that there is a random relation between the error from rounding and the flexibility of the model under a certain load case.

Table 5.4: Summary of MRD values for TC2 and the sensitivity analysis case with rounding to the third digit.

TC2	Reference		SA: Rounding 3		Difference [%]	
	MRD_d	MRD_F	MRD_d	MRD_F	MRD_d	MRD_F
Loop 1	0.2375	1.7153	0.1757	1.5701	-26.02	-8.46
Loop 2	0.1839	1.6308	0.1737	1.5640	-5.55	-4.10

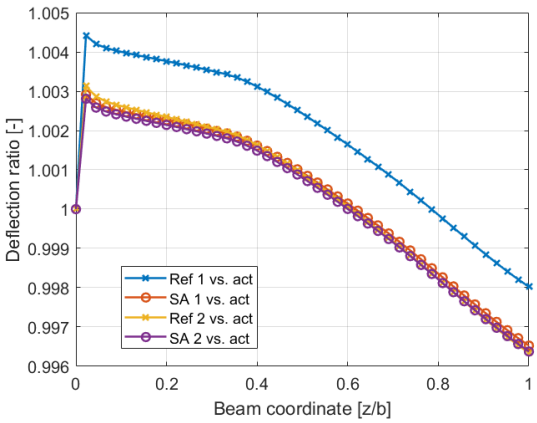

(a) Ratio of deflections of the optimised and actual values after the first and second optimisation loops.

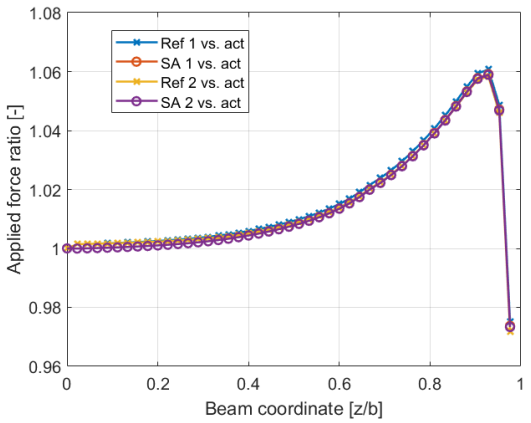

(b) Ratio of applied forces of the optimised and actual values after the first and second optimisation loops.

Figure 5.6: Results of TC2 with rounding to the third digit behind the decimal point for the sensitivity analysis case compared to the reference case with no rounding.

Table 5.5: Summary of MRD values for TC1 and the sensitivity analysis case with a random error of 0.001 m. The mean and standard deviation values are shown for 50 random error vectors and the difference applies to the mean of the MRD values.

TC1	Reference		SA: Random error ±0.001 m				Difference of mean MRD [%]	
			Mean		SD			
	MRD_d	MRD_F	MRD_d	MRD_F	MRD_d	MRD_F	MRD_d	MRD_F
Loop 1	0.2353	1.7114	0.2893	1.7928	0.1666	1.8012	22.95	4.76
Loop 2	0.1855	1.6350	0.0565	1.8680	0.0278	2.3412	-69.54	14.25

Random Errors

In a similar manner to rounding the reference deflection, a random value between -0.001 m and 0.001 m is added to each entry of the reference deflection set prior to running the framework. It is pointed out that no rounding is performed on this reference set. This allows the study of the behaviour of the framework when measurement uncertainties are included as noise. The equation used to simulate noise is shown in Equation 5.4, with $a = -0.001$ m, $b = 0.001$ m and r a random scalar generated using the MATLAB function $rand$ on the default interval $[0,1]$ from a uniform distribution. The resulting ratio graphs are shown in Figure 5.7 and 5.8 for Test Case #1 and #2, respectively. Similarly, Table 5.5 and 5.6 show the values of the MRD. As the random error case was run over 50 loops to assess the statistic effect, the tables now also show the MRD values for the SA case in terms of a mean and SD value. The figures themselves include a $\pm 3\sigma$ curve to depict the variation of the results. Additionally, the figures for the ratios are now split into one figure per loop to allow for a clear overview of the variation of the results.

$$d_{SA,\,noise} = d_{ref} + [(b-a)\cdot r + a] \tag{5.4}$$

By looking at the MRD values from Table 5.5 for the random error in TC1, one may notice that the MRD displacement is increased by up to 22.95% for TC1, where deflections are smallest. After the second loop, however, MRD_d has improved over the reference case. The MRD for the applied force increases by about 14% after the second loop with respect to the reference case. Looking at Table 5.6, showing the values for

Table 5.6: Summary of MRD values for TC2 and the sensitivity analysis case with a random error of 0.001 m. The mean and standard deviation values are shown for 50 random error vectors and the difference applies to the mean of the MRD values.

TC2	Reference		SA: Random error ±0.001 m				Difference of mean MRD [%]	
			Mean		SD			
	MRD_d	MRD_F	MRD_d	MRD_F	MRD_d	MRD_F	MRD_d	MRD_F
Loop 1	0.2375	1.7153	0.2662	1.7607	0.1536	1.8012	12.08	2.65
Loop 2	0.1839	1.6308	0.1773	1.6788	0.1103	2.0502	-3.59	2.94

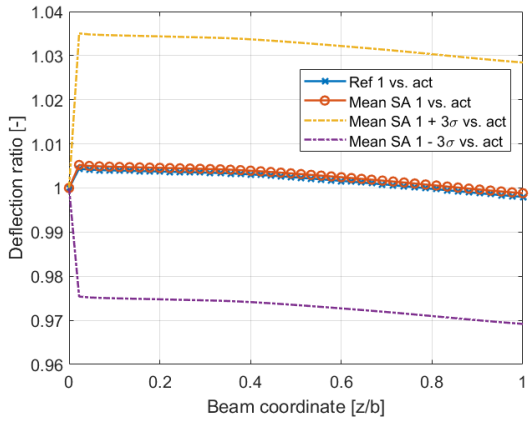

(a) Ratio of deflections of the optimised and actual values after the first optimisation loop.

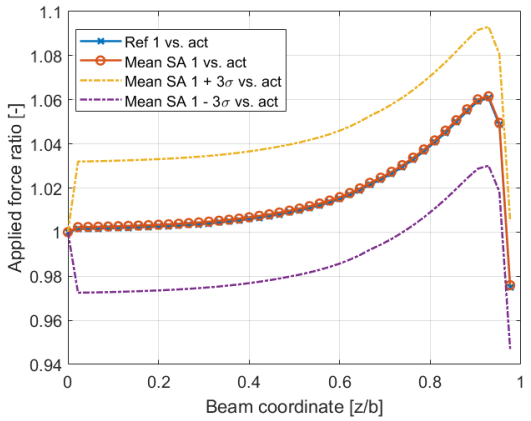

(b) Ratio of applied forces of the optimised and actual values after the first optimisation loop.

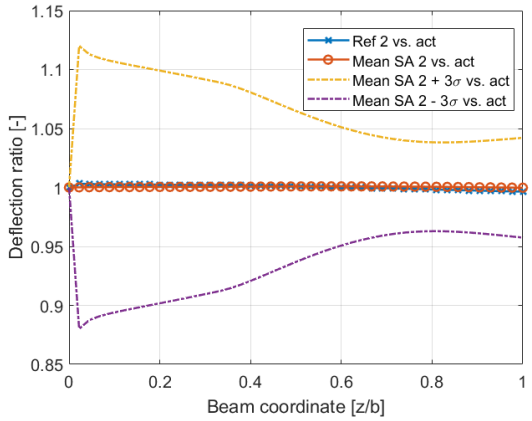

(c) Ratio of deflections of the optimised and actual values after the second optimisation loop.

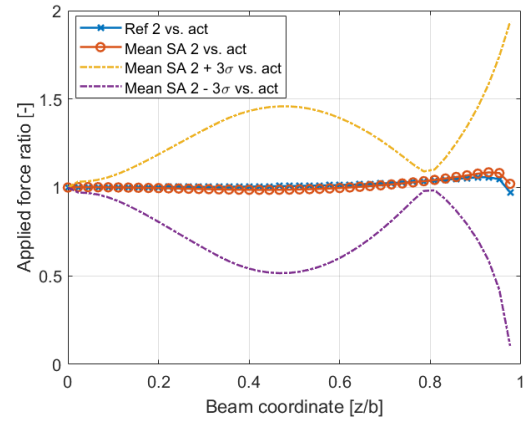

(d) Ratio of applied forces of the optimised and actual values after the second optimisation loop.

Figure 5.7: Results of TC1 with a random error of 0.001 m for the sensitivity analysis case compared to the reference case with no random error. The statistical mean over 50 loops with random errors is shown along with the $\pm 3\sigma$ curves.

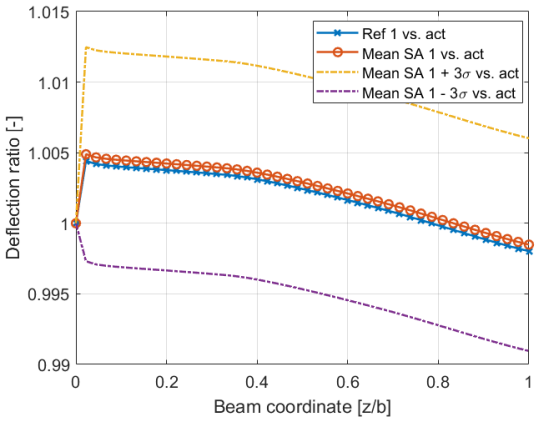

(a) Ratio of deflections of the optimised and actual values after the first optimisation loop.

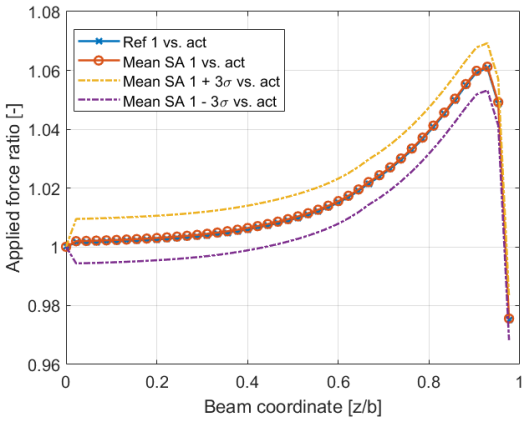

(b) Ratio of applied forces of the optimised and actual values after the first optimisation loop.

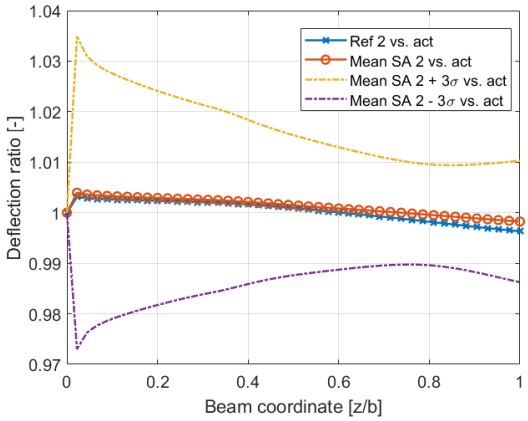

(c) Ratio of deflections of the optimised and actual values after the second optimisation loop.

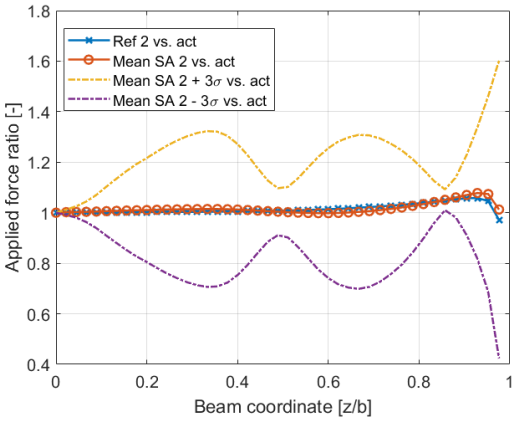

(d) Ratio of applied forces of the optimised and actual values after the second optimisation loop.

Figure 5.8: Results of TC2 with a random error of 0.001 m for the sensitivity analysis case compared to the reference case with no random error. The statistical mean over 50 loops with random errors is shown along with the $\pm 3\sigma$ curves.

TC2, one can conclude that again when overall deflections are larger, the framework becomes less sensitive to random deflection errors. As the deflections increase, the force becomes less sensitive to small random errors. This behaviour was also shown in the analysis of rounding the deflection.

The ratio plots for the displacements show that the wing has a mean deflection which is roughly equal to the reference case when compared to the SA case with a random error, as shown in Figure 5.7a and 5.7c by the mean curve. Looking then at Figure 5.7b and 5.7d, the mean force curve also seems to converge towards the reference case without random errors. This can be explained by the fact that the mean of the error averages out for the deflection and the force. The large fluctuations in standard deviation curves show that the optimisation in the second loop will attempt to over-fit to local errors in deflection. This is shown in the ratio of applied force plots, too. The inflection point that is found in both TC1 and TC2, at around $z/b = 0.85$ in Figure 5.7b and 5.7d, is located where the lift load has a steep drop due to the tip losses. This could lead the second optimiser to a wrong solution, especially in the presence of random errors in the measurements. Looking at TC2, with Figure 5.8a and 5.8c, the deflection shows similar behaviour. However, now the overall variation is smaller because the deflections are higher also in terms of the SD values. The ratios for the applied force in Figure 5.8b and 5.8d show that the force is consistently over-adjusted in loop 2 in the mid-span region, which is then also corrected for in the tip region. This behaviour was also noticed in TC1. Again, the mean matches the reference case quite well, which corresponds to the values from the MRD tables.

The figures plotted after the first loop for the deflection and the force, Figure 5.7a and 5.7b, show that the variation given by the SD curves is constant across the span. This can be explained by the fact that the optimiser is limited in its variation to scaling the entire curve. This implies that any variation in the deflection or force will be reflected at all points of the span since the LLT curve is scaled as a whole. This behaviour is expected in all random cases, as it is caused by the random variation of the input.

Overall, it can be said that with an error of up to 1 mm, the framework continues to provide reliable information about the force distribution, with larger deviations near the tip. These deviations become smaller when the maximal tip deflection increases. The random error – much like the rounding – shows that the framework will be influenced randomly and no systematic behaviour can be derived. Essentially, the error should be kept as small as possible relative to the absolute deflections to improve performance. Moreover, the optimisation in the second loop attempts to over-fit to local erroneous nodes, resulting in large deviations from the actual value. This effect is emphasised when there is a lack of multiple measurements. The mean, however, tends towards the reference case at all times and as such it is recommended to make multiple measurements to allow for any form of statistical averaging. Lastly, it can be seen by the deviation of the SD curves that for singular measurements, a large volatility can be expected in the results.

Number of Node Measurements

To assess the response of the framework to a local lack of measurement, the optimiser is adjusted to simply ignore the value at that measurement. It is thus taken out of the input and from the output of the objective function. This way, the optimiser will function as normal with the exception that certain nodes are not considered. The benefit of not taking the node out as a whole, is that the forces on the nodes next to it will not have to compensate for the lack of the node. In available data sets, the marker-measurement system showed that up to 10% can be faulty and need to be taken out of the data set. Hence, to study the worst-case scenario, up to 10% of the nodal measurements will be ignored to study the effect of lacking local data. These nodes are picked randomly using the $randi$ MATLAB function. As the FEM model has 44 nodes next to the root, which is fixed, up to four nodes will be excluded in the sensitivity analysis. Finally, the MRD values are summarised for TC1 and TC2 in Table 5.7 and 5.8. The graphs for the ratios of deflection and applied force are provided in Figure 5.9 and 5.10. Values are shown as statistics taken from a total of 50 randomly picked sets of nodes.

Table 5.7: Summary of MRD values for TC1 and the sensitivity analysis case with up to 10% lacking measurements. The mean and standard deviation values are shown for 50 random selections of lacking nodes and the difference applies to the mean of the MRD values.

TC1	Reference		SA: 10% Lacking nodes				Difference of mean MRD [%]	
			Mean		SD			
	MRD_d	MRD_F	MRD_d	MRD_F	MRD_d	MRD_F	MRD_d	MRD_F
Loop 1	0.2353	1.7114	0.2365	1.7135	0.1326	1.8012	0.51	0.12
Loop 2	0.1855	1.6350	0.1857	1.6364	0.0957	1.7447	0.11	0.09

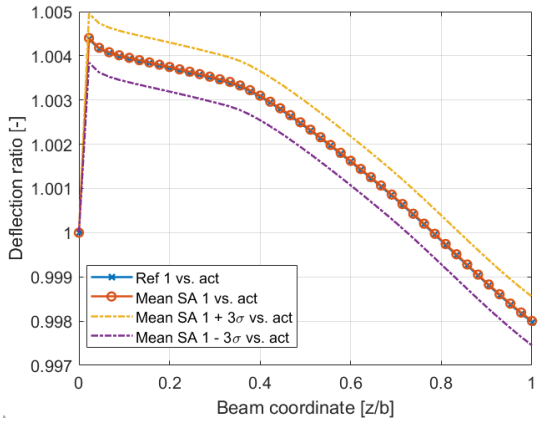

(a) Ratio of deflections of the optimised and actual values after the first optimisation loop.

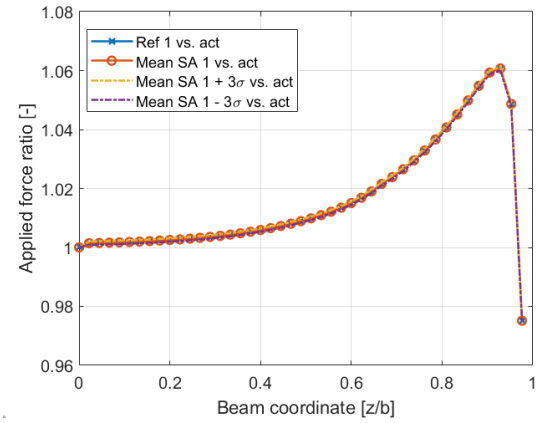

(b) Ratio of applied forces of the optimised and actual values after the first optimisation loop.

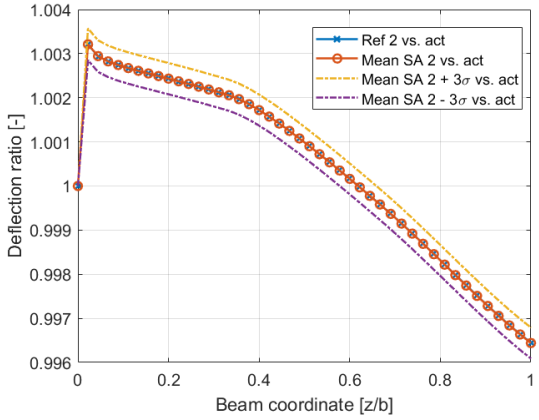

(c) Ratio of deflections of the optimised and actual values after the second optimisation loop.

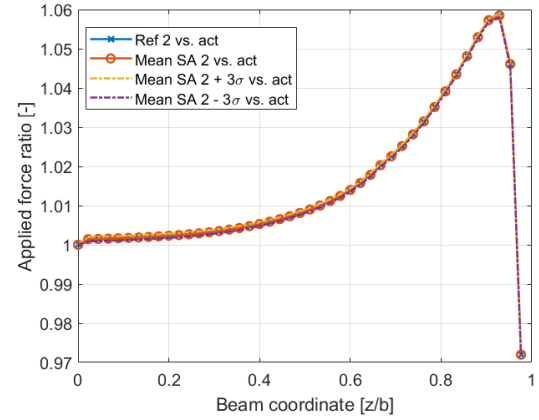

(d) Ratio of applied forces of the optimised and actual values after the second optimisation loop.

Figure 5.9: Results of TC1 with four lacking measurements (about 10% of total measurements) for the sensitivity analysis case compared to the reference case with no lacking measurements. The statistical mean over 50 loops with random errors is shown along with the $\pm 3\sigma$ curves.

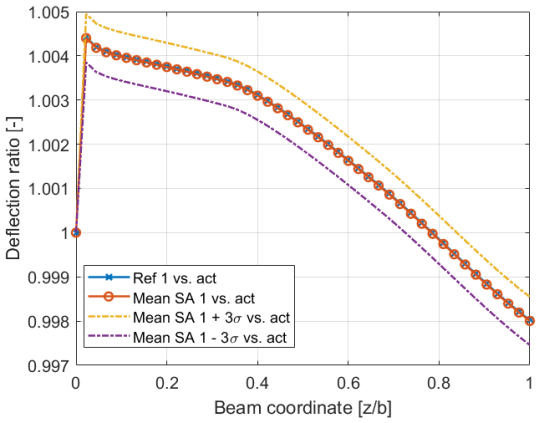

(a) Ratio of deflections of the optimised and actual values after the first optimisation loop.

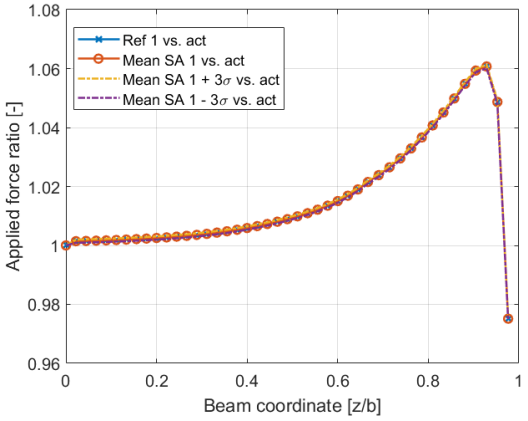

(b) Ratio of applied forces of the optimised and actual values after the first optimisation loop.

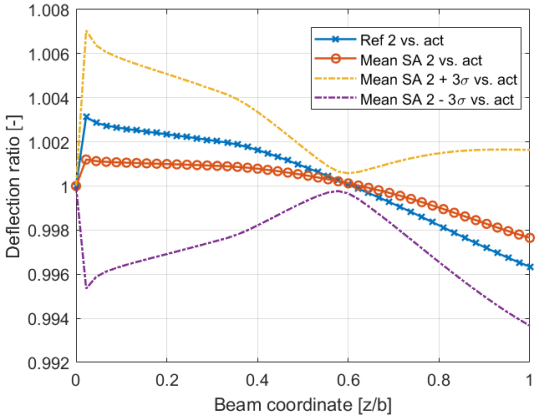

(c) Ratio of deflections of the optimised and actual values after the second optimisation loop.

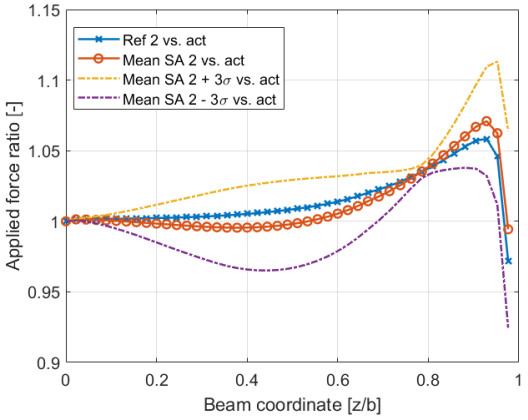

(d) Ratio of applied forces of the optimised and actual values after the second optimisation loop.

Figure 5.10: Results of TC2 with four lacking measurements (about 10% of total measurements) for the sensitivity analysis case compared to the reference case with no lacking measurements. The statistical mean over 50 loops with random errors is shown along with the $\pm 3\sigma$ curves.

Table 5.8: Summary of MRD values for TC2 and the sensitivity analysis case with up to 10% lacking measurements. The mean and standard deviation values are shown for 50 random selections of lacking nodes and the difference applies to the mean of the MRD values.

TC2	Reference		SA: 10% Lacking nodes				Difference of mean MRD [%]	
			Mean		SD			
	MRD_d	MRD_F	MRD_d	MRD_F	MRD_d	MRD_F	MRD_d	MRD_F
Loop 1	0.2375	1.7153	0.2365	1.7135	0.1326	1.8012	-0.42	-0.10
Loop 2	0.1839	1.6308	0.0918	1.4792	0.0542	2.1004	-50.08	-9.30

Table 5.9: Summary of MRD values for TC1 and the sensitivity analysis case with a 5% error in the global stiffness matrix.

TC1	Reference		SA: 5% Error in $\mathbf{K_S}$		Difference [%]	
	MRD_d	MRD_F	MRD_d	MRD_F	MRD_d	MRD_F
Loop 1	0.2353	1.7114	0.2378	6.6745	0.89	290.30
Loop 2	0.1855	1.6350	0.1847	6.5770	0.11	302.57

A quick analysis of the MRD values for the lack of nodes SA case shows that the influence of four lacking measurements is negligible for the forces in both TCs. Since the first loop imposes a curve-fit over the span of the wing for the force, it is assumed that no large local changes will occur for the forces when one individual node is missing. The MRD for the deflection shows a maximal mean value of -50.08% difference between the reference and SA case for TC2 after the second optimisation loop. This shows that the lack of measurements may also benefit the system and is thus also a random error in the framework. In some cases, a particular node may be considered as driving the deflection further from the reference case, whereas another node may pull it towards it. This logic explains how lacking measurements have an arbitrary influence on the results.

For TC1 the lack of measurements does not seem to affect the results too much, especially when considering the mean values in Figure 5.9. Moreover, the overall deviation from the reference case is in the order of 0.4% which can be considered negligible. For the force ratios, there is no noticeable deviation between the plots including the SD of the analysis. The same can be said about the plots for TC2 after the first loop, Figure 5.10a and 5.10b. On the other hand, after the second loop, TC2 shows larger deviations from the reference, as well as a wider range of values within the $\pm 3\sigma$ regions. Hence, the behaviour of the framework under lacking measurements is random in the case of a unique data set without averaging. Once more it can be noticed, however, that the mean value seems to approximate the reference case within a fair margin as shown in Figure 5.10d when a mean sample is considered.

Error in the Stiffness Matrix

An error in the stiffness matrix is expected to be noticeable by a large error in the MRD of the applied force, while having a reasonable load shape in terms of aerodynamics. That is, due to the relation between force and deflection, the optimiser will manage to adjust the forces such that the deflection is reached. Therefore, an error in MRD_d is expected to be small, while having a constant error in MRD_F due to the relation given by Equation 4.2. To assess this, a 5% error was imposed on the global stiffness matrix $\mathbf{K_S}$ for all of its terms. In reality, this figure can be reduced by performing for example ground vibration tests to be in the order of 1%, but for the purpose of the sensitivity analysis it is increased such that its effect will be predominant. The framework was run for both TCs with an error in $\mathbf{K_S}$ for which the MRD results are shown in Table 5.9 and 5.10 and the graphs for the ratios are provided in Figure 5.11 and 5.12.

The MRD results confirm the expectations following from the relation between the force and the deflection, caused by the global stiffness matrix. Not much can be derived from the deflection graph as the optimiser manages to obtain the right deflections. While MRD_d values are relatively comparable to the reference

Table 5.10: Summary of MRD values for TC2 and the sensitivity analysis case with a 5% error in the global stiffness matrix.

TC2	Reference		SA: 5% Error in $\mathbf{K_S}$		Difference [%]	
	MRD_d	MRD_F	MRD_d	MRD_F	MRD_d	MRD_F
Loop 1	0.2375	1.7153	0.2384	6.6815	0.38	289.52
Loop 2	0.1839	1.6308	0.1850	6.5790	0.60	303.42

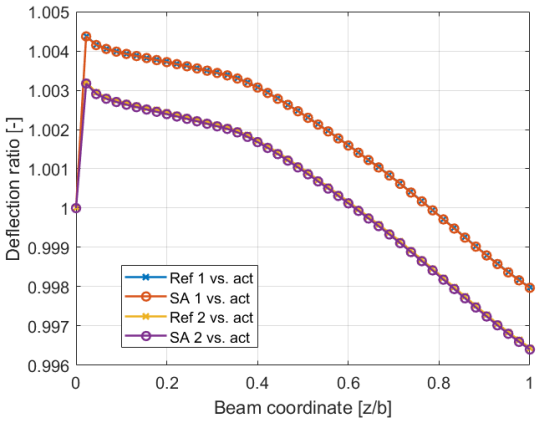

(a) Ratio of deflections of the optimised and actual values after the first and second optimisation loops.

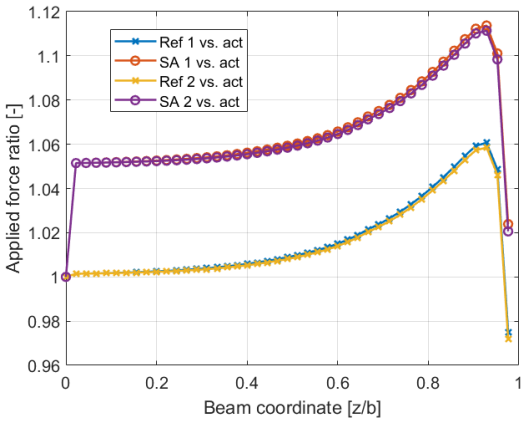

(b) Ratio of applied forces of the optimised and actual values after the first and second optimisation loops.

Figure 5.11: Results of TC1 with a 5% error in the global stiffness matrix for the sensitivity analysis case compared to the reference case with no error in $\mathbf{K_S}$.

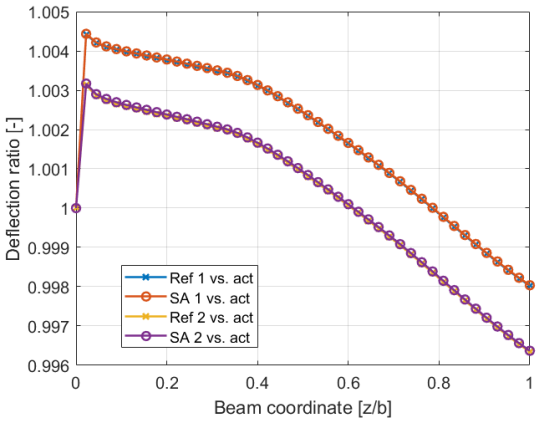

(a) Ratio of deflections of the optimised and actual values after the first and second optimisation loops.

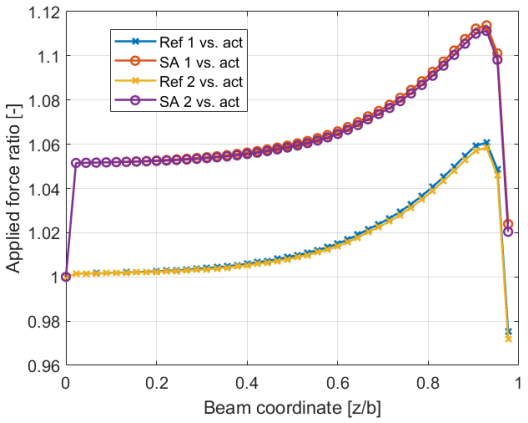

(b) Ratio of applied forces of the optimised and actual values after the first and second optimisation loops.

Figure 5.12: Results of TC2 with a 5% error in the global stiffness matrix for the sensitivity analysis case compared to the reference case with no error in $\mathbf{K_S}$.

Table 5.11: Summary of the parameter values for the pseudo-experimental case.

Parameter	Value
Rounding	Third digit (0.001)
Random Error	$\pm 0.001\ m$
Lack of Measurements	10%
Error in $\mathbf{K_S}$	1%

Table 5.12: Summary of MRD values for TC1 and the pseudo-experimental sensitivity analysis case. The mean and standard deviation values are shown for 50 random error vectors and the difference applies to the mean of the MRD values.

TC1	Reference		SA: Pseudo-experiment				Difference of mean MRD [%]	
			Mean		SD			
	MRD_d	MRD_F	MRD_d	MRD_F	MRD_d	MRD_F	MRD_d	MRD_F
Loop 1	0.2353	1.7114	0.3363	2.1700	0.1944	1.8058	42.92	26.80
Loop 2	0.1855	1.6350	0.3750	3.2151	0.2129	1.5553	102.16	96.64

cases (<1% difference), MRD_F shows that for both TCs, the SA case is off by a roughly constant factor, as the forces need to be larger to cause the same deflection. This is visualised in the ratio of the applied force graphs as per Figure 5.11b and 5.12b, where a near-constant difference of about 5% is present between the reference and SA case. This corresponds to the value of the artificial error in $\mathbf{K_S}$. The second loop behaviour on the force optimisation shows similar behaviour for the SA case as it does in the reference case. Hence, an error in the stiffness matrix would induce a systematic error into the framework. As was the case with the lacking nodes, the variation in the relative deflection with respect to the reference case is negligible as it is in the order of 0.5%. Since the error in the stiffness matrix is expected to affect only the forces, this is a peculiar result. It is explained by the way that the optimiser is affected by the forces. When the forces are adjusted differently due to a variation in $\mathbf{K_S}$, the deflection varies as well and while the optimiser considers only deflection, it allows a margin in the optimal value given by the tolerance on the objective function. Hence, under different forces, the converged solution may be slightly different from the reference case, even though the input deflection is exactly the same as opposed to other SA cases.

5.2.2. Pseudo-Experimental Parameter Set-Up

Following from the individual parameter study, a pseudo-experimental case can be designed which takes into account common experimental flaws in both the measurements and the model. In terms of the proposed framework, the parameters for a pseudo-experimental scenario are provided in Table 5.11. With these input values, an artificial data set can be analysed in a similar environment as an experimental data set. In other words, these parameters allow the simulation of experimental measurements.

With the pseudo-experimental parameters, the framework is deployed on the two test cases as per section 5.1. The MRD values are compiled in Table 5.12 and 5.13 for TC1 and TC2, respectively, and the ratio plots are shown in Figure 5.13 and 5.14. Since now the random error and lack of measurement parameters are both included, both pseudo-experimental cases are performed 50 times on different random sets to generate a statistical analysis.

By looking at the MRD values as displayed in Table 5.12 and 5.13, it is clear that for larger deflections the framework will become less sensitive to the errors. This was previously concluded due to the fact that as the deflections increase, the relative changes in force reduce with respect to local errors. Moreover, both the rounding and random errors induce an increase in the MRD values for the deflection and applied force.

Table 5.13: Summary of MRD values for TC2 and the pseudo-experimental sensitivity analysis case. The mean and standard deviation values are shown for 50 random error vectors and the difference applies to the mean of the MRD values.

TC1	Reference		SA: Pseudo-experiment				Difference of mean MRD [%]	
			Mean		SD			
	MRD_d	MRD_F	MRD_d	MRD_F	MRD_d	MRD_F	MRD_d	MRD_F
Loop 1	0.2375	1.7153	0.1826	2.5639	0.0920	1.8188	-23.12	49.47
Loop 2	0.1839	1.6308	0.1723	2.5216	0.0870	1.8617	-6.31	54.92

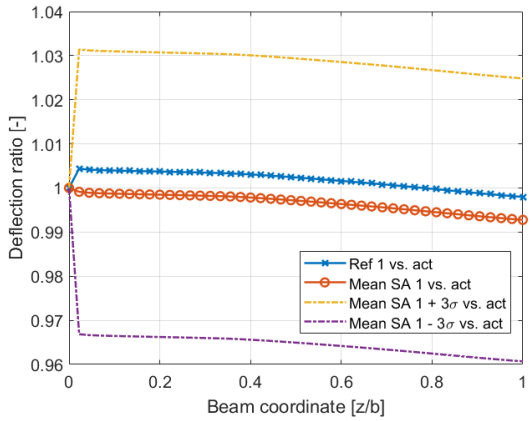

(a) Ratio of deflections of the optimised and actual values after the first optimisation loop.

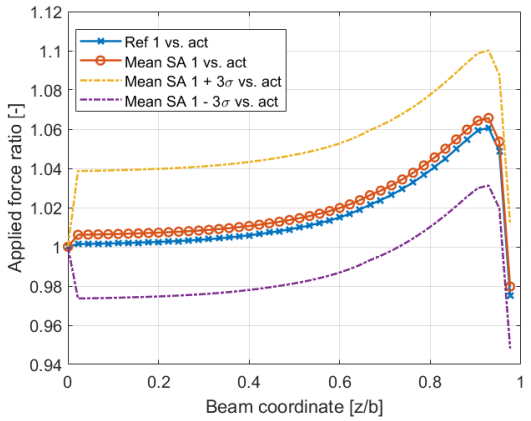

(b) Ratio of applied forces of the optimised and actual values after the first optimisation loop.

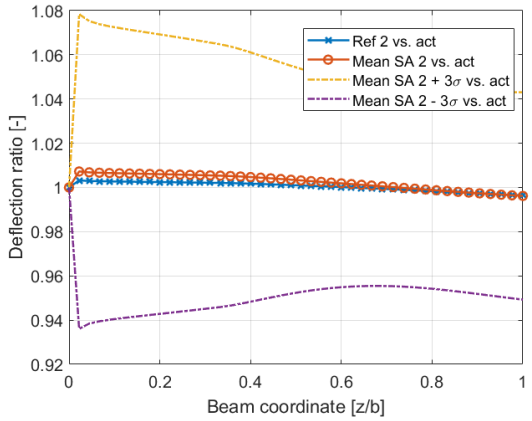

(c) Ratio of deflections of the optimised and actual values after the second optimisation loop.

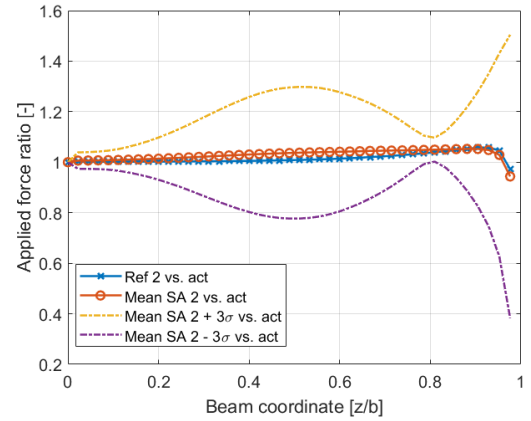

(d) Ratio of applied forces of the optimised and actual values after the second optimisation loop.

Figure 5.13: Results of TC1 with the pseudo-experimental parameters for the sensitivity analysis case compared to the reference case. The statistical mean over 50 loops with random errors is shown along with the $\pm 3\sigma$ curves.

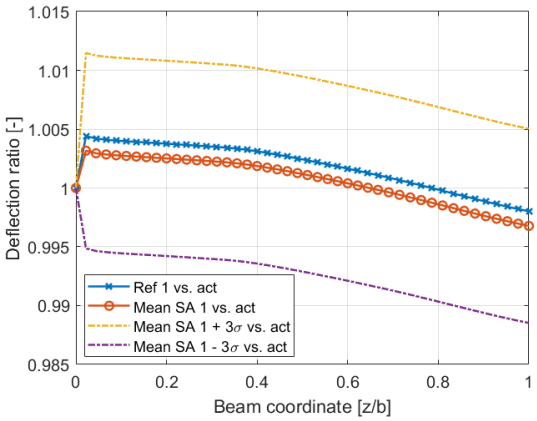

(a) Ratio of deflections of the optimised and actual values after the first optimisation loop.

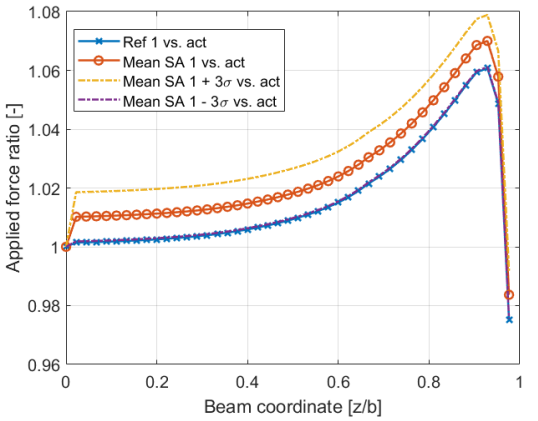

(b) Ratio of applied forces of the optimised and actual values after the first optimisation loop.

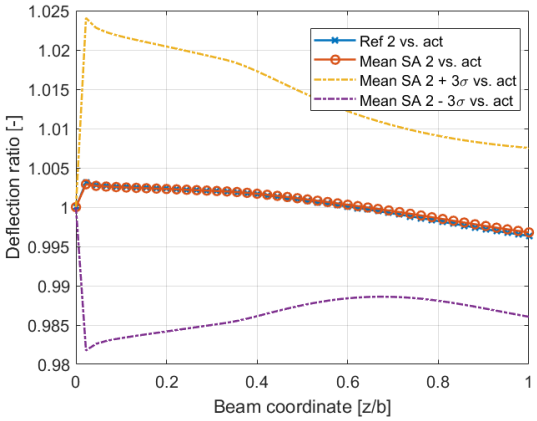

(c) Ratio of deflections of the optimised and actual values after the second optimisation loop.

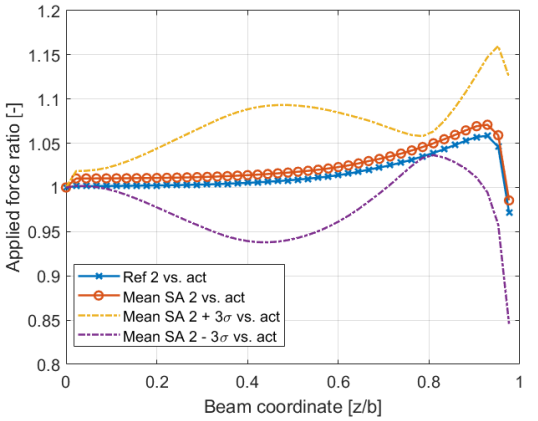

(d) Ratio of applied forces of the optimised and actual values after the second optimisation loop.

Figure 5.14: Results of TC2 with the pseudo-experimental parameters for the sensitivity analysis case compared to the reference case. The statistical mean over 50 loops with random errors is shown along with the $\pm 3\sigma$ curves.

Except for MRD_d in TC2 which shows an improvement in its value, it is clear that an experimental scenario induces more errors. The improvement in MRD_d is presumably an anomaly caused by the random variation, which was also found in the rounding. This implies that it would be suggestible to take several measurements of the same phenomenon such that the framework can be applied on each measurement. From these runs, statistical data seems to converge to the most accurate solutions and as such would provide quantitative insights with reasonable quality. Also, following from the error in $\mathbf{K_S}$ being 1% and it being shown previously that this would correspond to an error in the force of about $\Delta MRD_F = 1\%$, the resultant $MRD_F = 1.5553\%$ from the pseudo-experimental TC1 case is acceptable. In the same logic, TC2 which employs the pseudo-experimental parameters provides an acceptable 1.8617% in MRD of the applied force. Considering that the result from the framework in a simulated experimental environment contains an error of at most 2% for TC2, the framework is deemed to cope well with the four experimental flaws which were considered.

The 1% difference caused by the error in K_S is clearly visible in the ratio of applied forces plots as per Figure 5.13b and 5.14b. It is again shown that the quality of the framework's output improves in terms of accuracy when the deflections increase as per TC2 with respect to TC1 as seen by the lower visible variation of the ratios. Moreover, similar behaviour after the second optimisation loop for both TCs is seen when compared to the previous parameter study. Especially the behaviour of the random cases involving the error and lacking measurements can be noticed after the second loop, where over-fitting occurs which impose large fluctuations in the standard deviation curves that may become noticeable with singular measurements. The mean deflection curve after the second loop also shows to match the reference case closer than after the first loop as seen in Figure 5.13c and 5.14c.

5.3. Discussion

Concluding this sensitivity analysis and therefore the numerical assessment of this study, it is now known how the framework behaves given certain errors and experimental imperfections such as the measurement accuracy or the global stiffness matrix error. It is clear that the framework relies on accurate measurements, yet it remains robust in a situation where measurements are less reliable. It was found that under pseudo-experimental conditions, the framework may have an error of up to 2% in its force predictions. To achieve this result, the framework relies on an initial shape function for the aerodynamic load which must represent the aerodynamic behaviour in the actual encounter. This also provides the framework its robustness, as it will always have a reasonable first guess at the load which caused the measured deflection. The result mentioned here was realised with the consideration of a 1% error in the global stiffness matrix, which has the largest systematic influence on the results.

The influence of an accurate FEM model should therefore not go unnoticed, as any error in this model will induce equally large systematic errors in the results. While measurement methods are not readily improvable in terms of accuracy, it is feasible to reduce the systematic error caused by the FEM model's lack of similarity. The systematic error in the FEM model is represented in the extraction of the forces while the deflection is only affected marginally. Moreover, this induced systematic error increases linearly for all deflections and is constant across the span. This is the same conclusion which Gherlone et al. arrived to as discussed in subsection 2.1.2 [14].

This numerical analysis also emphasised the importance of an accurate measurement method. In order to reduce the random errors created by the measurement method in terms or rounding, accuracy and local lacking measurements, it is advisable to assess the application of different measurement methods to see how the accuracy varies with respect to marker-tracking method. Finally, the cases in which random values were considered showed that the mean of such results tend to converge to the reference case. Hence, considering multiple measurements for the same case would also provide a clearer insight into the results as any random error may be averaged out. It is noted that the systematic error of the stiffness matrix will not be affected by multiple measurements as it will be a consistent deviation from the actual wing model.

This behavioural sensitivity analysis shows that through multiple measurements, statistical convergence can be achieved in order to mitigate any random error. Moreover, the random errors have a larger influence on the result when deflections are small as the relative error is then larger. On the other hand, the systematic error caused by the error in the FEM model will increase linearly in terms of extracted force for varying deflection. Thus, as the deflections become larger, one may expect less influence of the random error and more influence from the systematic error in the FEM model. Also, the flexibility of the model itself may affect how much the random errors influence the model as local deviations become larger with less flexible models. Models with higher flexibility will not be affected as much by local deviations, as less force is required to

impose such a deviation for a more flexible model.

Lastly, by taking multiple measurements, lacking nodes may be resolved as this varies per measurement. While one track may not be available in a first series, it may be present in subsequent measurements which allows for averaging processes. This also applies to the effect of rounding and random errors. For oscillatory cases, a singular measurement may be phase-averaged to reduce the effect of random measurement errors.

6

Experimental Validation

In order to demonstrate the capabilities of the proposed framework to match the research purpose, it will be put to the test in an experimental environment. In the process, an attempt will be made towards the validation of its performance with respect to the characterisation of an aeroelastic problem. The experimental approach and the manner in which the validation data set is extracted was previously discussed in chapter 3.

With clarity on how the experimental data was retrieved, the report has arrived at the application of the proposed framework on real-life data to evaluate its performance in a non-ideal environment. The marker-tracking data as retrieved from the discussion in chapter 3 needs further post-processing such that it can be used in the framework. This process will be explained in section 6.1. Then, two situations will be considered for the evaluation of the proposed framework in an experimental environment. In first instance, section 6.2 will show the results of the framework in a static test case. Secondly, the framework will be used with data from a harmonic gust case to assess its performance in a dynamic case as will be explained in section 6.3.

6.1. Data Post-Processing

In order to be able to use the data from the experimental campaign discussed in chapter 3 based on the work of de Rojas in [7], further post-processing of the markers was required to obtain a better quality of results. In general, since this thesis applies beam-modelling and the marker grid provides 3D data of the displacement, the first step was to project this data onto the 1D beam. From the previous assessment on the influence of the bend-twist coupling – which could be neglected (see section 4.2) – a reasonable approach is to take the average displacement of all the chord-wise markers. Since each marker is assumed to have the same displacement in the absence of twist, this allows for a first smoothing of the measurements. By taking the average of seven chord-wise markers, the effect of the random error is reduced in addition to the averaging process over several measurements.

For a static case, the beam-like data can now be used in the framework to extract the aerodynamic load, as no inertial load is present, after mapping the data onto the FEM nodes as discussed later. As for the dynamic cases, the accelerations must be extracted from the marker data. Since the marker data is prone to measurement errors as discussed in the sensitivity analysis, straight-forwardly taking the gradient of the marker measurements in time twice provides noisy results as seen in Figure 6.1a. Hence, a different approach is required. Firstly, the deflection measurements are phase-averaged across the available measurement data of a harmonic gust with a constant frequency and amplitude. In addition to the chord-wise averaging, this will aid in providing smoother data for the deflection of a certain node throughout the oscillation. Then, the phase-averaged sinusoid of the deflection during one oscillation is fitted using a generic function for oscillations, given by Equation 6.1 with A, B, C and D constants. A is related to the amplitude, B will depend on the oscillation frequency, C represents a phase shift and D the static deflection caused by the wing's AOA.

$$f_{fit}(x) = A \cdot sin\,(B \cdot x + C) + D \tag{6.1}$$

Since the generic shape of the oscillation is the same for each marker on the beam with varying amplitude and static deflection (A and D), this fit can be applied to each phase-averaged marker deflection curve. This provides a continuous solution for the deflection of each marker throughout the oscillation. The sine fit is shown in Figure 6.2 for the phase-averaged tip marker deflection measurements. Performing this fitting for

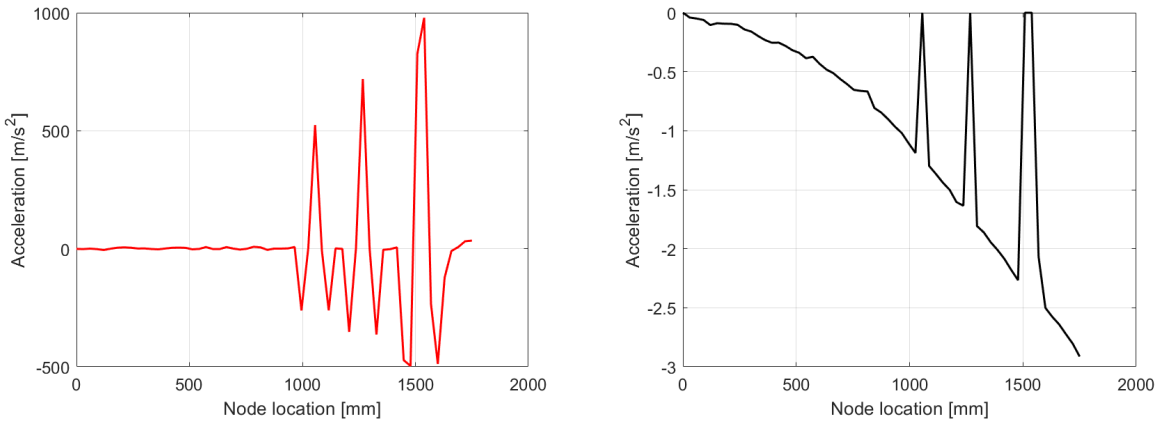

(a) Result from the direct numerical differentiation approach.

(b) Result from the phase-averaging approach.

Figure 6.1: Comparison of the results of the acceleration at the oscillation time of 0.092 s using the direct and the phase-averaging approaches.

each marker and then taking the value of all the fits at the same oscillation phase, one may find the instantaneous deflection of the entire wing. This is demonstrated in Figure 6.3 for an arbitrary oscillation time of 0.092 s (maximal amplitude) for a harmonic gust of 2 Hz, $AOA = 3.32°$ and a gust amplitude of $\pm 5°$, on which more later. The resulting deflection shows zero-values, which are the result of faulty tracks in the STB analysis. Moreover, one can see that one curve is deviating from the same trend as the others. Hence, this approach may also visualise outliers which need to be taken out of consideration when applying the framework. As discussed in the sensitivity analysis, these can be taken out of consideration in the framework. By taking then the second derivative of Equation 6.1, one arrives at the acceleration of the markers during the oscillation and a similar approach may be done as for the instantaneous deflection. For illustration purposes, Figure 6.1b provides the instantaneous acceleration at the same oscillation time of 0.092 s. As expected, at the maximal deflection point the acceleration is in the opposite sense due to the derivative of the velocity's cosine resulting in a negative sine. Furthermore, using the formula for the instantaneous acceleration in a harmonic oscillation given by Equation 6.2, one may find for an oscillation amplitude A of 18.51 mm and $\omega = B = 12.55\ rad/s$ that the acceleration $\ddot{x}$ should equal $-2.92\ m/s^2$ [47]. This value is reflected in Figure 6.1b, which shows an acceleration at the tip of $-2.91\ m/s^2$. The values for the oscillation amplitude and angular velocity ω were taken from the fit function, where the latter matches also the theoretical value $\omega = 2\pi \cdot f = 12.55\ rad/s$ with a gust frequency of $f = 2\ Hz$ which shows that the fit function represents the oscillation well.

$$\ddot{x} = -A \cdot \omega^2 \tag{6.2}$$

Finally, the wing has a total of 59 span-wise markers across its planform. The respective FEM model, however, has a total of 44 nodes when disregarding the root node as it is fixed at zero. To use the marker measurements for this analysis, the results of the deflection and acceleration must be projected onto those 44 FEM nodes. A simple algorithm was used to achieve this. It searches for the two markers which neighbour a FEM node location and then linearly interpolates the values of the markers towards this FEM node with a weight respective to the individual distance of each of the markers to the node. Null values are ignored and further linearly interpolated with the next neighbour. The result of this mapping process of the deflection for the oscillation time of 0.092 s from the markers to the FEM nodes is shown in Figure 6.4. It shows that there is a region near the tip with large deviations from the rest of the deflection. This is the effect of the linearisation process with the null measurements and the outlier which was considered in Figure 6.3. These nodes may be neglected in the final analysis. The same is performed for the acceleration. This procedure is applied after removing the first 5 cm from the marker measurement grid, as this is situated in the aluminium clamping region which is assumed to be rigid for the structural assessment.

6.2. Static Case

The static test case for this research was performed with a prescribed angle of attack of 5° and a free-stream velocity of 14 m/s. Measurements were taken across the entire wing and the markers were processed as per

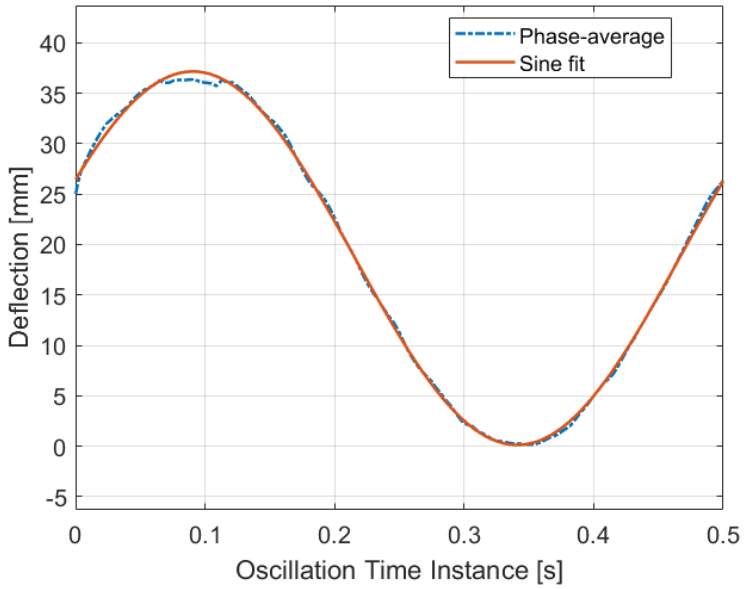

Figure 6.2: The sine fit on the phase-averaged marker data for the tip marker.

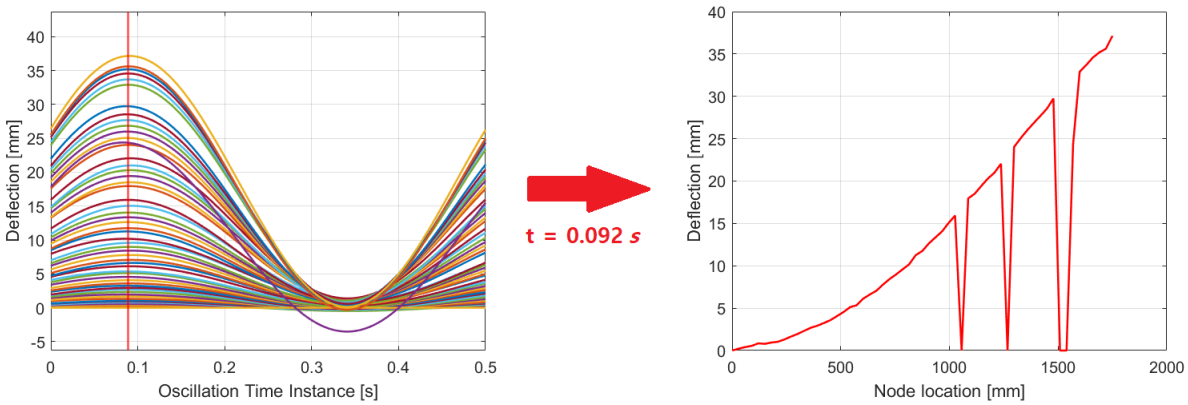

Figure 6.3: All the sine fits for each individual marker (left) and the resulting instantaneous wing deflection (right) following from the same oscillation time of 0.092 *s*.

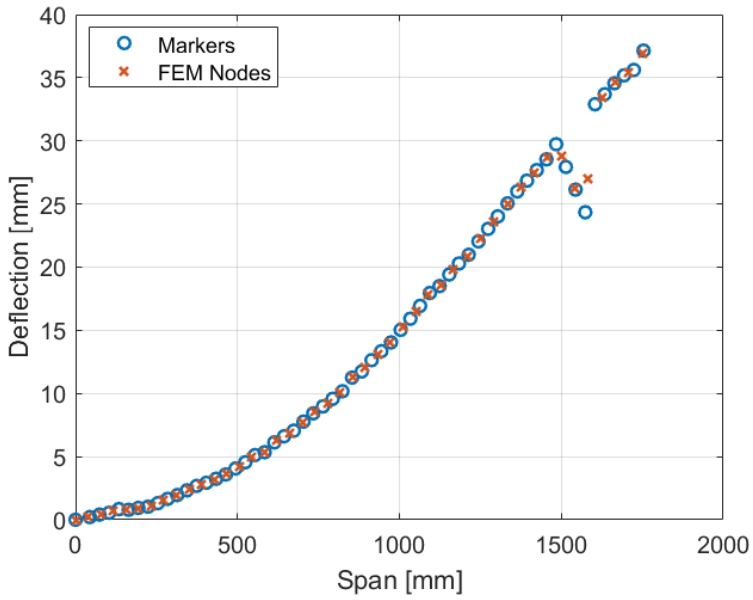

Figure 6.4: The mapping of the marker measurement results of the deflection to the FEM nodes.

the procedure described in the previous section. The results from the framework are shown in Figure 6.5. The deflection is plotted in terms of the actual marker measurements excluding the null/outlier nodes as well as the deflection which is caused by the theoretical VLM load. The resulting deflection from the framework is also plotted for both optimisation loops. Similarly for the aerodynamic load, the lift from circulation is plotted along with the lift from VLM and the result from the two optimisation loops.

Noticeable is the large deviation in the prediction from VLM with respect to the measured deflection and the framework's output in Figure 6.5a. The tip deflection under the VLM load is 28.4 mm, whereas the measured tip deflection is 18.5 mm. This large deviation is further discussed later when assessing the effective AOA which appeared to be 3.32° rather than the suggested 5°. From the framework, loop 1 and loop 2 provide respectively a tip deflection of 20.2 mm and 21.2 mm. Here, the first loop has a better match with the tip deflection than the second loop, which is likely caused by the second loop attempting to match the mid-span region more. The overall shape of the deflection seems to match with the optimisation loops, though the tip region shows larger deviations. Looking at solely the marker deflections, however, there is an unexpected behaviour in the marker tip region. The marker deflection bends back in a negative sense, which does not correspond to an aerodynamic load situation. The cause of this could be in the measurement of the markers itself, being prone to errors.

Looking then at the results from the load predictions in Figure 6.5b, again the VLM-based prediction shows a large deviation in maximal lift load near the root: 15.0 N/m from VLM versus 11.2 N/m from the optimisation. Considering the match between the lift based on circulation found from PIV and the framework near the tip region, one can consider that the framework manages to find a more accurate load distribution than VLM predicts especially at the tip region for 5° AOA. Moreover, since the match between the framework and the circulation result is good, it is assumed that the stiffness matrix does not contain large errors. Thus, the deviation between VLM and the framework's output gives rise to two considerations:

1. **The experimental conditions used to generate the VLM loads may be wrong.** VLM has proven to provide good results especially in static cases. Hence, such a large deviation here is unexpected. It can be related to errors in the actual angle of attack or wind-speed velocity used during the static case. Due to the sensitivity of the theoretical model to input conditions, this may be the cause of the deviation.

2. **The wind tunnel measurements may be influenced by empirical imperfections.** Due to empirical imperfections such as model imperfections or measurement flaws, the theoretical and actual loads may differ. Other flow imperfections or model attributes such as the zig-zag strips which are not incorporated in VLM may also further generate deviations between theory and practice.

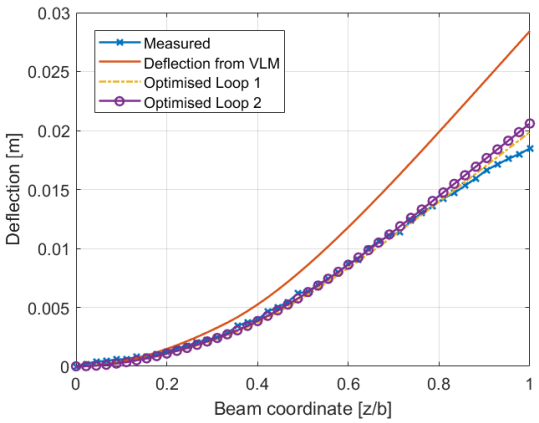

(a) Deflection plot of the wing from the measured marker deflections, the VLM-predicted loads and the two optimisation loops.

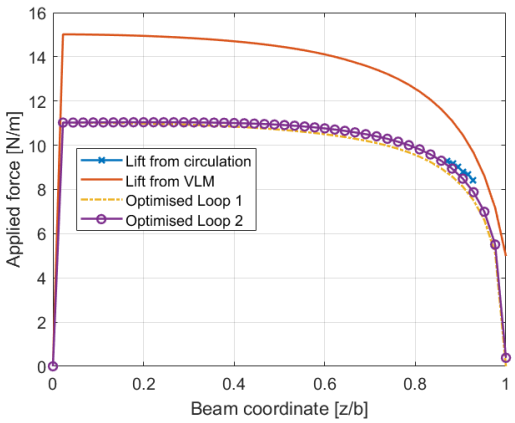

(b) Aerodynamic load plot of the wing from the PIV circulation approach, the VLM-predicted loads and the two optimisation loops.

Figure 6.5: Deflection and lift load for the static test case with a prescribed angle of attack of 5° and a constant wind speed of 14 m/s on the wing model.

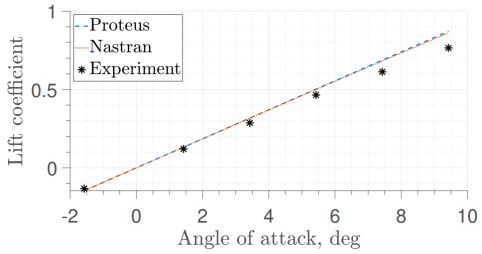

Figure 6.6: Lift coefficient versus angle of attack for the wing in the design study by Mitrotta et al. [30].

These two statements may have a large influence in the validation efforts for the dynamic case, as there are no circulation-based loads for that case. The dynamic case will be validated with MSC.Nastran, which also incorporates VLM for its aerodynamic load prediction, and will be further elaborated upon later. If, however, the measurement conditions are off or the empirical imperfections have too big of an influence on the loads, these efforts may not provide a realistic insight.

Of the two statements above, the former can be further supported with the application of experimental lift curve data obtained in the design study of this particular wing by Mitrotta et al. [30]. In this study, a static deflection test was performed at 25 m/s for varying angle of attack in the same wind tunnel, the OJF. The resultant lift coefficient curve is shown in Figure 6.6, compared to numerical studies with Proteus and MSC.Nastran. While measurements were taken at an interval of 2° between -2° and 10°, the plot shows a deviation in AOA measurement of 0.58° which was required to correct for a mismatch in the measured and effective AOA based on the zero-lift AOA. Since the same wing model was used for this experiment, the effective AOA must be adjusted by this 0.58° difference. Using then the effective AOA of $5 - 0.58 = 4.42°$, the analysis is repeated. The value achieved for the net root force from VLM now more closely matches the value found from the force balance as per Table 6.1, where VLM predicts this force to be 21.1 N for 4.42° as opposed to 23.1 N for 5°. Hence, it is therefore suggested that indeed the AOA listed in the static experimental campaign was not the effective aerodynamic angle of attack as depicted in the campaign. This error is likely to have been caused by a misalignment between the rotation table and the wing itself.

It is further noted that for the predicted root force from VLM for 4.42° of 21.1 N, a $C_{L_{VLM}}$ is found of 0.40. Comparing this to the result of 15.8 N for the force balance measurement which gives a $C_{L_{eff}}$ of 0.30, it is found that there is still a large deviation in the lift coefficient. It is assumed that the force balance is measured under the correct effective AOA. Looking then again at Figure 6.6, there is no such large deviation between the VLM-based MSC.Nastran prediction and the experimental measurement at $AOA = 4.42°$. Assuming that this VLM prediction perfectly matches the experimental measurements for the static case and that the lift coefficient is linear in this small-angle region, one may argue that the ratio of the lift coefficients and AOAs should match. The following relation can then be used to find a new effective AOA:

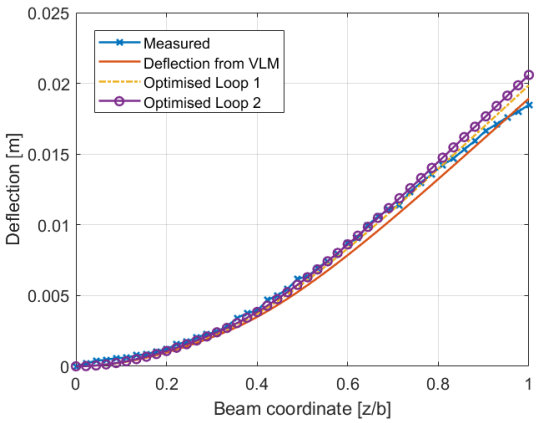

(a) Deflection plot of the wing from the measured marker deflections, the VLM-predicted loads and the two optimisation loops.

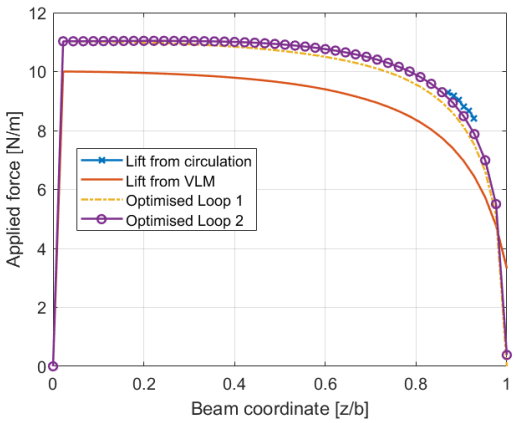

(b) Aerodynamic load plot of the wing from the PIV circulation approach, the VLM-predicted loads and the two optimisation loops.

Figure 6.7: Deflection and lift load for the static test case with an effective angle of attack of 3.32° and a constant wind speed of 14 m/s on the wing model.

Table 6.1: Results for the static case with $AOA = 5°$, 14 m/s and varying AOA for VLM simulations in terms of net lift force measured at the root of the wing.

Force Balance	Framework	VLM (5°)	VLM (4.42°)	VLM (3.32°)
15.8 N	17.8 N	23.1 N	21.1 N	15.8 N

$$\alpha_{eff} = \frac{C_{L_{eff}}}{C_{L_{VLM}}} \cdot \alpha_{VLM} = \frac{0.3}{0.4} \cdot 4.42° = 3.32° \tag{6.3}$$

Using this information on the effective angle of attack, a new static case was run now with VLM for $AOA = 3.32°$. The deflection and load plots are shown in Figure 6.7. In the figure for the deflection, it can now be seen that the VLM deflection matches the measurements more closely. Also, VLM estimates the net root force to be 15.8 N for 3.32° AOA as seen in Table 6.1, exactly matching the force balance measurement. In Figure 6.7b, it still shows that only the framework matches the lift from the circulation whereas VLM underpredicts this load. This indicates that the net root lift force may be affected by certain factors. One such factor is the boundary layer of the splitter table which was used in the experiment. This may have caused the lift generated near the root to be smaller, which would then reduce the total lift generated by the wing and thus also reduce the lift coefficient. Another factor may be the wind tunnel jet expansion effect due to the OJF being an open jet wind tunnel. This combination effectively reduces the lift generated by the wing especially near the edges of the jet which in this case was the root of the wing, where the lift is largest. The forces near the root region also have a smaller effect on the bending of the wing than the tip forces, which is why the tip region forces have a more prominent role in the deflection and thus on this framework. This explains the close match of the framework's prediction with the lift from circulation in the tip region while having a 12.6% increase in net root force when compared to the force balance.

Furthermore, it is suggested that the behaviour of the marker measurements near the root as visible in Figure 6.7a by the blue crosses influences the framework prediction, where the local measurements show a relatively larger deflection with respect to the deflection from the framework load. This sudden deflection is likely to impose larger forces on the framework and this is reflected in the total lift force. This deflection is an unexpected behaviour in the beam's deflection and is suspected to be related to the measurement error, depicting the importance of reliable measurements. A similarly unexpected behaviour is found in the tip region where the tip seems to bend in the opposite direction of the lift load. Finally, it can be seen in the load plot of Figure 6.7b that the second optimisation loop adjusts towards the circulation-based lift load, effectively emphasising the importance of the second optimisation loop where the optimiser has more freedom in adapting the forces locally. It is noted that the span-wise element in which circulation data was available is limited due to the limited measurement time-frame.

The deflection measurements in this example are the result of an averaging process in the time domain over a span of 18.3 s with a sampling frequency of 831 Hz. This translates to a total of roughly 15,000 mea-

surements. From the results of the SA in chapter 5, it was shown that already with 50 measurements the effect of random errors can be ignored in the mean approach. This effect is also seen in the present static test case as there is no unexpected random variation in the load distribution as was seen in the standard deviations of the random error case.

In conclusion, the framework manages to extract the aerodynamic loads for this static case when compared to a local tip measurement. This is the most important result from this static test case, demonstrating the feasibility of the framework. It is noted that the tip region is more intricate in its prediction due to tip losses, and thus a match with empirical data is a favourable result. More spanwise measurements would be ideal to further validate the load curve obtained through the framework in the root region. A comparison with VLM showed implications that there were losses of lift near the root due to wind tunnel and boundary layer effects on the splitter table, reducing the measured net root force. Additionally, it is apparent that the accuracy of the marker measurements plays a key role in the framework as it may attempt to over-fit locally, generating a deviation between the measured and calculated forces. The effect of taking multiple measurements of the same case allows for the reduction of the influence of random errors in the measurements, while systematic errors in for example the stiffness matrix will continue to have the same effect consistently.

6.3. Dynamic Case: Harmonic Gust

For the dynamic case, first it is ensured that it was also conducted with an AOA of 3.32°. Then, a validation tool is used as was briefly mentioned previously. This tool is MSC.Nastran, which is an aeroelastic solver commonly used in industry and scientific research [49]. This section will also elaborate on this validation effort prior to discussing the framework results.

Preliminary Effective AOA Assessment

In order to ensure that the dynamic case was also conducted with a mean initial wing AOA of 3.32°, the marker data is assessed. This preliminary check is required as the dynamic experiment had a prescribed AOA of 5°, similar to the static case which has been shown to instead being an effective AOA of 3.32°.

To achieve this goal, it is possible to use the curve-fitting data from Equation 6.1 in terms of the final coefficient D. In essence, this coefficient represents the static deflection around which the oscillation takes place. In theory, the value of D at a certain node should equal the deflection of that node in the static case with an equivalent AOA and V_∞ if a flat plate would be assumed. For the purpose of this assessment, the tip node is considered. This is possible under the assumption that the wing oscillates an equal amplitude around this point, which can be done when ignoring the effect of wing twist during the oscillation.

The tip node in the static case experienced a measured deflection of 18.5 mm. From the phase-fitted fitting curve for the tip node deflection oscillation, the value D was found to equal 18.6 mm. Due to this match between the static tip deflection and the value of D which represents the static deflection in the fitted curve, it is assumed that the wing AOA was also 3.32° for the dynamic case.

Validation with MSC.Nastran

A shell model of the experimental wing in MSC.Nastran was generated in previous research at the department of Aerospace Structures & Materials at Delft University of Technology. This shell FEM model was used in this campaign to assess the gust response under the same prescribed conditions as the experimental case. For this particular dynamic case, it was a harmonic gust with a frequency of 2 Hz, an initial effective AOA of the wing of 3.32° – which was originally intended to be 5° – and a gust amplitude determined by the angle of the gust vanes of the gust generator, which varied between $\delta_G = \pm 5°$. This translates to a reduced frequency for this wing of $k = 0.11$ and implies that the flow is unsteady. Following from the work of Lancelot et al. [22], an approximate relation between this gust angle and the provided gust vane angle is $\alpha_G \approx \delta_G/2$ with the installed gust generator. Since the gust vane angle for this case being ±5°, the gust angle may be approximated as $\alpha_G \approx \pm 2.5°$. Using then the relation of Equation 6.4, it is possible to estimate the gust velocity as $V_G \approx \pm 0.61\ m/s$ [7].

$$\alpha_G = \arctan\left(\frac{V_G}{V_\infty}\right) \tag{6.4}$$

MSC.Nastran has various solution sequences which provides support for multi-scenario analyses. For a dynamic aeroelastic analysis, the solution sequence SOL146 is required. This sequence allows for the simulation of the wing in gust, where the gust can be modelled in either a discrete or harmonic way. For this purpose, the harmonic gust as mentioned before is numerically prescribed to match the experimental measurements.

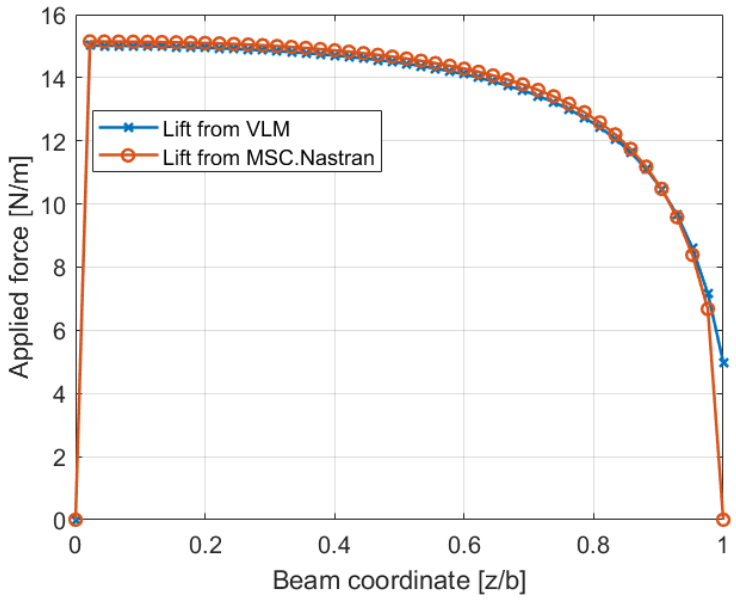

Figure 6.8: Comparison of the lift force from the VLM module used in this report and the VLM from MSC.Nastran at an AOA of 5° and a free-stream velocity of 14 m/s.

Since the initial AOA of the wing in gust is non-zero, it is required to also run a static aeroelastic analysis with $AOA = 3.32°$, which may be performed with SOL144. Since both sequences are linear, the resultant deflection and aerodynamic load of the static case can be added to the dynamic solution which then represents the experimental dynamic case. This combination of SOL144 and SOL146 is required since SOL146 has no natural support for initial angles of attack. Both cases have a free-stream velocity of 14 m/s and the dynamic simulation is ran for a total of 6 s such that the oscillation may stabilise in time.

Following from a static SOL144 reference case at 5° AOA and $V_\infty = 14\ m/s$, it is possible to do an initial assessment of the match between the MSC.Nastran shell model and the stiffness matrix as used in the framework, $\mathbf{K_S}$. Using the aerodynamic load in this static case as generated from MSC.Nastran (see Figure 6.8, the MSC.Nastran curve), the shell model experienced a maximal tip deflection of 23.3 mm. When applying MSC.Nastran's load to the stiffness matrix as used in the framework, a maximal tip displacement of 26.6 mm is found, which is a 14.2% increase over MSC.Nastran's prediction. This result implies that there is a discrepancy between the shell and global stiffness matrix model and the circulation-based lift result. The 14.2% increase in the deflection is closely related to the 12.5% increase in overall load found in the framework's prediction for the static case. This could imply that the stiffness in MSC.Nastran is smaller, and thus the deflection is smaller as well. Hence, the validation with MSC.Nastran for the $\mathbf{K_S}$-model is only approximate. From the result of the static analysis, where the load near the tip matched an empirical computation based on the global stiffness matrix, it is assumed that the $\mathbf{K_S}$-model represents the actual test wing sufficiently well to be used in this framework. When the absolute deflections become larger in dynamic cases, the effect of a mismatch between the FEM representation and the actual experimental model will linearly increase as was shown in the sensitivity analysis.

The static load distribution from the SOL144 reference case can also be compared to the VLM-predicted load for the original case with 5° AOA and $V_\infty = 14\ m/s$. This is shown in Figure 6.8, note that to compare the lift distribution on the same nodes, the loading was mapped to the FEM nodes similarly as the deflection and acceleration previously discussed. The comparison shows that the values differ slightly at all nodes. It is assumed that this is due to the influence of the wing's deflection on the aerodynamic shape. The VLM module in this report does not take that into account while MSC.Nastran does. Moreover, the aerodynamic grid used in MSC.Nastran is not the same as the one used in the VLM module, which was less refined. The conclusion from this comparison is mainly that the second optimisation loop is necessary for this analysis, as a generic aerodynamic load shape does not take into account wing deflection. Hence, the second loop allows the framework to make local adjustments according to such aeroelastic effects which are not incorporated into the theoretical LLT prediction.

Table 6.2: Characteristics of the harmonic gust for the dynamic test case.

V_∞	AOA	f	δ_G
14 m/s	3.32°	2 Hz	±5°

Lastly, as was discussed before, MSC.Nastran also uses VLM to predict the aerodynamic load. As with the static case, there may be empirical flaws in the initial AOA, free-stream velocity and the gust behaviour (frequency and amplitude) for the dynamic experiment. This needs to be considered in the discussion of the comparison between the framework output and the validation effort based on the effective AOA which was shown to be 3.32° and deviates from the intended 5°. Particularly for the dynamic case, the gust velocity which was calculated through an approximate relation may induce unwanted results.

Dynamic Case Results

In first instance, the dynamic case is characterised by the aspects as per Table 6.2 for a harmonic gust. The experiment is performed under the same circumstances as the static case, implying that the effective mean angle of attack of the wing was in fact 3.32° as was shown before by comparing the tip deflection. The results in terms of marker-displacement and acceleration were phase-averaged using the method discussed before. The data from the force balance at the root in terms of net total force in z (direction of lift) and the net moment in x (longitudinal axis of root-chord, bending moment), as well as the results from the MSC.Nastran validation scenario were also phase-averaged. The comparison between the three sources where applicable is made in Figure 6.9. Note that until now, the aerodynamic force and the resultant deflection were always considered in the positive sense. Due to the set-up of the force balance, however, a positive deflection was measured in the direction of negative lift for the balance. Hence, all graphs will be adjusted to be in the same reference system as the force balance. The net moment in x for the force balance is adjusted for the fact that the wing was in fact mounted 333.5 mm above the reference x axis in the force balance coordinate system. This includes the 5 cm aluminium clamped wing section.

The figure for the net total root force in z or the lift as per Figure 6.9a shows good overall agreement in terms of magnitude of the root force. It can be seen that there is an error at lower deflections (low net force) which is likely caused by the fact that for smaller deflections the relative error is larger. As per the sensitivity analysis, this has shown to increase the error. Looking at the higher load cases and thus higher deflection points, the error grows slightly larger with deflection. Following from the consideration in the sensitivity analysis, it is assumed that the stiffness matrix has an irregularity with respect to the actual model. Errors in the stiffness matrix are consistent and grow linearly with the load. Through the phase-averaging approach over multiple oscillations (up to 80 individual oscillations), it may be seen that the results do not show any effects of random errors. This has a similar effect as using statistical averaging to reduce the random influences in the SA. Finally, the wing was modelled in FEM as 1.75 m, where in reality it is 1.8 m and the 5 cm clamping region was assumed rigid. This assumption may have caused an error in the results as the deflection caused by the twist just aft of the clamping region may have increased the deflections overall. This is not taken into account for the framework.

Similarly to the net root force, Figure 6.9b shows the net root moment along the free-stream, which is created by the wing loading and may be called the wing bending moment. This moment was chosen since this gives an indication of how well the actual load distribution matches the predicted one. The moment is created by an equivalent resultant force of which the respective location of application represents the load distribution. A higher moment coefficient means a more tip-heavy load and vice versa. From the figure, it is noted that indeed the moment from the framework is larger than the moment as measured by the force balance. By considering the result from the net root force – which was also predicted larger than measured – this may be explained by the larger overall root force. Hence, there is no direct indication of large mismatches in terms of the instantaneous span-wise load distribution. Similar errors are found in the small deflection region with smaller loads, as the relative error in measurement is higher, and at larger deflections, where errors in the stiffness matrix $\mathbf{K_S}$ have a linearly increasing effect on the predicted forces.

For the net aerodynamic force at the root in Figure 6.9c, one can clearly see the influence of the error at smaller deflections. The error under larger deflections is assumed to be related to an error in the stiffness matrix as was found before in the comparison of the deflection of MSC.Nastran and $\mathbf{K_S}$ under the same load. It is noted that there is no plot for the force balance as the two forces at play (inertial and aerodynamic) cannot be separated for this measurement. Moreover, the difference between the first and second optimisation loops cannot be defined for the net root force at smaller deflections and at larger deflections it shows that

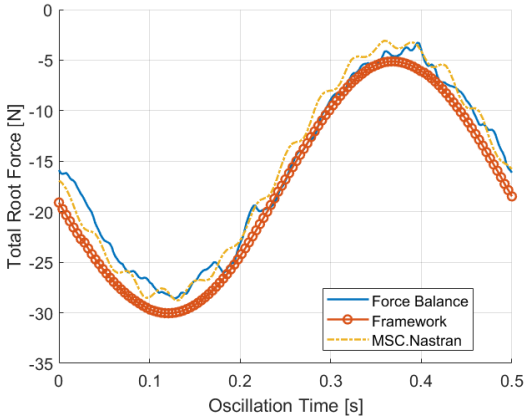

(a) Plot of the net total root force.

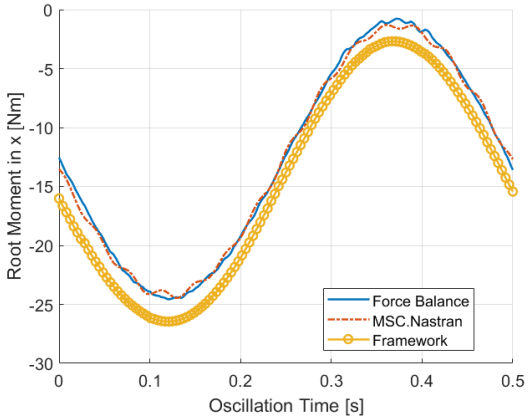

(b) Plot of the net root moment in x (around the root-chord axis).

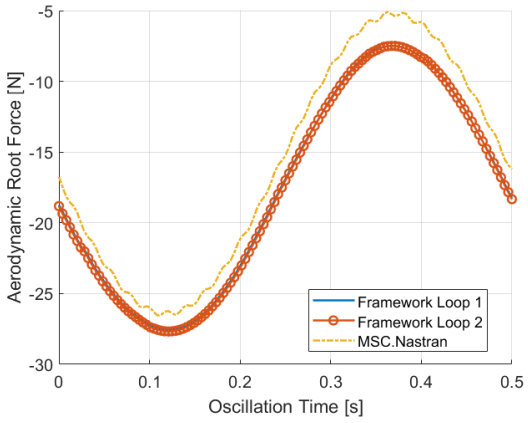

(c) Plot of the net aerodynamic root force.

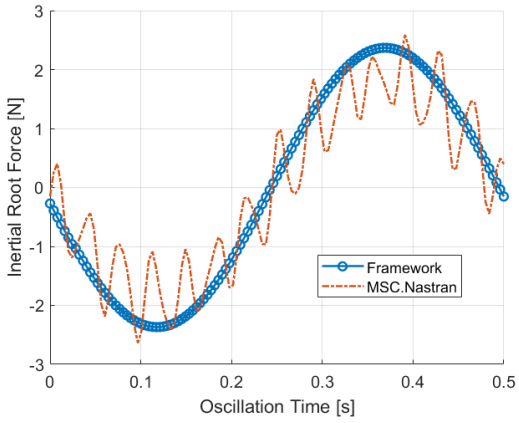

(d) Plot of the net inertial root force

Figure 6.9: Comparison of the results from the force balance, framework and MSC.Nastran over the oscillation period for a harmonic gust at 2 Hz, gust vane angle of $\pm 5°$, wing angle of attack of 3.32° and $V_\infty = 14\ m/s$.

the second loop results in a higher net root force. Furthermore, due to the close match between the total net root force for MSC.Nastran and the force balance, as well as the respective match in amplitude for the aerodynamic force between MSC.Nastran and the framework, the set-up of the validation sequence in MSC.Nastran may be considered reliable in terms of gust velocity V_G.

The inertial force in Figure 6.9d from MSC.Nastran and the framework show similarity in the overall amplitude of the curves. Especially considering the approximation of the mass distribution with volumetric calculations, the result does not vary much in overall amplitude with respect to MSC.Nastran. Other variations in amplitude may be caused by the variation of the deflection in MSC.Nastran and the experimental measurements, as it showed previously that for a static load the deflection does vary. Smaller deflections are expected in MSC.Nastran for the gust, implying that the accelerations will be smaller accordingly. Previously in the discussion of the sine fit for the deflection, at the tip a deflection amplitude of $A = 18.51\ mm$ was found, whereas MSC.Nastran predicts an amplitude of gust deflection of 14.9 mm. Since the acceleration amplitude is directly related to the amplitude of the deflection, this is a clear indication of this difference in inertial force. The reason for said difference in deflection could lie with the stiffness of the shell model varying with the experimental model. Noticeably is the secondary oscillation of the inertial force in MSC.Nastran, which is assumed to be caused by the sine gust input acting as a sudden step input at $t = 0\ s$ and activates a higher vibrational mode in the model. This was confirmed to match the structure's third vibrational mode at 28.8 Hz using MSC.Nastran's built-in eigenvalue analysis function. Lastly, MSC.Nastran did not take into account viscous damping as per its set-up. Hence, in reality it is expected that the amplitude of the oscillation in the curve of the inertial forces for MSC.Nastran is slightly lower due to the effect of damping.

Using the results as shown in Figure 6.9, the ultimate goal of the thesis can be reached as the FSI characterisation of a harmonic gust may be performed using the proposed hybrid numerical-experimental approach on a flexible wing. Since only measurement data of the markers has been used to predict the load with an iFEM framework, the original proposal is not compromised. The sole part which needs further validation is the exact distribution of these loads at instantaneous moments such that the prediction of the span-wise distribution can be confirmed. At this stage, there is no direct implication that this aspect is not accurate, given the good match between the predicted and measured moments. Finally, a comparison with MSC.Nastran showed that the proposed marker-based approach manages to extract the inertial forces from the motion of the wing.

7

Conclusion

The purpose of this thesis was to develop a framework which combines numerical and experimental evaluation techniques to quantify the three aeroelastic forces in the event of a harmonic gust with unsteady flow behaviour for a flexible wing. The proposed framework makes use of a marker-tracking technique and an inverse finite-element method (FEM) model based on the composite structure of the test wing to retrieve the span-wise aerodynamic and inertial force. It was developed based on a preliminary study on the shape of the load distribution, the FEM model and the inertial loads for a dynamic case. The framework uses two optimisation loops where the first attempts the scaling of a lifting-line theory (LLT) load curve to meet the measured deflection and the second then tunes the forces in a more local sense to match local deflections. The separation between the inertial and aerodynamic loads, and their resultant deflections, is done based on a linear separation of the two which allows for the characterisation of the three aeroelastic forces.

In order to understand the behaviour of the novel framework, a behavioural sensitivity analysis was conducted to assess how flaws in the modelling and acquisition during an experimental campaign may affect the results. The flaws which were considered were expressed in terms of measurement accuracy and FEM model representation of the experimental wing. It was found that the framework continues to provide accurate load distributions for the static numerical case even when such flaws were present. The result of the framework for a pseudo-experimental data-set which included the aforementioned flaws showed at worst a 2% error in its force prediction with respect to a reference case.

Following this analysis, the framework was used with experimental data for a static and dynamic test case with a flexible wing under a 3.32° effective angle of attack (AOA) and a free-stream velocity of 14 m/s in the Open Jet Facility (OJF) at Delft University of Technology. It was found that the lift distribution near the tip region matched data from local circulation measurements with particle-image velocimetry (PIV) and that the net root force matched closely with force balance measurements. The framework had a net root force of 17.8 N whereas the balance measured 15.8 N. A vortex-lattice method (VLM) model came out to 15.8 N under the same circumstances though this solution did not match the circulation-based lift load. This analysis showed an inconsistency in the prescribed AOA and the effective AOA, which was found to be 3.32° rather than the prescribed 5°. Hence, the VLM result may be flawed as the real case was likely under a different AOA still. Moreover, other experimental inconsistencies with respect to the framework such as the application of zig-zag strips on the test model and wind tunnel effects were considered in drawing the conclusion of the comparison of the framework's capabilities with the measurements and VLM. It is expected that the splitter table in the test set-up induced a boundary layer which reduced the net lift root force and thus the resultant lift coefficient which was used to calculate the effective AOA.

The dynamic case was a harmonic gust excitation under the same static circumstances with a frequency of 2 Hz and a gust vane AOA of ±5° which defined the gust amplitude. From a preliminary static assessment on the validation tool of MSC.Nastran, it was found that the shell model as used by MSC.Nastran and the FEM model used in the framework have minor discrepancies based on an analysis of the tip deflection of the two models under the same load. The dynamic force balance measurements were compared to the prediction from the framework and the results of MSC.Nastran in terms of the net root force, root moment in the longitudinal direction and in both aerodynamic and inertial net root forces. Overall, the results matched closely though the framework had an over-prediction in the root force, likely caused by the error in the FEM model and the loss of lift induced by the boundary layer in the experiment. Moreover, at smaller deflections it was

shown that the framework performs with less reliability as the relative error in marker measurement increases when the absolute deflection is smaller. The dynamic case also showed that it is possible to calculate the inertial forces from a mass distribution and the acceleration from the markers, which closely matched the inertial forces from MSC.Nastran. Hence, the framework has proven its feasibility in the quantitative characterisation of Collar's triangle in an unsteady dynamic case when considering net root forces. The bending moment coefficient was used to assess the overall load distribution during the gust. At this stage, there is no reason to believe that the span-wise distribution is inaccurate since the root moment was also closely matching the force balance measurements considering the aforementioned differences in net root force though further validation is required for this topic. Lastly, both for the static and dynamic cases it was concluded that with the application of statistical averaging of multiple measurements through mean or phase-averaging computations it is possible to reduce the effect of random errors in the measurements up to the point where they are negligible. Only errors in the FEM model were found to be systematic and are found in the force distribution.

In pursuance of further research on the framework, a few recommendations may be made. In first instance, the aforementioned static and dynamic cases may be further validated in the span-wise sense with another experimental campaign in which the focus lies on resolving the actual load on the wing. In such a campaign, more span-wise measurements with PIV may allow for an insight into the actual load distribution rather than relying on a VLM result. The prediction which is based on an LLT function may also be changed to more complex models to incorporate other unsteady effects. In addition, as a linear separation was performed for the three deflection components caused by the three individual forces, further assessment is necessary to assess the performance when non-linear deflection effects are present.

For improvements on the framework itself, one may consider to include the measurements from the force balance as constraints. By using the net root force and the root moment as constraints, the optimisation may take these into account to further adjust the results towards empirical values. The input to the framework may also be improved by using shape functions to describe the deflection of the structure to reduce the effect of the error in the marker measurements. For this sake, one may also consider using other displacement measurement techniques which provide a similar span-wise deflection and higher accuracy.

Finally, it was shown how an error in the used FEM model has a linear relation to the error in the resultant aerodynamic force. In following applications of the framework, it is suggested that an effort is made to reduce such errors in the FEM modelling. One could consider ground-vibration tests to assess the natural frequencies of the structure or static deflection tests to compare deflections from the FEM model and the actual test. A similar assessment may be performed to ensure that the mass distribution used for the inertial forces is improved.

Bibliography

[1] John David Anderson Jr. Fundamentals of aerodynamics. Tata McGraw-Hill Education, 2010.

[2] Roger C Baker. Flow measurement handbook: industrial designs, operating principles, performance, and applications. Cambridge University Press, 2005.

[3] Raymond L Bisplinghoff, Holt Ashley, and Robert L Halfman. Aeroelasticity. Courier Corporation, 2013.

[4] Charlene Black, Kumar V Singh, Steven Goodman, Aaron Altman, and Raymond M Kolonay. Design, fabrication and testing of 3d printed wings for rapid evaluation of aeroelastic performance. In 2018 AIAA/ASCE/AHS/ASC Structures, Structural Dynamics, and Materials Conference, page 1997, 2018.

[5] Harvey H Brown et al. A method for the determination of the spanwise load distribution of a flexible swept wing at subsonic speeds. Technical report, NATIONAL AERONAUTICS AND SPACE ADMINISTRATION WASHINGTON DC, 1951.

[6] AR Collar. The expanding domain of aeroelasticity. The Aeronautical Journal, 50(428):613–636, 1946.

[7] Tomás de Rojas Cordero. Integrated aerodynamic and structural measurements of the gust response of a flexible wing with robotic piv. Master's thesis, Delft University of Technology, 2020.

[8] C Easa. Certification specifications for large aeroplanes, cs 25, 2009.

[9] Mostafa SA Elsayed, Ramin Sedaghati, and Mohammed Abdo. Accurate stick model development for static analysis of complex aircraft wing-box structures. AIAA journal, 47(9):2063–2075, 2009.

[10] Gerrit E Elsinga, Fulvio Scarano, Bernhard Wieneke, and Bas W van Oudheusden. Tomographic particle image velocimetry. Experiments in fluids, 41(6):933–947, 2006.

[11] Etana Ferede and Mostafa Abdalla. Cross-sectional modelling of thin-walled composite beams. In 55th AIAA/ASMe/ASCE/AHS/SC Structures, Structural Dynamics, and Materials Conference, page 0163, 2014.

[12] Joel H Ferziger, Milovan Perić, and Robert L Street. Computational methods for fluid dynamics, volume 3. Springer, 2002.

[13] Yuan Cheng Fung. An introduction to the theory of aeroelasticity. Courier Dover Publications, 2008.

[14] Marco Gherlone, Priscilla Cerracchio, Massimiliano Mattone, Marco Di Sciuva, and Alexander Tessler. An inverse finite element method for beam shape sensing: theoretical framework and experimental validation. Smart Materials and Structures, 23(4):045027, 2014.

[15] Sharon Suzanne Graves, Alpheus W Burner, John W Edwards, and David M Schuster. Dynamic deformation measurements of an aeroelastic semispan model. Journal of aircraft, 40(5):977–984, 2003.

[16] Mohammad Yazdi Harmin. Aeroelastic modelling and design. PhD thesis, University of Liverpool, 2012.

[17] Frederic M Hoblit. Gust loads on aircraft: concepts and applications. American Institute of Aeronautics and Astronautics, 1988.

[18] Constantin Jux, Andrea Sciacchitano, Jan FG Schneiders, and Fulvio Scarano. Robotic volumetric piv of a full-scale cyclist. Experiments in Fluids, 59(4):74, 2018.

[19] Thiemo Kier. Comparison of unsteady aerodynamic modelling methodologies with respect to flight loads analysis. In AIAA Atmospheric Flight Mechanics Conference and Exhibit, page 6027, 2005.

[20] Hans Georg Kussner. Stresses produced in airplane wings by gusts. NASA, 1932.

[21] Paul MGJ Lancelot, Jurij Sodja, Noud PM Werter, and Roeland De Breuker. Design and testing of a low subsonic wind tunnel gust generator. Advances in aircraft and spacecraft science, 4(2):125, 2017.

[22] PMGJ Lancelot, Jurij Sodja, and Roeland De Breuker. Investigation of the unsteady flow over a wing under gust excitation. In 17th International Forum on Aeroelasticity and Structural Dynamics. International Forum on Aeroelasticity and Structural Dynamics (IFASD), 2017.

[23] LEM Lignarolo. On The Turbulent Mixing in Horizontal Axis Wind Turbine Wakes. PhD thesis, Delft University of Technology, 2016.

[24] Tianshu Liu, Alpheus W Burner, Thomas W Jones, and Danny A Barrows. Photogrammetric techniques for aerospace applications. Progress in Aerospace Sciences, 54:1–58, 2012.

[25] Yi Liu, Changchuan Xie, Chao Yang, and Jialin Cheng. Gust response analysis and wind tunnel test for a high-aspect ratio wing. Chinese Journal of Aeronautics, 29(1):91–103, 2016.

[26] Holger Mai, Jens Neumann, and Holger Hennings. Gust response: a validation experiment and preliminary numerical simulations. Proceedings" IFASD 2011", 2011.

[27] Thomas Henry Gordon Megson. Aircraft structures for engineering students. Butterworth-Heinemann, 2016.

[28] Francesco Mitrotta. Experimental fluid-structure interaction of a flexible plate under gust excitation. Master's thesis, Delft University of Technology, 2020.

[29] Francesco MA Mitrotta, Andrea Sciacchitano, Jurij Sodja, Roeland De, and Bas W Breuker. Experimental investigation of the fluid-structure interaction between a flexible plate and a periodic gust by means of robotic volumetric piv. In Proceedings of the 13th International Symposium on Particle Image Velocimetry. Universitat der Bundeswehr Munchen, 2019.

[30] Francesco Mario Antonio Mitrotta, Darwin Rajpal, Jurij Sodja, and Roeland De Breuker. Multi-fidelity design of an aeroelastically tailored composite wing for dynamic wind-tunnel testing. In AIAA Scitech 2020 Forum, page 1636, 2020.

[31] Robert L Mott. Applied strength of materials. CRC Press, 2007.

[32] S Naik and R Raghavendra. Deflection estimation of varying cross section cantilever beam. International Journal for Scientific Research & Development, 2:11–42, 2015.

[33] Jens Neumann and Holger Mai. Gust response: Simulation of an aeroelastic experiment by a fluid–structure interaction method. Journal of Fluids and Structures, 38:290–302, 2013.

[34] David Ordoñez Celaya. Time-averaged pressure from robotic volumetric piv. Master's thesis, Delft University of Technology, 2020.

[35] Mayuresh Patil. Nonlinear gust response of highly flexible aircraft. In 48th AIAA/ASME/ASCE/AHS/ASC Structures, Structural Dynamics, and Materials Conference, page 2103, 2007.

[36] K Pengel, R Müller, and BG Van der Wall. Stereo pattern recognition–the technique for reliable rotor blade deformation and twist measurement. In Proceedings of the American Helicopter Society International Meeting on Advanced Rotorcraft Technology and Life Saving Activities (Heli Japan), Tochigi, Utsunomiya, Japan, 2002.

[37] Ulf Ringertz, David Eller, Donald F Keller, and Walter A Silva. Design and testing of a full span aeroelastic wind tunnel model. In 17th International Forum on Aeroelasticity and Structural Dynamics, IFASD 2017, 25 June 2017 through 28 June 2017. International Forum on Aeroelasticity and Structural Dynamics (IFASD), 2017.

[38] John Roy, Tianshu Liu, and Colin Britcher. Extracting dynamic loads from optical deformation measurements. In 47th AIAA/ASME/ASCE/AHS/ASC Structures, Structural Dynamics, and Materials Conference 14th AIAA/ASME/AHS Adaptive Structures Conference 7th, page 2187, 2006.

[39] Edoardo Saredi, Andrea Sciacchitano, and Fulvio Scarano. Multi-δt 3d-ptv based on reynolds decomposition. Measurement Science and Technology, 2020.

[40] Daniel Schanz, Sebastian Gesemann, and Andreas Schröder. Shake-the-box: Lagrangian particle tracking at high particle image densities. Experiments in fluids, 57(5):70, 2016.

[41] Jan FG Schneiders, Fulvio Scarano, Constantin Jux, and Andrea Sciacchitano. Coaxial volumetric velocimetry. Measurement Science and Technology, 29(6):065201, 2018.

[42] Andrea Sciacchitano and Daniele Giaquinta. Investigation of the ahmed body cross-wind flow topology by robotic volumetric piv. In Proceedings of the 13th International Symposium on Particle Image Velocimetry. Universitat der Bundeswehr Munchen, 2019.

[43] Andrea Sciacchitano and Fulvio Scarano. Elimination of piv light reflections via a temporal high pass filter. Measurement Science and Technology, 25(8):084009, 2014.

[44] HS Timmermans, JH van Tongeren, EGM Geurts, RFA Marques, MS Correa, and Stefan Waitz. Design and validation of a numerical high aspect ratio aeroelastic wind tunnel model (hmae1). International Forum on Aeroelasticity and Structural Dynamics, 2019.

[45] C Wales, D Jones, and A Gaitonde. Simulation of airfoil gust responses using prescribed velocities. In International Forum on Aeroelasticity and Structural Dynamics, 2011.

[46] C Wales, D Jones, and A Gaitonde. Prescribed velocity method for simulation of aerofoil gust responses. Journal of Aircraft, 52(1):64–76, 2015.

[47] Jearl Walker, Robert Resnick, and David Halliday. Principles of physics: international student version. Wiley, 2011.

[48] Stephen Warwick, Mario Bras, Jenner Richards, and Afzal Suleman. Measurement of aeroelastic wing deflections using modal shapes and strain pattern analysis. In AIAA Scitech 2019 Forum, page 1116, 2019.

[49] Jan Robert Wright and Jonathan Edward Cooper. Introduction to aircraft aeroelasticity and loads, volume 20. John Wiley & Sons, 2008.